A scanning electron microscope for ultracold quantum gases

Disseration

zur Erlangung des Grades

"Doktor

der Naturwissenschaften"

am Fachbereich Physik

der Johannes Gutenberg-Universität

in Mainz

Tatjana Gericke

geboren in Rüsselsheim

Mainz, den 01.03.2010

D77

1. Gutachter:
2. Gutachter:

Tag der mündlichen Prüfung: 24.08.2010

Zusammenfassung

In dieser Arbeit wird eine neue Abbildungsmethode für ultrakalte Quantengase vorgestellt. Seit der ersten experimentellen Beobachtung eines Bose-Einstein Kondensates, stellen ultrakalte Atome ein wichtiges Gebiet zur Untersuchung fundamentaler Quanteneffekte in Mehr-Teilchen Systemen dar. Die meisten dieser Experimente benutzen optische Abbildungsmethoden um Informationen aus den Systemen zu extrahieren und sind deshalb an die fundamentalen Limitierungen dieser Methode gebunden: die bestmögliche räumliche Auflösung ist vergleichbar mit der Wellenlänge des benutzten Lichtfeldes. Da allerdings der mittlere atomare Abstand und die Längenskala von charakteristischen räumlichen Strukturen in Bose-Einstein Kondensaten wie Vortices oder Solitonen zwischen 100 nm und 500 nm liegt, wird eine Abbildungsmethode mit einer entsprechenden räumlichen Auflösung benötigt. In dieser Arbeit wird nun eine Abbildungsmethode vorgestellt die das Prinzip des Rasterelektronenmikroskops auf ultrakalte Quantengase erweitert. Dabei wird ein fokussierter Elektronenstrahl über die Wolke von kalten Atomen bewegt und die lokal erzeugten Ionen anschliessend detektiert. Mit dieser Methode ist es möglich die Dichteverteilung eines Bose-Einstein Kondensates in der Falle präzise zu vermessen. Des weiteren wird die Dichteverteilung in eindimensionalem und zweidimensionalen optischen Gittern ermittelt und darüber das räumliche Auflösungsvermögen bestimmt. Abschliessend wird die Vielseitigkeit der Methode durch das gezielte Entfernen einzelner Gitterplätze demonstriert.

Abstract

This thesis presents a new imaging technique for ultracold quantum gases. Since the first observation of Bose-Einstein condensation, ultracold atoms have proven to be an interesting system to study fundamental quantum effects in many-body systems. Most of the experiments use optical imaging methods to extract the information from the system and are therefore restricted to the fundamental limitation of this technique: the best achievable spatial resolution that can be achieved is comparable to the wavelength of the employed light field. Since the average atomic distance and the length scale of characteristic spatial structures in Bose-Einstein condensates such as vortices and solitons is between 100 nm and 500 nm, an imaging technique with an adequate spatial resolution is needed. This is achieved in this work by extending the method of scanning electron microscopy to ultracold quantum gases. A focused electron beam is scanned over the atom cloud and locally produces ions which are subsequently detected. The new imaging technique allows for the precise measurement of the density distribution of a trapped Bose-Einstein condensate. Furthermore, the spatial resolution is determined by imaging the atomic distribution in one-dimensional and two-dimensional optical lattices. Finally, the variety of the imaging method is demonstrated by the selective removal of single lattice site.

Contents

Chapter 1

Introduction

Our knowledge of the world, with all its intriguing and fascinating phenomena, depends on the ability to probe the objects of interest. In particular, the invention of more and more sophisticated detection techniques have allowed for deeper insights into the microscopic and macroscopic world. On the other hand, the urge to advance into unexplored regimes of nature, are usually accompanied by the development of new measurement techniques and methods.

A central role in measurement and detection, whether it is on macroscopic [1] or microscopic scale, plays imaging. In particular, if we turn our attention on microscopic structures, the spatial resolution of the imaging system is of high interest. In the case optical imaging in free space the spatial resolution is fundamentally limited by the imaging wavelength, as expressed in the Abbe criterion [2]. To overcome this limitation it is necessary to develop new imaging techniques beyond the bounds of optical approaches. The development of the scanning electron microscope, pioneered by Manfred von Ardenne [3], greatly contributed to the understanding of microscopic structures. With the aid of electron microscopy it is possible to investigate surfaces and structures with a spatial resolution of few nanometers and below.

The microscopic world offers a wide range of exotic and bewildering phenomena that contradicts our daily experience of the world: Particles behave like waves [4], tunnel through "impenetrable" barriers [5] or are inseparably connected by entanglement [6]. This regime of nature, to our current knowledge, is described by the theory of quantum mechanics. Although quantum mechanics characterizes this microcosm with good agreement, the

complexity of even small systems makes a detailed description difficult. It is therefore highly desirable to study the quantum regime in well defined, fully controllable environments.

In recent years, promising implementations of such a quantum laboratory have emerged in form of ultracold atoms. In particular, the experimental realization of the Bose-Einstein condensate [7, 8, 9, 10, 11], theoretically predicted by Einstein [12] and Bose [13] in 1925, allowed for a rapid progress of the research field in the last decade. The study of this state of matter, with its macroscopic occupation of the ground state below a critical temperature, enabled a proceeding understanding of the state itself and its relation to phenomena such as superfluidity [14], superconductivity [15], and magnetism [16, 17]. Furthermore, the research field has been extended to fermionic quantum gases, and the creation of ultracold molecules [18, 19, 20] as well as non-linear effects in matter waves [21].

By transferring condensed atoms into arrays of microscopic traps [22], created by interfering laser beams, extraordinary possibilities to study strongly correlated many-body physics [23] and the preparation of low-dimensional systems [24, 25, 26, 27] have opened up. The interfering laser beams form periodic potentials that allow for the mimicking of solid state systems, whose properties are completely controlled by the employed light fields. This high experimental control in combination with long coherence times, allows to model and explore condensed matter problems with unprecedented perfection [28, 29, 30]. In addition, these optical lattice systems feature promising possibilities for scalable quantum information processing [31, 32] and precision metrology [33].

Although the Bose-Einstein condensate is one of the largest quantum objects available, the typical size is very small, in the order of a ten few micrometers. This minuscule extend makes it challenging to image an ensemble of condensed atoms with high spatial resolution by typically employed optical methods. Despite the fact, that ultracold quantum gases can be experimentally prepared and controlled with highest accuracy, the information about these system is usually obtained by techniques that are fundamentally limited in their spatial resolution. Hence, the granular structure of matter that underlies the many-body wave function of a Bose-Einstein condensate or atoms trapped at individual sites of an optical lattice can in general not be directly observed. The characteristic length scales in ultracold quantum gases, such as the mean distance between atoms in a Bose-Einstein con-

densate, the healing length, or the spacing between two sites in an optical lattice, is on the order of a few hundred nanometers.

The aim of this thesis is to transfer the principle of scanning electron microscopy for application in ultracold quantum gases. By scanning a focused electron beam through a cloud of trapped, neutral atoms, the powerful technique of scanning electron microscopy can be extended from solid surfaces to gaseous targets. In combination with subsequent ion detection of locally produced ions, a high resolution, single atom sensitive imaging tool for ultracold quantum gases is created. In this thesis, the great functionality of this technique is demonstrated by precise density measurements of a trapped Bose-Einstein condensate. Moreover, the high spatial resolution of the imaging system is documented by resolving single sites of an one- and two-dimensional submicrometer optical lattice.

Overview

This thesis is organized as follows. Chapter 2 will introduce the theoretical description of ultracold bosons. Starting with the ideal Bose gas in a harmonic trap to establish the concept of Bose-Einstein condensation, we turn to the more realistic interacting Bose gases. Since the interaction between ultracold quantum gases is mediated by scattering processes in the s-wave regime, scattering theory will be shortly reviewed. The chapter proceeds with the introduction of the characteristic interaction length, which determines the length scale of solitons and vortices in ultracold quantum gases. Finally, we will discuss the ground state of a trapped Bose gas. Chapter 3 covers the imaging of ultracold quantum gases, starting with the most common optical and non-optical imaging techniques. Thereafter, we turn to electron microscopy of ultracold quantum gases by introducing the possible electron atom interactions. The formation of an all-optical Bose-Einstein condensate in an electron microscope is the content of chapter 4. The electron column is presented and characterized in chapter 5. Subsequently, the functionality of the method is documented by imaging the density distribution of a trapped Bose-Einstein condensate. The resolution of the new imaging technique is determined in chapter 6 by imaging single sites of an optical lattice. Finally, we demonstrate the addressing of single lattice sites and the preparation of arbitrary patterns in a two dimensional optical lattice.

Publications in Context of This Work

- **A scanning electron microscope for ultracold atoms**
  T. Gericke, C. Utfeld, N. Hommerstad and H. Ott
  Laser Physics Letters **3**, 415 (2006)

- **All-optical formation of a Bose-Einstein condensate for applications in scanning electron microscopy**
  T. Gericke, P. Würtz, D. Reitz, C. Utfeld, and H. Ott
  Applied Physics B: Lasers and Optics **89**, 447 (2007)

- **Probing Bose-Einstein Condensates by Electron Impact Ionization**
  P. Würtz, T. Gericke, T. Langen, A. Koglbauer, H. Ott
  J. Phys.: Conf.Ser. **141**, 012020 (2008)

- **High-resolution scanning electron microscopy of an ultracold quantum gas**
  T. Gericke, P. Würtz, D. Reitz, T. Langen, H. Ott
  Nat. Phys. **4**, 949 (2008)

- **Experimental Demonstration of Single-Site Addressability in a Two-Dimensional Optical Lattice**
  P. Würtz, T. Langen, T. Gericke, A. Koglbauer, H. Ott
  Phys. Rev. Lett. **103**, 080404 (2009)

- **Image formation in scanning electron microscopy of ultracold atoms**
  P. Würtz, T. Gericke, A. Vogler, F. Etzold, and H. Ott
  Applied Physics B: Lasers and Optics **98** , 641 (2010)

Chapter 2

Theory of Ultracold Bosons

The fact that identical particles cannot be distinguished in the microscopic world, results in a statistical behavior which differs from that, known in the classical world. Microscopic particles can be divided into two groups: those which carry an integer spin and those with an half integer spin. The former are named bosons and the latter fermions. Fermions follow the Fermi-Dirac distribution [34, 35, 36, 37] which states, that two identical fermions cannot occupy the same quantum state, known as the Pauli exclusion principle. The statistical behavior of bosons is completely different and described by the so called Bose-Einstein distribution [12, 13]. From it arises, that an unlimited number of identical bosons can occupy the same state.

A direct consequence of the Bose-Einstein statistics is a phase transition, that occurs below a critical temperature in a bosonic ensemble, inducing a macroscopically occupied ground state. This phenomenon, known as Bose-Einstein condensation, has been theoretically predicted by Bose and Einstein [12, 13] in 1925 and experimentally realized in 1995 [7, 8, 9, 10, 11] in dilute gaseous samples of alkali metals.

The following section is split in two parts and will give an introduction to the theory of trapped, interacting Bose gases. The first part reviews the theoretical description of a Bose gas at zero temperature, while the second discusses simplification models for the characterization of the many-body ground state of a trapped Bose gas.

2.1 Interacting Bose Gases at Zero Temperature

The theoretical description of Bose condensed samples provides deeper insights of the density profile of ultracold quantum gases especially the spatial form and moreover spatial structures that can occur. In order to discuss the characteristics of interacting Bose gases it is convenient to recall the derivation of Bose-Einstein condensation for a trapped ensemble of ideal, non-interacting bosons. This short review follows loosely the discussion of Bose-Einstein condensation in a variety of statistical mechanics text books, e.g. [38, 39]. For a better understanding how the interaction between two ultracold boson is mediated, an introduction to scattering theory and cold collisions is given before entering the field of interacting Bose gases.

2.1.1 The Ideal Bose Gas in a Harmonic Trap

The case of the ideal Bose gas in a harmonic trap is considered, because almost all Bose-Einstein condensates realized in experiments, are produced in a trap which's potential can be harmonically approximated.

A harmonic potential is given by

$$V_{\text{ext}}(\mathbf{r}) = \frac{1}{2}m\omega_x^2 x^2 + \frac{1}{2}m\omega_y^2 y^2 + \frac{1}{2}m\omega_z^2 z^2 \tag{2.1}$$

with $\omega_x^2, \omega_y^2, \omega_z^2$ being the oscillator frequencies and m the mass of the atom. The eigenvalues of the single-particle Hamiltonian

$$\hat{H} = \frac{\hat{p}^2}{2m} + \hat{V}_{\text{ext}}(\mathbf{r}) \tag{2.2}$$

are

$$\epsilon_{n_x n_y n_z} = \hbar\omega_x n_x + \hbar\omega_y n_y + \hbar\omega_z n_z \quad , \tag{2.3}$$

where n_x, n_y, n_z are positive integer numbers that label the quantum state of the system and $\hbar$ is the reduced Planck's constant. The zero point energies of the harmonic oscillators have been omitted in this expression since they only shift the energy scale.
The average occupation number of the ith single-particle state in a system of non-interacting bosons at thermal equilibrium is then

$$\bar{n}_i = \frac{1}{e^{\beta(\epsilon_i - \mu)} - 1} = \frac{1}{\zeta^{-1}e^{\beta\epsilon_i} - 1} \quad , \tag{2.4}$$

where ϵ_i is the energy of the ith state, $\zeta = \exp[\beta\mu]$ the fugacity, and $\beta = 1/k_B T$ with the Boltzmann constant k_B and the temperature T. The chemical potential μ has to be fixed to the total number of particles N by the normalization

$$\sum_i \bar{n}_i = N \quad . \tag{2.5}$$

The relation $\mu < \epsilon_i$ must hold for any state i otherwise the occupancy of the state would be negative. This means on the other hand that the fugacity fulfills the relation

$$0 < \zeta < 1 \quad . \tag{2.6}$$

In the limit $\zeta \to 0$, the average occupancy (2.4) agrees with the classical Boltzmann statistic where $\bar{n}_i \propto \exp[-\beta\epsilon_i]$. The characterizing feature of the limit $\zeta \to 1$ becomes apparent in the average occupation of the ground state that is given by

$$\bar{n}_0 = \frac{1}{\zeta^{-1} - 1} = \frac{\zeta}{1 - \zeta} \quad . \tag{2.7}$$

For $\zeta \to 1$, equation (2.7) diverges, indicating that the ground state of the system is macroscopically filled.

For further investigation of the occupancy of the ground state one can use the normalization (2.5) and explicitly separate the number of atoms N_0 in the ground state from the atoms in the other states

$$N = N_0 + \sum_{i \neq 0} \frac{1}{\zeta^{-1} e^{\beta\epsilon_i} - 1} =: N_0 + N_T \quad . \tag{2.8}$$

To determine the number of thermal atoms N_T the sum in (2.8) is replaced by the integral[1]

$$N_T = \int \frac{1}{\zeta^{-1} e^{\beta\epsilon_{n_x n_y n_z}} - 1} dn_x dn_y dn_z = g_3(\zeta) \left(\frac{k_B T}{\hbar\bar{\omega}}\right)^3 \quad , \tag{2.9}$$

where $\bar{\omega} = (\omega_x \omega_y \omega_z)^{\frac{1}{3}}$ is the geometric averaged trapping frequency and $g_3(\zeta)$ is a special case of a so called Bose function[2], which has a maximum for $\zeta = 1$. Equations (2.8) and (2.9) allow for the definition of a critical temperature T_c at which the macroscopically occupation of the ground state

[1] The replacement of the sum by the integral is valid if the number of trapped atoms is large and $k_B T \gg \hbar\omega_{\mathrm{ho}}$ [40].

[2] Bose function: $g_p(z) = \frac{1}{\Gamma(p)} \int_0^\infty x^{p-1} \frac{1}{z^{-1} e^x - 1} dx$

starts. The critical temperature is obtained in the limit $N_0 \to 0$ at $T = T_c$ and given by

$$k_B T_c = \hbar\bar{\omega} \left(\frac{N}{g_3(1)} \right)^{\frac{1}{3}} = 0.94 \hbar\bar{\omega} N^{\frac{1}{3}} \quad . \tag{2.10}$$

Below the critical temperature T_c the system undergoes the transition to a Bose-Einstein condensate. This means that the ground energy state is occupied in a macroscopic way. The critical temperature T_c decreases as the particle number N is reduced.

2.1.2 Scattering Theory

So far the phenomenon of Bose-Einstein condensation has been discussed in the special case of non-interacting bosons. The description of ultracold bosons will be extended to interacting particles in the following sections. The most basic process that can occur is the collision between two particles. Therefore this section starts with a brief review on elementary scattering theory at ultralow temperatures between two spinless particles. Followed by an introduction of the weakly-interacting Bose gas which was firstly introduced by Bogoluibov and the description of a nonuniform Bose gas by the Gross-Pitaevskii equation.

The general Hamiltonian for the scattering process between two identical, neutral, and spinless particles with mass m can be written as the combination of the free particle Hamiltonian $\hat{H}_0 = \hat{p}^2/2\mu$ and the scattering potential $\hat{V}$

$$\hat{H} = \hat{H}_0 + \hat{V} \quad . \tag{2.11}$$

For identical particles the reduced mass is $\mu = m/2$. The presence of a scatterer $\hat{V}$ causes the energy eigenstates to differ from the free particle eigenstates. This leads to the basic Schrödinger equation

$$\left(\hat{H}_0 + \hat{V} \right) |\Psi_k\rangle = E_k |\Psi_k\rangle \tag{2.12}$$

for the wave function Ψ_k where $E_k = \frac{\hbar^2 \mathbf{k}^2}{2\mu}$ with $\mathbf{k}$ denoting the wave vector of the scattered particle. The solution to this problem is presented in many text books [41]. Therefore we will confine the discussion to the relevant cases for this thesis.

The general solution of a scattering problem assumes an observer which is placed far away from the finite scatter potential. Hence, only the asymptotic incoming and outgoing states can be observed. The asymptotic scat-

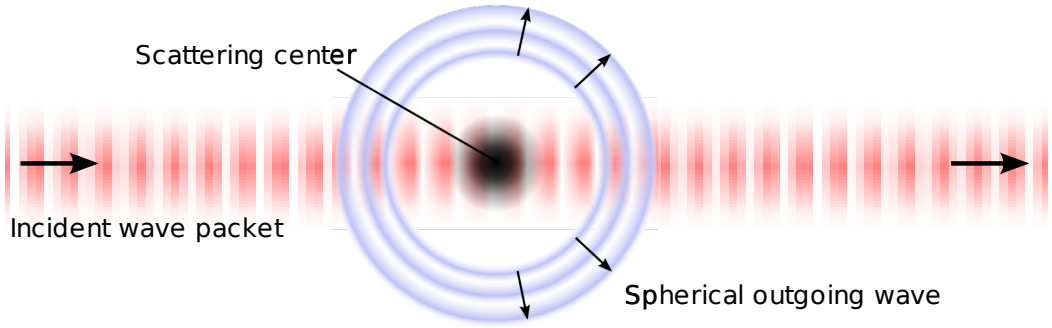

Figure 2.1: Illustration of the scattering mechanism. The incident wave packet continues to move in the incoming direction whereas the scattering potential generates a spherical outgoing wave front, which is scaled by the from factor.

tering function has the form of an incoming plane wave plus an outgoing spherical wave, and is given by

$$\begin{aligned}\Psi_k(\mathbf{x}) &\sim \frac{1}{(2\pi)^{3/2}} e^{i\mathbf{k}\cdot\mathbf{x}} - \frac{e^{ikr}}{r}\frac{2m}{4\pi\hbar^2}\int d^3x' e^{-i\mathbf{k}'\cdot\mathbf{x}'} V(\mathbf{x}')\,\Psi_k^+(\mathbf{x}') \\ &= \frac{1}{(2\pi)^{3/2}}\left[e^{i\mathbf{k}\cdot\mathbf{x}} + \frac{e^{ikr}}{r} f(\mathbf{k}',\mathbf{k})\right] \quad ,\end{aligned} \tag{2.13}$$

where $\mathbf{k}$ denotes the incoming wave vector, $\mathbf{k}'$ the outgoing wave vector and the amplitude of the outgoing spherical wave $f(\mathbf{k}',\mathbf{k})$ is the so called form factor. The form factor is a measure of the deviation of the target from a point-like scatter and is represent by

$$\begin{aligned}f(\mathbf{k}',\mathbf{k}) &\equiv -\frac{1}{4\pi}\frac{2m}{\hbar^2}(2\pi)^3\int d^3x' \frac{e^{-i\mathbf{k}'\cdot\mathbf{x}'}}{(2\pi)^{3/2}} V(\mathbf{x}')\,\Psi_k^+(\mathbf{x}') \\ &\equiv -\frac{1}{4\pi}(2\pi)^3\frac{2m}{\hbar^2}\langle\mathbf{k}'|V|\Psi_k^+\rangle \quad .\end{aligned} \tag{2.14}$$

The scattering principle is illustrated in figure 2.1.

A characteristic value for a scattering potential is the cross section, which is defined as the number of particles scattered into a differential solid-angle element $d\Omega$ per unit time and normalized by the number of incident particles. The differential cross section $\frac{d\sigma}{d\Omega}$ is determined by assuming a large

number of identically prepared particles which can be characterized by a plain wave. Insofar as the first term in equation (2.13) indicates the incoming particles and the second term the scattered ones, the total cross section is defined as

$$\frac{d\sigma}{d\Omega}d\Omega = \frac{r^2|\mathbf{j}_{\text{scatt}}|d\Omega}{|\mathbf{j}_{\text{incid}}|} = |f(\mathbf{k}', \mathbf{k})|^2 d\Omega \quad , \tag{2.15}$$

with a differential cross section of

$$\frac{d\sigma}{d\Omega} = |f(\mathbf{k}', \mathbf{k})|^2 \quad . \tag{2.16}$$

Due to the dependence on the unknown function $\Psi_k(x)$ it is not possible to exactly calculate the differential cross section and approximation method are needed.

Partial Wave Expansion

For a spherical symmetric scattering potential it is well suited to expand the scattering amplitudes in terms of the eigenfunctions of the angular momentum operator, which are called partial waves. This leads to an effective one dimensional potential

$$V_{\text{eff}}(r) = \frac{\hbar^2 (l+1) l}{2\mu r^2} + V(r) \tag{2.17}$$

where l denotes the partial wave. The total cross section which is the sum of all possible scattering amplitudes, is then given by the sum over all partial wave contributions

$$\sigma_{\text{tot}}(k) = \sum_{l=0}^{\infty} \sigma_l(k) = \frac{4\pi}{k^2} \sum_{l=0}^{\infty} (2l+1) \sin^2 \delta_l(k) \tag{2.18}$$

where $\delta_l(k)$ represents the phase shift of the partial wave with respect to the incoming wave caused by the scattering potential. This phase shift can be determined in the case of low energy, i.e. $k \to 0$, to be [42]

$$\delta_l(k) \approx n\pi - a_l k^{2l+1} \quad . \tag{2.19}$$

Here, n is an integer, and the coefficients a_l stand for proportionality constants of the lth partial wave, depending on the potential $V(r)$. By substituting the phase shift (2.19) into equation (2.18) and expand this around $k = 0$ it becomes clear, that for low energies the contribution of the lth partial wave vanishes as

$$\lim_{k \to 0} \sigma_l = k^{4l} \quad . \tag{2.20}$$

This result in the particular case of Bose-Einstein condensates indicates that only the partial wave with $l = 0$ has to be taken into account, because all higher partial waves are reflected by the centrifugal barrier of the potential (2.17), before they feel an influence of the scattering potential. This regime is called the s-wave scattering regime and in the case of ^{87}Rb - the atomic species employed in this work - this regime is reached below some 100μK [43] whereas the typical temperatures of a ^{87}Rb BEC is well below 1μK. Hence, all interaction effects between ultracold atoms can be treated in the s-wave scattering regime.

The s-Wave Scattering Length

In the case of s-wave collisions, the phase shift between the incoming and outgoing is determined by a single parameter $a_s \equiv a_{l=0}$ known as the s-wave scattering length which is given by

$$a_s = -\lim_{k\to 0} \frac{\tan \delta_0}{k} \quad . \tag{2.21}$$

The physical interpretation of the s-wave scattering length is given by the behavior of asymptote to the radial part of the wave function which has a zero crossing at a_s. The sign of the s-wave scattering length defines the nature of the interaction: A negative scattering length belongs to an attractive interacting, whereas a repulsive interaction is characterized by a positive scattering length. The meaning of the positive scattering length can be visualized as scattering of hard spheres with a radius a_s. The s-wave scattering length of ^{87}Rb is on the order of $100\, a_B$ [44], where a_B stands for the Bohr radius, with a numerical value of $a_B \approx 0.53$Å.

Cross Sections

So far only the case of collisions between two distinguishable particles have been considered. The total cross section in the s-wave scattering regime is therefore given by

$$\sigma_{\text{tot}} = 4\pi a_s^2 \quad . \tag{2.22}$$

This expression resembles the cross section of hard spheres with radius a_s in the s-wave scattering regime. Note, that this cross section is four times larger than the geometric cross section of a hard sphere.

In the case of indistinguishable particles the amplitude of the forward and backward scattering has to be summed, which modifies the cross section by a factor of two:

$$\sigma_{\text{tot}}^{\text{identical}} = 8\pi a_s^2 \quad . \tag{2.23}$$

The Fermi Contact Potential

A convenient formulation of the s-wave scattering is given by an effective contact potential

$$V(\mathbf{r}) = g\delta(\mathbf{r}) \quad , \tag{2.24}$$

where $\mathbf{r}$ denotes the relative distance between the collision partners, and g stands for the coupling constant of the interaction, which has to be chosen in such a way that both potentials- the real and the effective contact potential - lead to the same scattering length. The interaction coupling constant is therefore determined to

$$g = \frac{4\pi\hbar^2}{m} a_s \quad . \tag{2.25}$$

2.1.3 The Weakly-Interacting Bose Gas

The problem of the ideal Bose gas is that the ground state energy is zero in absence of interactions and therefore traditional perturbations techniques cannot be applied. This problem was solved by Bogoliubov [45] by introducing a new perturbation technique, which allows the identification of elementary excitations of the system. This microscopic theory of the condensed state take into account the quantum nature of excitations.

The model Hamiltonian considered by Bogoliubov describes a dilute Bose gas confined in a box of the volume V:

$$\hat{H} = \sum_p E_p \hat{a}_p^\dagger \hat{a}_p + \frac{V_0}{2V} \sum_{p,p',q} \hat{a}_{p+q}^\dagger \hat{a}_{p'-q}^\dagger \hat{a}_p \hat{a}_{p'} \quad , \tag{2.26}$$

where $E_p = \frac{p^2}{2m}$ denotes the free particle spectrum, $\hat{a}_p^\dagger$ and $\hat{a}_p$ represent the creation and annihilation operators of a boson in the state with the momentum p, and V_0 is the Fermi-contact potential as introduced in the previous section. For an ideal Bose gas at $T = 0$ K we can assume a macroscopic occupation of the ground state $p = 0$ and replace

$$\hat{a}_0^\dagger, \hat{a}_0 \to \sqrt{N_0} \tag{2.27}$$

with the ground state occupation number N_0. Moreover, this number should be similar to the total number of particles $N_0 \approx N$. With that assumption, and assuming that the fluctuations are small, which is equivalent to including only terms which are no more than quadratic in $\hat{a}_p^\dagger$ and $\hat{a}_p$ for $p \neq 0$ [46], the Hamiltonian becomes quadratic in the operators $\hat{a}_p^\dagger$ and $\hat{a}_p$ [47].

Bogoliubov has shown, that this Hamiltonian can be solved by introducing a canonical transformation of the operators

$$\hat{a}_p = u_p \hat{b}_p - v_p \hat{b}^\dagger_{-p} \qquad \hat{a}^\dagger_p = u_p \hat{b}^\dagger_p - v_p \hat{b}_{-p} \quad . \tag{2.28}$$

The new set of operators $\hat{b}^\dagger_p, \hat{b}_p$ obey as well the bosonic commutation rules

$$\left[\hat{b}_p, \hat{b}^\dagger_{p'}\right] = \delta_{pp'} \quad \text{and} \quad \left[\hat{b}_p, \hat{b}_{p'}\right] = \left[\hat{b}^\dagger_p, \hat{b}^\dagger_{p'}\right] = 0 \quad . \tag{2.29}$$

The Hamiltonian (2.26) can be transformed into

$$\hat{H} = \frac{1}{2} \sum_p \epsilon_p \left(\hat{b}^\dagger_p \hat{b}_p + \hat{b}^\dagger_{-p} \hat{b}_{-p} \right) \quad , \tag{2.30}$$

where ϵ_p stands for the Hamiltonian's excitation spectrum, if one chooses

$$u_p = \cosh \phi_p \, , \quad v_p = \sinh \phi_p \, , \quad \text{with} \quad \tanh 2\phi_p = \frac{\mu}{E_p + \mu} \quad . \tag{2.31}$$

Here, the chemical potential is given by $\mu = gn$ where $n = N/V$ represents the particle density and $g = V_0 = 4\pi\hbar^2 a_s/m$ is the interaction coupling constant. From the commutation relations in (2.29) follows, that $\hat{b}^\dagger_p \hat{b}_p$ has integer and non negative eigenvalues and therefore ϵ_0 represents the energy of the ground state. It can be regarded as the quasi-particle vacuum and is defined by

$$\hat{b}_p |0\rangle = 0 \qquad \forall \quad p \neq 0 \quad . \tag{2.32}$$

The average energy per particle in the ground state is given by

$$\frac{\epsilon_0}{N} = \frac{gn}{2} \left(1 + \frac{128}{15} \sqrt{\frac{na^3}{\pi}} \right) \quad . \tag{2.33}$$

The first term in this expression is $\mu/2$ and the second term is the Lee-Yang correction [48] which is non-analytic in the interaction parameter na^3.

The excitation spectrum ϵ_p is given by the Bogoliubov dispersion law

$$\epsilon_p \equiv \sqrt{\frac{\mu}{m} p^2 + \left(\frac{p^2}{2m} \right)^2} , \tag{2.34}$$

for elementary excitations in the system, which has two limiting cases

$$\epsilon_p \approx \begin{cases} \sqrt{\frac{\mu}{m}} p \, , & p \to 0 \\ \frac{p^2}{2m} + \mu \, , & p \to \infty \end{cases} \quad . \tag{2.35}$$

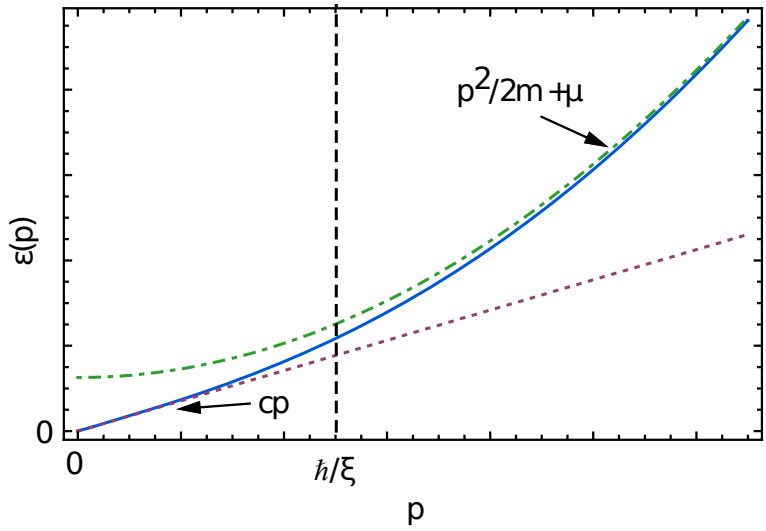

Figure 2.2: Bogoliubov dispersion of elementary excitations. The blue curves shows the Bogoliubov dispersion, while the red, dotted and the green, dash-dotted curve indicate the phonon-like and free particle-like dispersion, respectively. The transition between the phonon and free particle regimes takes place at $p \sim \hbar/\xi$.

The Bogoliubov dispersion together with the two cases of (2.35) are depicted in figure 2.2. The corresponding excitations for small momenta $p \ll mc$ are sound waves with a speed of sound

$$c = \sqrt{\frac{\mu}{m}} \quad , \tag{2.36}$$

while the dispersion law in the opposite limit $p \gg m$ resembles free particle-like excitations. The transition between the phonon and the particle regime takes place when $p^2/2m \approx gn$. By setting $p^2/2m = gn$ with $p = \hbar/\xi$ one can define the characteristic interaction length

$$\xi = \sqrt{\frac{\hbar^2}{2mgn}} \quad , \tag{2.37}$$

whose physical meaning will be discussed in the following.

Superfluidity in Weakly Interacting Bose Gases

The excitation spectrum prompts that weakly interacting Bose gases must show superfluidity: For a given dispersion relation ϵ_p of a medium, the Landau criterion [49] states, that an object moving at a velocity

$$v < v_c = \min_p \left[\epsilon_p / p\right] \quad , \tag{2.38}$$

smaller than a critical velocity v_c, cannot scatter from the medium. For free particles and as well for the Bose-Einstein condensate in an ideal gas, $\epsilon_p \sim p^2$ and therefore $v_c = 0$. For the weakly interacting Bose gas one finds $v_c = c > 0$ and therefore for particle velocities smaller than v_c it is a frictionless superfluid. The superfluidity of Bose-Einstein condensates has been studied in several experiments [50, 51, 52, 53, 54, 55, 56, 14] and its consequences will be discussed in section 2.1.5.

2.1.4 The Gross-Pitaevskii Equation

In the previous section, the interaction between the bosons has been introduced. In the following we will extend the description not only to the interaction between the particles but will also take the effect of an external trapping potential into account.

The Schrödinger equation describing an interacting system of bosons in an external potential is given by

$$\begin{aligned} i\hbar\frac{\partial}{\partial t}\hat{\Psi}\left(\mathbf{r},t\right) = \Bigg[& -\frac{\hbar^2\nabla^2}{2m} + V_{\text{ext}}\left(\mathbf{r},t\right) + \\ & \int \hat{\Psi}^\dagger\left(\mathbf{r}',t\right) V\left(\mathbf{r}'-\mathbf{r}\right) \hat{\Psi}\left(\mathbf{r}',t\right) d\mathbf{r}' \Bigg] \hat{\Psi}\left(\mathbf{r},t\right) \quad , \end{aligned} \tag{2.39}$$

where $V\left(\mathbf{r}-\mathbf{r}'\right)$ is the two-body potential, $\hat{\Psi}^\dagger$ is the field operator creating a particle, $\hat{\Psi}$ the annihilation field operator, and $V_{\text{ext}}\left(\mathbf{r},t\right)$ an external potential. Under the assumption of dilute gases, the range of the interatomic forces can be considered much smaller than the average distance between two particles

$$d = n^{-1/3} \quad . \tag{2.40}$$

This justifies the use of the two body potential $V\left(\mathbf{r}-\mathbf{r}'\right)$ [47]. The diluteness in combination with the low temperature, as it is needed for BEC, allows to simplify the two-body interaction potential with the Fermi contact

potential (see section 2.1.2). The field operator $\hat{\Psi}(\mathbf{r},t)$ can be decomposed in the form

$$\hat{\Psi}(\mathbf{r},t) = \Psi_0(\mathbf{r},t) + \delta\hat{\Psi}(\mathbf{r},t) \quad , \tag{2.41}$$

where the ground state is given by $\Psi_0(\mathbf{r},t)$, and the contribution of all higher state $\delta\hat{\Psi}(\mathbf{r},t)$ is treated as perturbations. The function $\Psi_0(\mathbf{r},t)$ is a classical field with the meaning of an order parameter [47] and usually called wave function of the condensate. By neglecting all terms of $\mathcal{O}\left[\delta\hat{\Psi}(\mathbf{r},t)\right]$ and higher equation (2.39) reduces to

$$i\hbar\frac{\partial}{\partial t}\Psi_0(\mathbf{r},t) = \left[-\frac{\hbar^2\nabla^2}{2m} + V_{\text{ext}}(\mathbf{r},t) + g|\Psi_0(\mathbf{r},t)|^2\right]\Psi_0(\mathbf{r},t) \quad , \tag{2.42}$$

which is also known as the Gross Pitaevskii equation [57, 58]. Here g is the interaction coupling constant as defined in (2.25). The condensate wave function is a complex quantity, which can be represented by an amplitude and a phase

$$\Psi_0(\mathbf{r},t) = |\Psi_0(\mathbf{r},t)|e^{iS(\mathbf{r},t)} \quad . \tag{2.43}$$

It is normalized to the total number of atoms, which results in the fact that the density of the condensate is given by

$$n(\mathbf{r},t) = |\Psi_0(\mathbf{r},t)|^2 \quad . \tag{2.44}$$

An equivalent representation of the Gross-Pitaevskii equation is given by the continuity equation

$$\frac{\partial n(\mathbf{r},t)}{\partial t} + \nabla\cdot(n\mathbf{v}_s) = 0 \quad , \tag{2.45}$$

with

$$\mathbf{v}_s(\mathbf{r},t) = \frac{\hbar}{m}\nabla S(\mathbf{r},t) \tag{2.46}$$

being the velocity of the condensate, and an equation for the phase of the condensate wave function

$$\hbar\frac{\partial}{\partial t}S(\mathbf{r},t) + \nabla\left[\frac{1}{2}m\mathbf{v}_s^2 + V_{\text{ext}} + gn - \frac{\hbar^2}{2m\sqrt{n}}\nabla^2\sqrt{n}\right] = 0 \quad . \tag{2.47}$$

Equation (2.45) is obtained by multiplying the Gross-Pitaevskii equation (2.42) with Ψ_0^* and subtracting the complex conjugation of the resulting expression. Equation (2.47) can be retrieved by inserting (2.43) into the Gross-Pitaevskii equation (2.42).

The Gross-Pitaevskii equation can be reduced to a simpler form in the case of stationary solutions, i.e. the time evolution of the condensate wave function is fixed by

$$\Psi_0(\mathbf{r},t) = \sqrt{n(\mathbf{r})}e^{-\frac{i\mu t}{\hbar}} \quad , \tag{2.48}$$

where the time dependence is determined by the chemical potential μ. The stationary Gross-Pitaevskii equation then takes the form

$$\left[-\frac{\hbar^2\nabla^2}{2m} + V_{\text{ext}}(\mathbf{r}) + g|\Psi_0(\mathbf{r})|^2\right]\Psi_0(\mathbf{r}) = \mu\Psi_0(\mathbf{r}) \quad , \tag{2.49}$$

where it is assumed that the external potential is time independent.

2.1.5 The Characteristic Interaction Length

The characteristic interaction length ξ (see (2.37)) has been introduced in the section 2.1.3 as the length that corresponds to the momentum which characterizes the transition between phonon and free particle regime in the Bogoliubov dispersion law. As it can be seen in the definition of the characteristic interaction length

$$\xi = \frac{\hbar}{\sqrt{2mgn}} = \frac{1}{\sqrt{8\pi a_s n}} \quad , \tag{2.50}$$

it only depends on the average density of the system n and a_s, the s-wave scattering length of the employed species. The physical meaning of the characteristic length scale will be discussed in the following. The characteristic interaction length is the parameter which describes the length scale on which a spatially disturbed density distribution of a quantum gas reaches its normal value. Due to this "healing" of the density distribution, the characteristic interaction length is also called healing length. As an example of possible spatial structures in a quantum gas with sizes are characterized by the healing length, we will briefly discuss the phenomenon of vortices and solitons.

Vortices

One of the most spectacular consequences of Bose-Einstein condensation is superfluidity [49]. In macroscopic systems superfluidity shows up with many peculiar features like absence of viscosity or quantized vortices which occur when a superfluid is rotated. Several of these properties can be interpreted as coherence effects associated with the phase $S(\mathbf{r},t)$ of the condensate wave

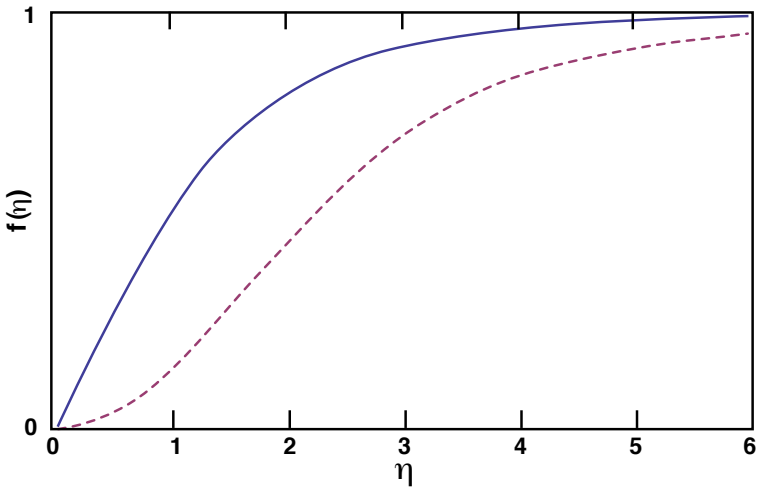

Figure 2.3: Density distribution of a vortex. The graph shows the solutions of the equation (2.57) for a singly charged vortex with $j = 1$ (blue, solid line) and a doubly charged vortex with $j = 2$ (red, dashed line). The obtained density distribution is plotted as a function of the radial coordinate $\eta = r/\xi$ [47].

function. The distinctive sign of an existing vortex is an imprint in the density.

As we have seen in equation (2.46), the velocity field of the condensate is proportional to the gradient of the scalar phase of the wave function

$$\mathbf{v}_s(\mathbf{r}, t) = \frac{\hbar}{m} \nabla S(\mathbf{r}, t) \quad . \tag{2.51}$$

This fact has far-reaching consequences for the possible motion of the fluid. For a normal fluid, the velocity field of a rotation is given by the rigid body form $\mathbf{v} = \mathbf{\Omega} \times \mathbf{r}$. In contrary to this, the rotation velocity field of a condensate is given by the gradient of the phase and from equation (2.51) follows immediately

$$\nabla \times \mathbf{v}_s(\mathbf{r}, t) = 0 \quad . \tag{2.52}$$

This means that a Bose-Einstein condensate, just like a superfluid, is irrotational, unless the phase of the wave function has a singularity.

From the single-valuedness of the condensate wave function it results that around a closed loop the change in the phase $\Delta S(\mathbf{r}, t)$ of the wave function

must be a multiple of 2π. Hence, the circulation Γ around a closed loop is then given by

$$\Gamma = \oint \mathbf{v}_s \cdot d\mathbf{l} = 2\pi j \frac{\hbar}{m} \quad , \tag{2.53}$$

where j is an integer. One finds that the circulation is quantized in units of h/m. Assuming an azimuthal flow in a cylindrical trap, which is invariant under the rotation about the z-axis, the condensate's wave function has then to vary as $e^{ij\phi}$, where ϕ is the azimuthal angle, due to the single-valuedness of the wave function. The velocity is then

$$v_\phi = \frac{\hbar}{m}\frac{j}{r} \quad , \tag{2.54}$$

with r being the distance from the trap axis. For $j \neq 0$ the condensate wave function must vanish, otherwise the kinetic energy diverges due to the azimuthal motion. The density of the gas must approach the unperturbed value $|\Psi_0| \to \sqrt{n}$ for large distances from the vortex. The exact solution for the density distribution near a vortex can be obtain by the ansatz

$$\Psi_0 = \sqrt{n} f(\eta) e^{ij\phi} \quad , \tag{2.55}$$

where $f(\eta)$ is a dimensionless function of the radial coordinate in units of the healing length:

$$\eta = r/\xi \quad . \tag{2.56}$$

The function $f(\eta)$ is real and fulfills the equation

$$\frac{1}{\eta}\frac{\mathrm{d}}{\mathrm{d}\eta}\left(\eta\frac{\mathrm{d}f}{\mathrm{d}\eta}\right) + \left(1 - \frac{j^2}{\eta^2}\right) f - f^3 = 0 \tag{2.57}$$

with the constraint $f(\infty) = 1$. Figure 2.3 shows the solution of $f(\eta)$ for $j = 1$ and $j = 2$. For $\eta \to 0$ the solution of equation (2.57) tends to zero as $f \sim \eta^{|j|}$, ensuring that $n(\mathbf{r}) = |\Psi_0|^2$ tends to zero on the axis of the vortex. One finds, that the core of the vortex line, the region where the density is perturbed in a significant way, is on the order of the healing length.

Solitons

The second example for a physical effect that is diagnosed by a signature imprint in the density distribution of a BEC is a soliton. A soliton is a special solution of the time-dependent Gross-Pitaevskii equation (2.42) [47], which present itself as a localized modulation of the density profile moving at a constant velocity in the medium without loosing its intrinsic shape.

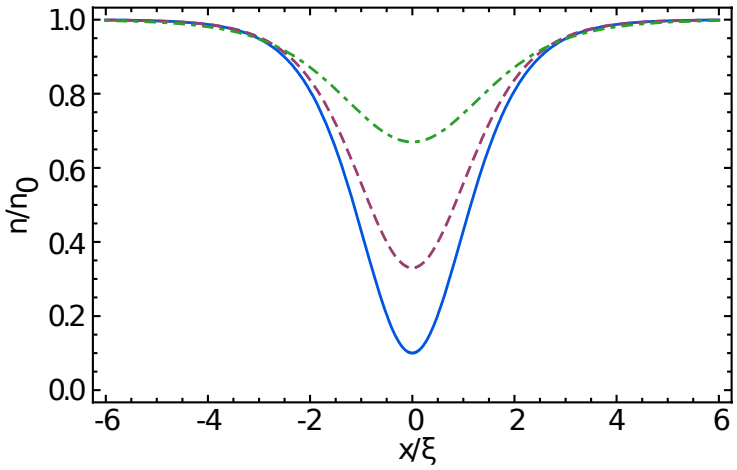

Figure 2.4: Density profile of a dark soliton. The graphs shows the density profiles for three different soliton velocities. The blue, solid line corresponds to $v^2 = 0.1c^2$, while the red, dashed and the green, dash-dotted line depicts the density profiles with $v^2 = 0.33c^2$ and $v^2 = 0.66c^2$, respectively.

Solitons exist for a various number of nonlinear equations and have first been observed in shallow water waves [59].

The perturbation of the density is characterized by a suppression of the density with respect to the density of the undisturbed region, a so called dark soliton. The typical length scale on which the density is modified is again featured by the healing length ξ. A solution in one dimension is described by the distribution [46]

$$n\left(x - vt\right) = n_0 \frac{v^2}{c^2} + n_0 \left(1 - \frac{v^2}{c^2}\right) \tanh^2 \left[\frac{x - vt}{\sqrt{2}\xi}\sqrt{1 - \frac{v^2}{c^2}}\right] \quad , \qquad (2.58)$$

where v is the velocity of the soliton, n_0 the density of the unperturbed system, and c the speed of sound in the system. From equation (2.58) one finds that the width of the soliton is fixed by the healing length, but it is amplified by the factor $\left(1 - \frac{v^2}{c^2}\right)^{-1/2}$ which diverges for $v \to c$. Figure 2.4 shows the density profiles of a dark soliton for different soliton velocities.

2.2 Ground State of a Trapped Bose Gas

In an experiment with ultracold quantum gases the atoms have to be confined in an external trapping potential and they cannot be assumed to be non-interacting. Therefore, the emphasis of this chapter is to indicated how the combined effects of Bose-Einstein condensation, nonuniform external trapping, and two-body interactions characterize the ground state properties of the system.

2.2.1 Thomas-Fermi Limit

The potential energy of a non-interacting bosonic particle in a harmonic trap is

$$E_{\mathrm{pot}}^{\mathrm{harm}} \propto \frac{1}{2} m \omega_{\mathrm{ho}}^2 \Delta R^2 \quad , \tag{2.59}$$

where $\omega_{\mathrm{ho}} = (\omega_x \omega_y \omega_z)^{1/3}$ denotes the geometrical averaged oscillator frequency of the harmonic trap. The spatial extension of the cloud ΔR is characterized by the oscillator length

$$a_{\mathrm{ho}} = \sqrt{\frac{\hbar}{m \omega_{\mathrm{ho}}}} \quad , \tag{2.60}$$

which is the characteristic quantum-mechanical length scale for the harmonic oscillator. From Heisenberg's uncertainty principle we can deduce that the particle momentum is of the order of $\hbar/\Delta R$, which results in a kinetic energy

$$E_{\mathrm{kin}}^{\mathrm{harm}} \propto \frac{\hbar^2}{2m\Delta R^2} \quad . \tag{2.61}$$

Thus, in absence of interaction the total energy varies as $1/\Delta R^2$ for small ΔR and as ΔR^2 for large ΔR. The total energy is minimal for equal kinetic and potential energy. This equilibrium is changed for interacting bosons. For an ensemble with a number of particles N, the particle density is given by

$$n \propto \frac{N}{\Delta R^3} \quad . \tag{2.62}$$

Hence, the interaction energy of a particle is of the order of (cf. (2.25))

$$E_{\mathrm{int}}^{\mathrm{harm}} \propto \frac{gN}{\Delta R^3} = \frac{4\pi\hbar a N}{m \Delta R^3} \quad . \tag{2.63}$$

For a repulsive interaction, the minimum of total energy is shifted to larger values of ΔR, and consequently, for increasing values of aN, the kinetic

energy term becomes less important. For sufficiently large clouds, one can therefore calculate the ground-state energy by neglecting the kinetic energy term in the stationary Gross-Pitaevskii equation. Equation (2.49) then simplifies to

$$\left[V_{\text{ext}}\left(\mathbf{r}\right) + g|\Psi_{\text{TF}}\left(\mathbf{r}\right)|^2\right]\Psi_{\text{TF}}\left(\mathbf{r}\right) = \mu_{\text{TF}}\Psi_0(\mathbf{r}) \quad . \tag{2.64}$$

This equation has the solution

$$n_{\text{TF}}\left(\mathbf{r}\right) = |\Psi_{\text{TF}}\left(\mathbf{r}\right)|^2 = \frac{1}{g}\left[\mu_{\text{TF}} - V_{\text{ext}}\left(\mathbf{r}\right)\right] \tag{2.65}$$

in the region where the right hand side is positive, while the wave function Ψ_{TF} vanishes outside this region. Hence, the cloud's boundary is given by

$$V_{\text{ext}}\left(\mathbf{r}\right) = \mu_{\text{TF}} \quad . \tag{2.66}$$

The physical meaning of the approximation is that the energy to add a particle at any point in the cloud is everywhere the same. This energy consists of the sum of the external potential $V_{\text{ext}}\left(\mathbf{r}\right)$ and an interaction contribution $gn_{\text{TF}}\left(\mathbf{r}\right)$ which is given by the chemical potential of a uniform gas with a density equal to the local density $n_{\text{TF}}\left(\mathbf{r}\right)$. Thus, this approximation is reminiscent of the Thomas-Fermi approximation in the theory of atoms [60] and is therefore referred to by the same name [46]. The Thomas-Fermi approximation is valid if the so called Thomas-Fermi parameter is very large:

$$N\frac{a_s}{a_{\text{ho}}} \gg 1 \quad . \tag{2.67}$$

The value of the chemical potential is obtained by the normalization of the density and given by

$$\mu_{\text{TF}} = \frac{\hbar\omega_{\text{ho}}}{2}\left(\frac{15a_sN}{a_{\text{ho}}}\right)^{\frac{2}{5}} \quad . \tag{2.68}$$

From equation (2.65) it is found that the density profile of the trapped Bose-Einstein condensate in the Thomas-Fermi limit takes the form of an inverted parabola which vanishes at the classical turning points, characterized by the three radii R_l of the ellipsoid. The relation

$$\mu_{\text{TF}} = \frac{1}{2}m\omega_l^2R_l^2 \quad , \tag{2.69}$$

where the index l denotes the three spatial axes, fixes the values of the ellipsoid's radii to the oscillator frequencies. Using the expression for the chemical potential given in equation (2.68) the radii R_l can be written as

$$R_l = a_{\text{ho}}\left(\frac{15a_sN}{a_{\text{ho}}}\right)^{\frac{1}{5}}\frac{\omega_{\text{ho}}}{\omega_l} \quad . \tag{2.70}$$

In contrast to the size of a Bose condensed ideal gas, which is fixed by the oscillator length and independent of the number of contained particles N, the condensate size in the Thomas-Fermi limit increases with $N^{1/5}$.

The region where the Thomas-Fermi density (2.65) is deficient, is close to the classical turning points. The shape of the outer part of the condensate is determined by the balance between the external potential and the zero point kinetic energy.

2.2.2 Semi-Ideal Model

In all the discussed models so far the interaction between the condensate and atoms in the thermal cloud has been neglected. This interaction can be included by introducing an effective potential V_{eff}. In the cases of an ideal gas this effective potential reduces to the external potential. A model which takes into account that the condensate actually repels the thermal cloud, is the so-called semi-ideal model [61, 62, 63]. This model considers a condensate containing $N_0 < N$ atoms plus a ideal thermal gas moving in the combined trapping plus condensate potential. This effective potential is given by

$$V_{\text{eff}}(\mathbf{r}) = V_{\text{ext}}(\mathbf{r}) + 2g|\Psi_0(\mathbf{r})|^2 \quad . \tag{2.71}$$

The factor two accounts for exchange collisions between atoms in different quantum states and the condensate wave is normalized to the number of condensed atoms. The density distribution of the thermal component is given by

$$n_{\text{th}} = \frac{g^{3/2}(z)}{\lambda_{\text{th}}^3} \quad , \tag{2.72}$$

with the modified fugacity

$$z = \exp\left[\frac{-\left(V_{\text{eff}}\left(\mathbf{r}\right) - \mu\right)}{k_B T}\right] \quad . \tag{2.73}$$

Here, $\lambda_{\text{th}} = \sqrt{2\pi\hbar^2/mk_BT}$ is the thermal de Broglie wavelength. The total number of atoms is

$$N = N_0 + N_{\text{th}} = N_0 + \int n_{\text{th}} d\mathbf{r} \quad . \tag{2.74}$$

The semi-ideal model predicts the repulsion of the thermal component by the condensate which is an important feature in the static density profile of trapped interacting Bose gases. This is caused because the density of the

condensate greatly exceeds the density of the thermal component, even if the condensate fraction is only a few percent. The condensate mean-field is therefore stronger and repels the thermal cloud from the center of the trap, digging a hole into the thermal distribution.

Chapter 3

Imaging Ultracold Atoms

In the past years the field of ultracold quantum gases experienced an enormous progress. Initially, the research focused on weakly interacting quantum gases, e.g. states of weakly interacting quantum gases [11]. More recently, the interest has turned towards strongly interacting bosonic [23, 64, 65] and fermionic systems [66, 67, 68, 69] realized with and without optical lattices [28]. Despite the fact that the research area covers a lot of different sub-fields the information about the prepared physical system is usually obtained by imaging the density distribution of the atom cloud. Depending on the system under investigation a range of optical and non-optical imaging methods is available, each with its own benefits and drawbacks.

The aim of the presented work is the implementation and characterization of a new imaging method with high spatial resolution for ultracold atoms which uses scanning electron microscopy techniques [70] instead of optical imaging techniques. In order to give an overview of the strengths and limitations of the common imaging methods we will start this chapter by briefly reviewing typical imaging techniques. After this we will concentrate on electron-atom scattering processes, and end this chapter with a short discussion on the expected interaction cross sections and the resulting detection efficiency and speed.

3.1 Imaging Methods for Ultracold Quantum Gases

The length scale of characteristic spatial structures in Bose-Einstein condensates such as vortices and solitons is determined by the healing length

as discussed in chapter 2.1.5. In the case of ^{87}Rb, typical condensate densities are between $10^{13}\,\mathrm{cm}^{-3}$ and $10^{15}\,\mathrm{cm}^{-3}$, providing a range from several hundred to one hundred nanometers for the corresponding healing length. Furthermore, in optical lattice systems the smallest structure is the spacing between sites, typically $0.5\,\mu$m. In order to visualize and measure these structures an imaging system with an adequate spatial resolution is needed. In addition, to address and observe single atoms on single lattice site, an imaging method is needed that combines high spatial resolution with single atom sensitivity.

The possible imaging methods for ultracold atoms can be separated into two classes: optical and non-optical imaging techniques. By far the most methods, including the most common ones, use optical imaging. However, several non-optical imaging methods have been developed to target special problems unaccessible to optical imaging.

3.1.1 Optical Imaging Methods

All optical imaging method have in common that the spatial resolution is fundamentally limited[1] by the wavelength of the imaging light. The minimum distance r of two points that can be resolved by an optical system, is given by the wavelength λ of the light which is used for the imaging process and the numerical aperture of the imaging system NA. This distance can be expressed in the so-called Abbe criterion

$$r = \frac{\lambda}{2\,NA} \quad . \tag{3.1}$$

The numerical aperture is determined by the refractive index n of the surrounding medium and the opening half angle θ of the optical system

$$NA = n\sin(\theta) \quad . \tag{3.2}$$

Also common to all optical imaging is that the fundamental process is the interaction between atoms and light. The atoms can influence the light in three different ways: spontaneous absorption of photons, re-emission of photons, and shifting the phase of the transmitted light. The interaction

[1] In the stimulated-emission-depletion fluorescence [71] and in near-field scanning optical microscopy [72], resolutions beyond Abbe's law have been achieved. However, for standard linear optical systems such as presented in this chapter this law is still valid.

can be described by the complex refraction index of the atoms, which for a two-level system can be expressed as [73]:

$$n_{\mathrm{ref}}(x,y) = 1 + n(x,y) \cdot \frac{\sigma_0 \lambda}{4\pi} \left[\frac{i}{1 + (I/I_{\mathrm{sat}})\,\delta^2} - \frac{\delta}{1 + (I/I_{\mathrm{sat}})\,\delta^2} \right]. \tag{3.3}$$

Here, n represents the density of the atoms, σ_0 denotes the resonant light cross section, I stands for the light intensity, I_{sat} for the saturation intensity of the transition, and

$$\delta = \frac{\omega - \omega_0}{\Gamma/2} = \frac{\Delta}{\Gamma/2} \tag{3.4}$$

is the detuning in half line widths. The frequency of the light field is denoted by ω and ω_0 labels the atomic transition frequency.

A light wave $\mathbf{E}(x,y,z,t)$ which passes through an atomic cloud is attenuated and phase shifted by the atoms. The outgoing light field, propagating in the $\hat{\mathbf{e}}_z$ direction is given by

$$\mathbf{E}'(x,y,z,t) = \mathbf{E}(x,y,z,t) \exp\left[-\frac{2\pi i}{\lambda} \int \left(n_{\mathrm{ref}}(x,y) - 1\right) dz \right] \tag{3.5}$$

$$= T(x,y)\mathbf{E}(x,y,z,t) e^{i\phi(x,y)} \quad , \tag{3.6}$$

where the integral covers the whole atom cloud, $T(x,y)$ denotes the transmission coefficient, while the phase shift which the light field experiences is labeled with $\phi(x,y)$. Moreover, an important parameter is the optical density which is given by

$$D(x,y) = \frac{\sigma_0}{1+\delta^2} \int n(x,y,z)\, dz \quad , \tag{3.7}$$

where we consider resonant ($\delta = 0$) and off resonant ($\delta \neq 0$) imaging. The integral denotes the integrated column density of the atomic sample. The relation of the transmission coefficient and the phase shift to the optical density will be discussed in the following sections.

Absorption Imaging

Absorption imaging is a technique that only uses the absorption of resonant light ($\delta = 0$) in an atom cloud. The atoms are illuminated with a resonant laser beam and the shadow cast by the atoms is imaged with the aid of an optical system onto a two-dimensional detector, typically a charged coupled device (CCD) camera. The principle of absorption imaging is depicted in

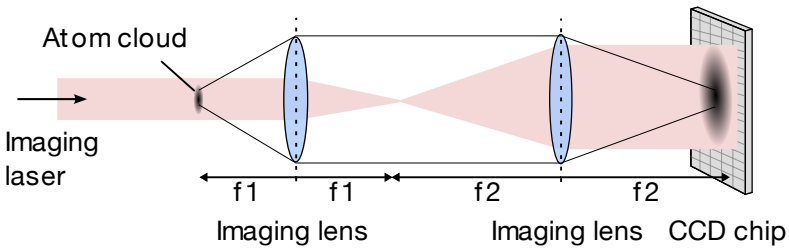

Figure 3.1: Principle of absorption imaging. A resonant laser pulse illuminates the atom cloud. The light is absorbed by the atoms and suffers attenuation, which results in a shadow. This shadow is magnified with a lens system and imaged onto a CCD-chip.

figure 3.1.

The density distribution of the imaged cloud is obtained by measuring the attenuation of the light in the atom cloud. If the direction of the incident imaging beam is given by $\hat{\mathbf{e}}_z$, the attenuation of the probe beam intensity is given by $T(x,y)^2$. The intensity $I_1(x,y)$ of the imaging laser after it passed the atoms is

$$I_1(x,y) = T(x,y)^2 I_0(x,y) = I_0(x,y)e^{-D(x,y)} \quad , \tag{3.8}$$

where $I_0(x,y)$ labels the intensity of the light before the atom cloud, and $D(x,y)$ is the optical density from equation (3.7). The column density can be obtained by comparing an image with atoms, with an image without atoms and is given by

$$\int dz\, n(x,y,z) = -\frac{1}{\sigma_0} \ln \frac{I_1(x,y)}{I_0(x,y)} = \frac{1}{\sigma_0} D(x,y) \quad . \tag{3.9}$$

The absorption imaging technique can in principle be applied to a trapped sample but those are usually small in size and have high optical densities. Depending on the numerical aperture of the imaging system, the size of the trapped cloud of atoms, could be smaller than the diffraction limit, so that the shape of the sample cannot be obtained. The high optical density will essentially absorb all probe light, causing $D(x,y)$ to diverge. The problem of the high optical density can be overcome by the so called time of flight (TOF) method where the cloud expands during a free fall of several millisecond. Due to the expansion the cloud gets larger resulting in a reduced

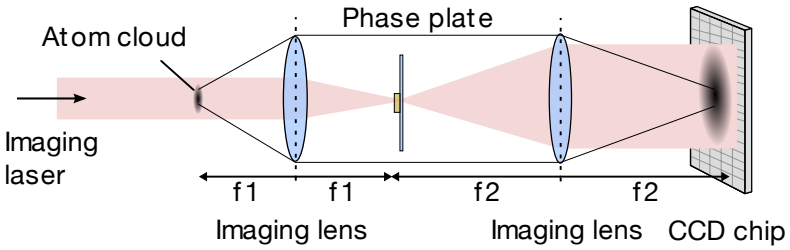

Figure 3.2: Principle of phase contrast imaging. A part of the incident detuned light is diffracted by the atom cloud which acts like a phase object. The non-diffracted part forms the reference beam. Both components are collected by an imaging lens and spatially separated in the back focal plane. The phase of the reference beam is shifted by $\phi = \pm\pi/2$ using a phase plate. The two components are then recombined by a second lens and interfere at the image plane, forming the phase contrast image.

optical density and $D(x, y)$ no longer diverges. A consequence of the TOF method is that the information about the spatial distribution of the ensemble in the trap is lost.

An advantage of absorption imaging is that all atoms are detected at once. On the downside, due to the use of resonant imaging light, which causes the atom cloud to heat up, the evolution of an atomic ensemble cannot be observed over a period of time.

Phase Contrast Imaging

Information about the density of a system can also be obtained by measuring the phase shift that a probe beam experiences when passing an atom cloud. This method is know as phase contrast imaging [73, 74, 75] and like other dispersive methods it relies on the ability to separate scattered and unscattered components of the probe light and manipulate them independently. Phase contrast imaging can be regarded as a homodyne detection scheme in which the unscattered light acts as the local oscillator and interferes with scattered part of the probe beam. This is achieved by shifting the phase of the unscattered light by $\pi/2$ in the Fourier plane of the imaging system using a phase plate, as it can be seen in figure 3.2. The intensity on

the CCD chip in the image plane is given by [76]

$$I = I_0 \left[T^2 + 2 - 2\sqrt{2}t \cos\left(\phi \pm \frac{\pi}{4}\right)\right] \xrightarrow{\phi \text{ small}} I_0 \left[T^2 + 2 - 2T \pm T\phi\right] . \tag{3.10}$$

The phase shift ϕ can be expressed by:

$$\phi(x, y) = \frac{\delta}{2} D(x, y) \quad . \tag{3.11}$$

The $\pm$ sign in equation (3.10) corresponds to the phase shift of the unscattered light by $\pm\pi/2$. Since phase contrast imaging uses off-resonant light, in contrast to absorption imaging, it allows for the *in situ* observation of the time evolution of an individual atom cloud [77].

Fluorescence Imaging

Fluorescence imaging detects the light which is emitted by an atom that is illuminated by resonant light. A simple illustration of the method is shown in figure 3.3. The spatial resolution of this method is limited by equation (3.1) and depends on the wavelength of the fluorescence light and the available numerical aperture. The time it takes to capture enough signal intensity for a measurement depends on the number of fluorescing atoms. While the fluorescence light of 10^5 atoms can be captured in a few microseconds, the measurement of a single atom typically needs some tens of milliseconds. During the measurement the atom is heated due to the absorbed and re-emitted light, it is therefore necessary to confine the imaged atom in a sufficiently deep trap to keep it in place and cool it during the imaging process.

A recent experiment has demonstrated a resolution of 600nm for an imaging wavelength of 780 nm and $NA = 0.8$ [78].

3.1.2 Non-Optical Imaging

The class of non-optical imaging detects the particle directly instead of imaging it with light. In the case of metastable helium, which has an internal energy of 20 eV, the particle can be detected by a multi channel plate (MCP).

The cloud of ultracold atoms is trapped above a MCP detector. The atoms are released from the trap and accelerated in $\hat{e}_z$ direction towards the detector due to gravity. The $(\hat{e}_x, \hat{e}_y)$-position of the particles is given directly

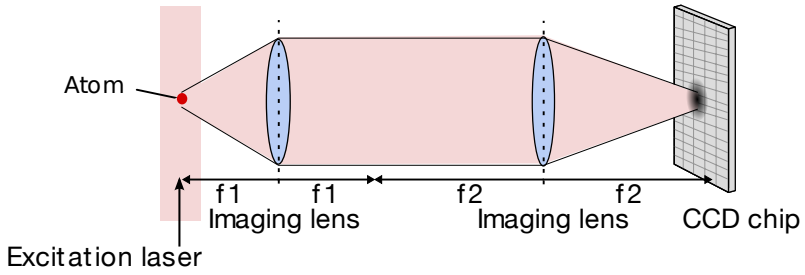

Figure 3.3: Principle of fluorescence imaging. The trapped atom is illuminated with a light beam. The atom absorb the light and emits photons isotropically. The fluorescence light is collected by an imaging system and detected by either a CCD-camera or a photo diode.

from the detector and the $\hat{e}_z$-position is obtained by the time of flight. The resolved distances between two particles are $d \approx 250\ \mu$m in the $(\hat{e}_x, \hat{e}_y)$-direction and $d \approx 2\,$nm in $\hat{e}_z$-direction [79]. Due to the high signal to noise ratio the method is single atom sensitive. The technique features a high spatial resolution in one dimension, but it is incapable of *in-situ* measurements and restricted to a specific class of atoms.

An alternative method is to first ionize the neutral atoms locally and subsequently extract and detect the produced ions. An atom chip experiment demonstrated this detection scheme using photo ionization to ionize ultracold magnetically trapped atoms [80]. The scheme uses two optical transitions, the first transition resonantly excites the atoms from the 5S ground state using a two-photon transition into the 5D state. Before decaying back into the ground state the atoms are ionized by the second transition. Position control is achieved by preparing the atoms in the $|F = 2, m_F = 2\rangle$ hyperfine level of the ground state. The first laser is in resonance with the $|F = 1, m_F = 1\rangle$ hyperfine state so that a coupling between the prepared ground state and the excited state is only possible if an additional microwave frequency of 6.83 GHz is present. By applying a magnetic field gradient one gains spatial control over the system due to the Zeeman effect which changes the energy difference between both hyperfine states depending on the magnetic field. The ionization process is only possible by coupling the two states with a matching microwave frequency, which can be tuned to address the desired positions along the magnetic field gradient [81]. So far the scheme has been implemented [82], but the possible spatial resolution has not yet been explored.

3.2 Electron Microscopy of Ultracold Atoms

Since the spatial resolution of an imaging system is fundamentally limited by the wavelength of the imaging light, expressed in the Abbe criterion (3.1), it can be improved by using a smaller wavelength. A common high resolution imaging technique is scanning electron microscopy (see [83] and references therein), which allows imaging of solid surfaces and structures with a resolution of a few nanometers and below. Instead of light this method utilizes a beam of electrons which scans the object. The impact of an electron on the surface of the sample leads to the emission of secondary electrons and the backscattering of the particle, depending on the incident energy. By either measuring the secondary or backscattered electrons, an image of the scanned surface is obtained.

In the following we describe how this technique is extended to ultracold quantum gases in combination with electron impact ionization. When trying to image a gaseous target with the aid of scanning electron microscopy, the detection method must be slightly altered. The working principle of the method is the as follows: a focused electron beam is moved over the ultracold quantum gas and locally produces ions, based on electron-atom scattering interactions. Subsequent detection of the ions allows for the reconstruction of the atoms position where the ionization process occurred. The working principle is illustrated in figure 3.4.

This section introduces the possible processes that occur in electron-atom scattering interactions with a short overview of the common approximation methods to calculate the scattering cross sections of those processes.

3.2.1 First Born Approximation

The interaction between electrons and atoms is characterized by scattering theory which is has been discussed in 2.1.2 with an emphasis on collisions between ultracold atoms. However, to describe the scattering of incident electrons from an focused electron beam with atoms different approximation methods have to be employed due to the high energy of the collision.

From equation (2.16) we know that the differential cross section can be computed from the form factor of the scattering potential, which is defined in equation (2.13). Furthermore, equation (2.13) represents an integral equa-

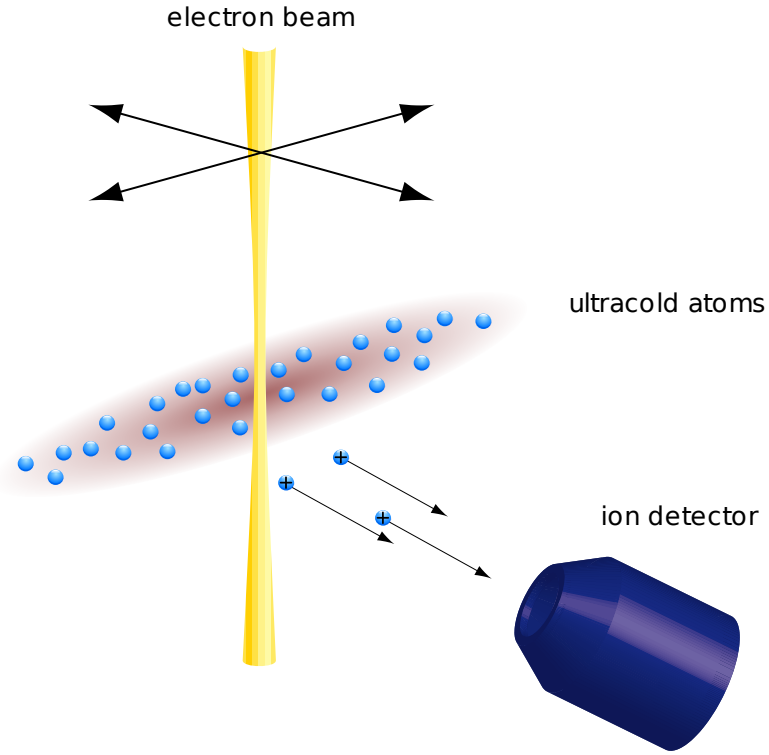

Figure 3.4: Working principle of scanning electron microscopy applied to ultracold quantum gases. A focused electron beam is scanned over the atom cloud and ionizes single atoms, which are subsequently detected by an ion detector [70].

tion for the unknown wave function $\Psi_k(\mathbf{x})$. If the effect of the scatter is not very strong, the scattering potential can be considered as perturbation to the solution

$$\Psi_k^0(\mathbf{x}) = \frac{1}{(2\pi)^{3/2}} e^{i\mathbf{k}\cdot\mathbf{x}} \quad . \tag{3.12}$$

The final wave function is then represented by the series

$$\Psi_k(\mathbf{x}) = \sum_{n=0}^{\infty} \Psi_k^n(\mathbf{x}) \tag{3.13}$$

with $\Psi_k^n(\mathbf{x})$ given by [41, 84]

$$\Psi_k^n(\mathbf{x}) = -\frac{2m}{4\pi\hbar^2} \int d^3x' \frac{e^{i\mathbf{k}\cdot|\mathbf{x}-\mathbf{x}'|}}{|\mathbf{x}-\mathbf{x}'|} V(\mathbf{x}') \Psi_k^{n-1}(\mathbf{x}) \quad . \tag{3.14}$$

If one restricts the expansion to $n = 1$, which is known as the first Born approximation one finds that in this approximation the form factor is simply given by the Fourier transformation of the scattering potential:

$$f^1(\mathbf{k}, \mathbf{k}') = -\frac{2m}{4\pi\hbar^2} \int d^3x \, e^{i(\mathbf{k}-\mathbf{k}')\cdot\mathbf{x}} V(\mathbf{x}) \quad . \tag{3.15}$$

3.2.2 Electron Atom Interaction

The processes that occur due to the interaction between the electron beam and the atoms are elastic and inelastic scattering. The ionization of atoms due to the interaction with the electron beam is a special case of inelastic scattering and is called electron impact ionization. Since the imaging technique presented in this work uses these ionized atoms, we will consider electron impact ionization as an independent process.

Elastic scattering means that the internal state of the target atom remains unchanged during the scattering process. Since energy and momentum are conserved in this scattering process, the scattered atom carries some energy and momentum of the incident electron. Due to the transfered energy such an atom can gain enough kinetic energy to leave the trap. Since in the scheme described in this section only ions are detected, this process leaves no detectable signal it is a pure loss channel. In the second process, inelastic scattering, the internal state of the target atom is changed. The atom which has been hit is in principle "marked" and could, for example with some post ionization scheme be detected [85]. If no such post ionization scheme is implemented it is a loss channel as well. Electron impact ionization is the process where the the incident electron knocks out a bound electron from the target atom. The remaining ion can be extracted and detected with the aid of ion optics and detector.

Elastic and Inelastic Scattering

In the case of elastic scattering between an electron and a neutral atom, one assumes that the atom is in its ground state $|\varphi_0\rangle$ and the state of the atom will remain unchanged.

The wave vector of the incident electron is denoted by $\mathbf{k}$, and $\mathbf{k}'$ is the wave vector of the outgoing electron. The plain-wave states of the electrons are then $|\mathbf{k}\rangle$ and $|\mathbf{k}'\rangle$. The initial and final states of the elastic scattering process can be written as direct products

$$|\Psi_\mathrm{i}\rangle = |\mathbf{k}\rangle \times |\varphi_0\rangle \equiv |\mathbf{k}, \varphi_0\rangle \quad , \tag{3.16a}$$

$$|\Psi_\mathrm{f}\rangle = |\mathbf{k}'\rangle \times |\varphi_0\rangle \equiv |\mathbf{k}', \varphi_0\rangle \quad . \tag{3.16b}$$

In the case of inelastic scattering between an incident electron and a neutral atom, the atom is excited into another energy eigenstate $|\varphi_n\rangle \neq |\varphi_0\rangle$. This results in a kinetic energy difference between the outgoing electron and the incident electron. The kinetic energy difference corresponds to the energy difference between the initial and final internal state. The initial and the final state of the scattering process is again given by direct products

$$|\Psi_\mathrm{i}\rangle = |\mathbf{k}\rangle \times |\varphi_0\rangle \equiv |\mathbf{k}, \varphi_0\rangle \quad , \tag{3.17a}$$

$$|\Psi_\mathrm{f}\rangle = |\mathbf{k}'\rangle \times |\varphi_n\rangle \equiv |\mathbf{k}', \varphi_n\rangle \quad . \tag{3.17b}$$

The elastic and inelastic scattering cross section in first Born approximation (3.14) is discussed in detail in [41, 86, 87, 88] and we will therefore give only a brief summary of the subject.

The scattering potential V where an incident electron interacts with the nucleus, assumed in the origin, and with each atomic electron, is

$$V = -\frac{Ze^2}{|\mathbf{x}|} + \sum_j^Z \frac{e^2}{|\mathbf{x} - \mathbf{x_j}|} \quad , \tag{3.18}$$

for a neutral atom with Z protons and electrons. Note, the potential is given in atomic units. The differential cross section can then be written as [41]

$$\frac{d\sigma}{d\Omega}(0 \to n) = \frac{4m^2Z^2e^4}{\hbar^4 q^4}\left(\frac{k'}{k}\right)|F_n(\mathbf{q}) - \delta_{n0}|^2 \quad , \tag{3.19}$$

where δ_{nm} denotes the Kronecker symbol and F_n is a modified form factor defined as follows:

$$ZF_n(\mathbf{q}) = \langle\varphi_n| \sum_j e^{i\mathbf{q}\cdot\mathbf{x_j}} |\varphi_0\rangle \quad , \tag{3.20}$$

with $\mathbf{q} \equiv \mathbf{k} - \mathbf{k}'$.

The elastic scattering differential cross section [41, 86] is obtained from equation (3.19) as the special case of n=0:

$$\frac{d\sigma_\mathrm{el}}{d\Omega}(\varphi_0 \to \varphi_0) = \frac{4m^2Z^2e^4}{\hbar^4 q^4}|F_0(\mathbf{q}) - 1|^2 \quad , \tag{3.21}$$

and can be computed if the ground state wave function is known. To retrieve the total elastic cross section equation (3.21) has to be integrated over the solid angle $d\Omega$. For a spherically symmetric atom this yields [86]

$$\sigma_{\mathrm{el}} = 2\pi \left(\frac{2me^2}{\hbar^2 k}\right)^2 \int_0^\infty \frac{dq}{q^3} |F_0(\mathbf{q}) - 1|^2 \quad . \tag{3.22}$$

Thus, the total elastic scattering cross section as a function of energy is proportional to $1/E$ for large energies.

The differential inelastic scattering cross section is obtained by summing the cross sections for scattering from the ground state $|\varphi_0\rangle$ to any excited state $|\varphi_n\rangle$:

$$\frac{d\sigma_{\mathrm{inel}}}{d\Omega} = \sum_{n\neq 0} \frac{d\sigma}{d\Omega}(\varphi_0 \to \varphi_n) = \sum_{n\neq 0} \frac{4m^2 Z^2 e^4}{\hbar^4 q^4} \left(\frac{k'}{k}\right) |F_n(\mathbf{q})|^2 \quad . \tag{3.23}$$

Note that $|\mathbf{k}|$ is not equal to $|\mathbf{k}'|$. To obtain the total inelastic scattering cross section, equation (3.23) has to be integrated over the solid angel $d\Omega$. In the nonrelativistic case this is given by [88]

$$\sigma_{\mathrm{inel}} = \frac{4\pi a_0}{E/R} \left[M_{\mathrm{tot}} \ln\left(\frac{4c_{\mathrm{tot}} E}{R}\right) + \frac{\gamma_{\mathrm{tot}}}{E/R} + \mathcal{O}\left(\frac{R^2}{E^2}\right)\right] \quad , \tag{3.24}$$

where $R = \frac{me^4}{2\hbar^2} = 13.606\,\mathrm{eV}$ represents the Rydberg energy and M_{tot}, c_{tot}, and γ_{tot} are constants which are discussed in [88]. Hence, the total inelastic scattering cross section as a function of energy is proportional to $\ln E/E$.

Electron Impact Ionization

The special case of single electron impact ionization is a three body process. The initial and final states are again given by the direct products

$$|\Psi_{\mathrm{initial}}\rangle = |\mathbf{k}\rangle \times |\varphi_0\rangle \equiv |\mathbf{k}, \varphi_0\rangle \quad , \tag{3.25a}$$

$$|\Psi_{\mathrm{final}}\rangle = |\mathbf{k}'\rangle \times |\mathbf{k}''\rangle \times |\varphi^*\rangle \equiv |\mathbf{k}', \mathbf{k}'', \varphi^*\rangle \quad , \tag{3.25b}$$

this time φ^* denotes the wave function of an ionized atom and $\mathbf{k}''$ is the wave vector of the additional, ejected electron after the ionization.

The three-body problem has no general valid method for calculating the solution, but several kinematic regions can be described separately [89]. In the so called *binary regime*, all of the momentum is transfered from the

incident electron to the ejected electron by a direct collision between them. The assumption that the incident electron interacts only with the ejected electron and does not interact with the target ion, is the basis of the *impulse regime*. In this approximation, the wave function for the target is represented by the isolated-target wave function and the final-residual ion wave function is given by the isolated wave function of the ion. Combining plane waves with impulse approximation gives the *plane-wave impulse approximation* (PWIA) where the incident, scattered, and ejected electrons are considered to be plane waves. The differential cross section for this process is given by [89]

$$\frac{d^3\sigma_{(e,2e)}}{d\Omega d\Omega'' dE''} = \frac{4m^2e^4}{\hbar^4 K^4}\left(\frac{k'k''}{k}\right)\left|\langle\varphi^*\left(\mathbf{x}\right)|e^{\frac{i\mathbf{q}\cdot\mathbf{r}''}{\hbar}}|\varphi_0\left(\mathbf{x}\right)\rangle\right|^2 \quad , \tag{3.26}$$

where $-\hbar\mathbf{q} = \hbar\mathbf{k} - \hbar\left(\mathbf{k}' + \mathbf{k}''\right)$ is the recoil momentum of the residual ion resulting from the ejection of the target electron and $\hbar\mathbf{K}$ is the difference between the momentum of the incident electron $\hbar\mathbf{k}$ and the scattered electron $\hbar\mathbf{k}'$. The total electron impact ionization cross sections can be calculated numerically [90, 91].

Cross Sections and Characteristics of the Imaging Process

The electron column, which is used in the experiments presented in this work, provides a focused electron beam with an energy between 1.7 keV and 6 keV, where the latter energy constitutes the main working point. The total cross section for the scattering system of electron and rubidium has so far not been measured for an electron beam with kinetic energy of about 6 keV, but are well examined for energies up to 500 eV [92, 93]. The total ionization cross section σ_{ion} and the total scattering cross section σ_{total} have been measured for this energy and amount to

$$\sigma_{\text{ion},500\,\text{eV}} = 2.5 \times 10^{-16}\,\text{cm}^2 \tag{3.27a}$$

$$\sigma_{\text{tot},500\,\text{eV}} = 6.2 \times 10^{-16}\,\text{cm}^2 \quad . \tag{3.27b}$$

Electron impact ionization represents about 40% of all scattering events and it is expected that this ratio remains constant for higher beam energies [94]. The probabilities for elastic and inelastic scattering can be calculated in first Born approximation to be 50% - 55% for inelastic scattering and 5% - 10% for elastic scattering.

In reference [91] the electron-impact ionization cross sections have been calculated using plane wave Born approximation for a wide range of elements

including Rb and several electron energies. The calculated electron-impact ionization cross section for an energy of 500 eV is in good agreement with (3.27a). The calculated cross section for 6 keV is specified to

$$\sigma^{\mathrm{cal}}_{\mathrm{ion,6\,keV}} = 3.5 \times 10^{-17}\,\mathrm{cm}^2 \quad . \tag{3.28}$$

If we assume that the ratio of electron impact ionization cross section to the total scattering cross section does not change for higher energies, we find from (3.28) a total scattering cross section of

$$\sigma_{\mathrm{tot,6\,keV}} = 8.8 \times 10^{-17}\,\mathrm{cm}^2 \quad . \tag{3.29}$$

In comparison, the cross section for resonant light of wavelength λ

$$\sigma_{\mathrm{opt}} = \frac{3\lambda^2}{2\pi} \approx 10^{-9}\,\mathrm{cm}^2 \tag{3.30}$$

is eight orders of magnitude larger then the cross section for electrons at 6 keV. In conclusion, since in average only one out of 500,000 electrons interacts with an atom, the atom cloud is almost transparent for the electron beam, in contrary to resonant light for which the cloud is not transparent. Thus, multiple scattering events can be neglected.

To quantify the typical time scale τ_i for ionization of an atom located in the electron beam center, the following expression has to be evaluated [70, 92]

$$\tau = \frac{q}{j_0 \sigma_{\mathrm{tot}}} \quad , \tag{3.31}$$

where j_0 denotes the central current density and q the electron charge. The time τ in equation (3.31) is defined as the time in which the "survival probability" of the atom has dropped to $1/e$. Assuming a Gaussian electron beam profile [83, 95], the current density of the electron beam is given by

$$j(\rho) = \frac{I}{2\pi\rho_0^2} e^{\frac{\rho^2}{2\rho_0^2}} = j_0 e^{\frac{\rho^2}{2\rho_0^2}} \quad , \tag{3.32}$$

where I is the beam current and ρ_0 the σ-width of the electron beam, we find a survival time of $\tau = 21\,\mu$s for a beam current of 10 nA and a FWHM[2] diameter of 100 nm, which is a typical working point of our setup. In the case that the electron beam stays at a position for a time Δt that is much

[2] **F**ull **W**idth at **H**alf **M**aximum

smaller than the lifetime τ, the probability for a scattering event to occur corresponds to [96]

$$w = 1 - e^{\frac{-\Delta t}{\tau}} \approx \frac{\Delta t}{\tau} = \frac{j_0}{e}\sigma_{\mathrm{tot}} \times \Delta t \quad . \tag{3.33}$$

This means if the electron beam stays at a position for 2 μs the probability for a scattering event is about 10%.

The detection probability of an atom at position $\{x, y\}$ is given by

$$P(x, y) = \frac{j_0}{e}\sigma_{\mathrm{ion}} \times \Delta t \times \eta_{\mathrm{det}} \times \int |\phi(x, y, z)|^2 dz, \tag{3.34}$$

where the integral denotes the density distribution of the atomic wave function ϕ integrated along the direction of the electron beam and η_{det} describes the combined detection efficiency of the detector and the ion optics.

Chapter 4

All-Optical BEC in an Electron Microscope

The main aim of the presented work is the imaging of ultracold quantum gases with the aid a focused electron beam. Hence, the atoms have to be prepared and confined in the right distance underneath the electron column. This means the trapped atoms and the lower part of the electron microscope plus the diagnostic tools have to share the same vacuum chamber. Therefore it is important that the experimental environment is not only suitable for electron microscopy but furthermore allows for the preparation of a Bose-Einstein condensate.

In this chapter, the experimental realization of the BEC is described. We begin with the description of the vacuum system and introduce the laser setup, and the magneto-optical traps, which are necessary to trap and precool the atoms. Since an all-optical approach for Bose-Einstein condensation is employed we will continue with a brief overview of the theory of optical dipole traps, before the optical dipole trap setup is introduced. The chapter ends with the realization and characterization of an all-optical Bose-Einstein condensate of ^{87}Rb atoms in an optical dipole trap formed by a focused CO_2 laser.

4.1 The Vacuum System

The vacuum system consists of two separate chambers, connected via a flexible bellow and a valve. The experiments are performed in the first chamber in the following called main chamber, and the second hosts an atom source.

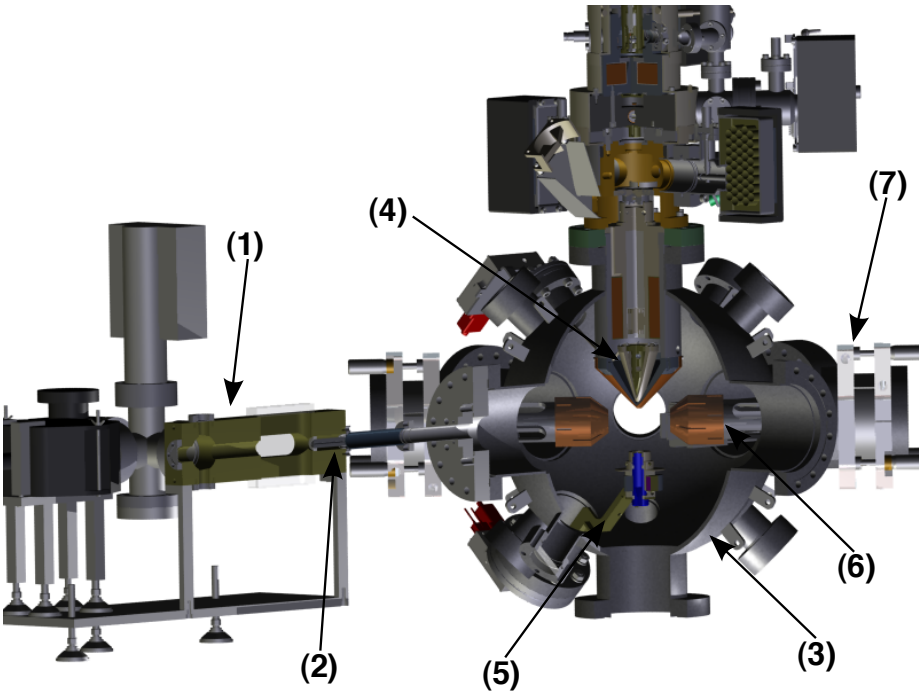

Figure 4.1: Sectional drawing of the vacuum system. On the left hand side is the titanium 2D-MOT chamber (1) which is connected to the main chamber (3) via a differential pumping section (2). The electron column (4) is mounted on top of the main chamber. The tip of the column is placed 13 mm above the center of the vacuum chamber. Underneath the tip a Faraday cup (5) is installed. The laser beam of the optical dipole trap enters the chamber from the right hand side and is focused by an aspherical lens (6) inside the chamber. The lens can be moved and adjusted via a so called port aligner (7).

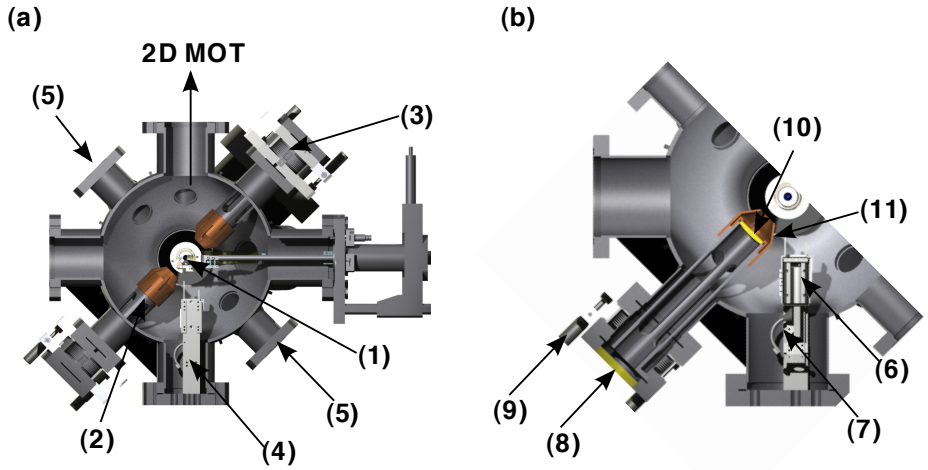

Figure 4.2: (a) Sectional drawing of the main chamber. The horizontal plane of the vacuum chamber hosts in total 8 flanges. On the right hand side is the movable test target holder (1). The lens holders (2) are mounted on bellows and can be adjusted by port aligners (3). The ion detector (4) is placed opposite to the 2D-MOT. Perpendicular to the optical dipole axis are two view-ports (5). (b) View of the lens holder and the ion detector. The ion detector consist of the ion optics (6) and a channeltron detector (7). The CO_2 laser beam enters the chamber through a ZnSn viewport (8). The lens holder itself can be adjusted with three micrometer screws (9). The ZnSn-lens (10) is mounted behind a copper protection cap (11).

The latter is a two dimensional magneto-optical trap [97, 98, 99] which will be described later in this section. The bellow guarantees, that the relative position of the two chambers to each other can be adjusted, while the valve ensures the possibility of separate ventilation. The pressure in the two chambers are 2×10^{-10}mbar and 2×10^{-7}mbar for the main and 2D-MOT chamber, respectively. The pressure difference between the two chambers is kept by a differential pumping section [100] consisting of a 5 cm long stainless steel tube with an 1.5 mm through bore-hole. The differential pumping capacity is $< 1 \times 10^{-4}$. Figure 4.1 shows an overview of the bifid vacuum system.

The main chamber, which is made of stainless steel, has a spherical shape with a diameter of 30 cm and is equipped with a total of 22 CF[1] flanges.

[1]CF - conflat

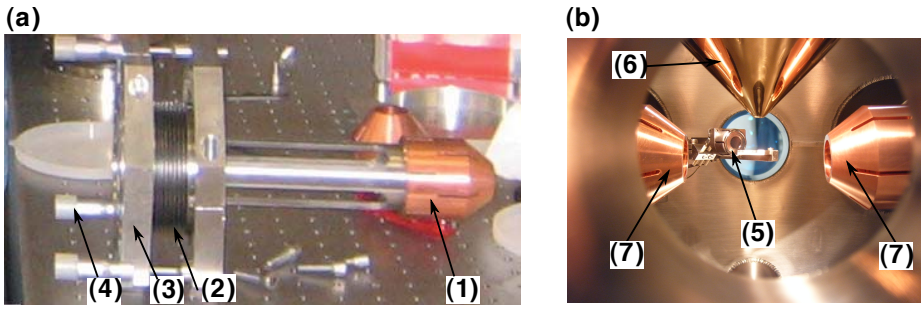

Figure 4.3: (a) Picture of the assembled lens holder. The protection caps (1) can be seen on the right end of the holder. The bellow (2) and the port aligner plates (3) with the micrometer screws (4) are on the left hand side. (b) Picture of the main chamber's interior. The movable test target holder (5) is placed underneath the tip of the electron column (6). The two lens holders (7) are on either side of the test target.

The custom made electron column[2] is placed on top of the vacuum chamber as it can be seen in figure 4.1. The lower column part, consisting of a pole piece made of an iron-nickel alloy, extends into the main chamber which is designed in such a way that the tip of the pole piece is placed 13 mm above the center of the sphere. The setup of the electron column will be described in detail in the following chapter. The current of the electron beam is measured with a Faraday cup, which is placed 5 cm underneath the tip. The ion getter pump[3] and the pressure gauge[4] are connected via a cross piece opposite to the electron column.

The horizontal plane of the chamber contains eight of the 22 flanges. They are equipped with optical viewports, the ion optics and detector, a movable test target holder[5], and the connection to the chamber of the atom source. The arrangement of these flanges can be seen in figure 4.2. The viewports windows for the CO_2 laser, which forms the optical dipole trap, are made of ZnSe[6]. The CO_2 laser beam is focused by a ZnSe lens with a focal length of 63 mm, which due to the dimensioning, is mounted by a holder inside the vacuum chamber. In order to protect the insulating lenses from possible charging, caused by statistically scattered electrons, the lenses are shielded

[2]Delong Instruments
[3]Gamma vacuum, Tall profile 150 l/s
[4]Leybold Ionivac IM 540, Gauge: IE 414
[5]VgScienta, Minax translator
[6]Zincselenide

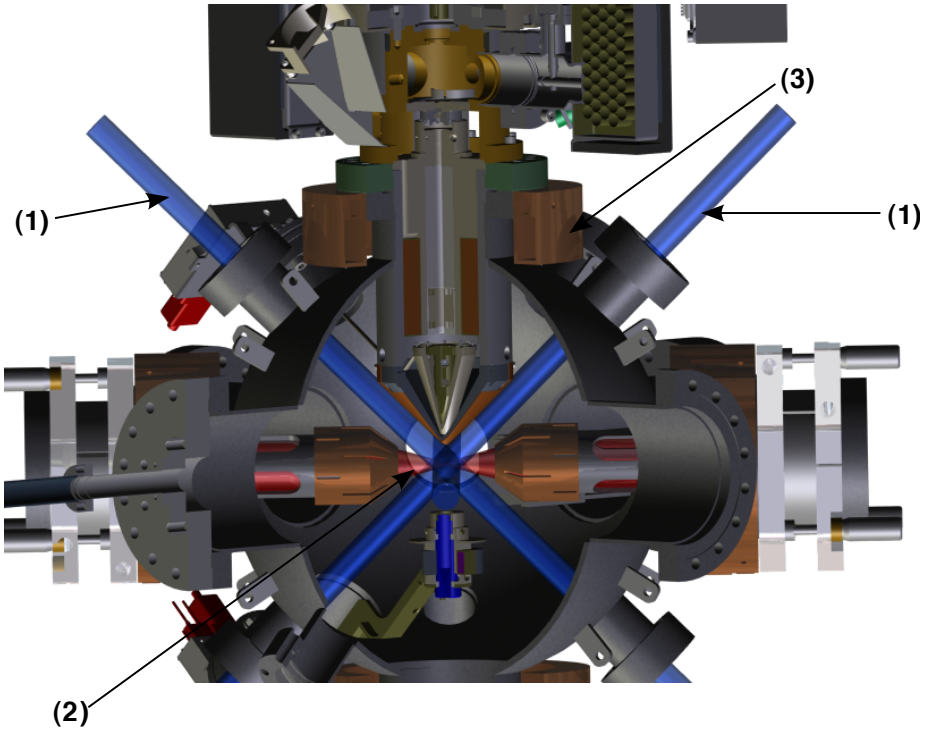

Figure 4.4: Vacuum chamber with laser beams for the 3D-MOT. The optical setup for the 3D-MOT consists of six laser beams (1) which overlap in the middle of the chamber with the optical dipole trap (2). To complete the magneto-optical trap, 6 coils (3) are mounted on the chamber.

by copper protection caps. The position of the lenses can be adjusted by moving a flexible bellow with the aid of three micrometer screws[7]. A picture of the assembled lens holder can be seen in figure 4.3. A second lens is used to collimate the beam again before it leaves the main chamber.

The viewports which provide optical access for the laser beams of the magneto-optical trap and other optical potentials are placed on the diagonal axes as it can be seen in figure 4.4.

[7]OWIS, Micrometer 25 mm travel

4.2 Realization of a Spinor Condensate in a CO_2 Dipole Trap

This section describes the experimental realization of an all-optical Bose-Einstein condensate of ^{87}Rb atoms. It contains the description of the laser system for the 2D- and 3D-MOT, in which the atoms are trapped and precooled prior to their transfer into the optical dipole trap. Apart from a characterization of the experimental setup of the CO_2 dipole trap, this chapter provides a short review of the theoretical background for the trapping of neutral atoms in optical potentials. This form of trap is discussed starting with the optical dipole potential in general before we introduce the special case of a CO_2 laser trap. The section ends with the description of the experimental cycle and the realization of an all-optical BEC.

4.2.1 Magneto-Optical-Traps

The MOT setup consists of a retro-reflected 2D-MOT [101, 102], which serves as an atom source, and a 3D-MOT in standard six-beam configuration [103]. The 2D-MOT provides a transversally precooled atom beam. This atom beam is then used to load the 3D-MOT which traps and cools the atoms further. After cooling in the 3D-MOT the atoms are loaded into the optical dipole trap.

Laser System

In order to successfully laser cool rubidium atoms two laser frequencies are required: One for the cooling and one for the repumping transition. In the case of ^{87}Rb, these correspond to hyperfine substate transitions (see figure A.1) of the D_2-line at 780 nm wavelength.

The light for the repumping transition

$$|5S_{1/2}(F=1)\rangle \rightarrow |5P_{3/2}(F'=2)\rangle$$

is provided by a grating stabilized diode laser[8] in Littrow configuration [104]. The laser wavelength is observed by a Doppler free spectroscopy [105] and stabilized with the aid of a frequency-modulated (FM) spectroscopy [106] to the (1,2) crossover peak. This crossover peak lies at an energy 78.5 MHz smaller than the actual repumping transition. The setup is pictured in figure 4.5. The laser frequency is shifted to resonance via

[8] Sharp GH0781JA2S (120 mW)

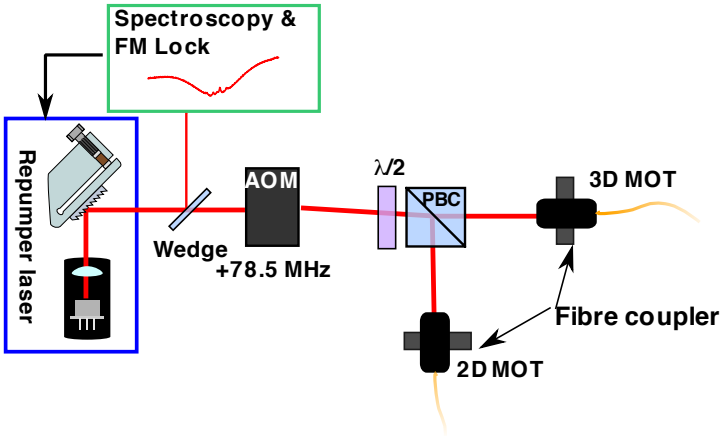

Figure 4.5: Simplified drawing of the repumper branch. A grating stabilized diode laser provides the light. An AOM makes sure that the intensity of the laser beam can be controlled. The beam is split into two by the aid of a PBC and a half wave plate and than coupled into optical fibers.

acousto-optical modulator (AOM) [107]. The light is afterwards split into two by a polarizing beam splitter cube (PBC) and each beam is coupled into a polarization maintaining single mode optical fiber. The 2D-MOT has an available repumping power of 7 mW whereas the repumping light for the 3D-MOT has 5.8 mW.

The light for the cooling transition

$$|5S_{1/2}(F=2)\rangle \rightarrow |5P_{3/2}(F'=3)\rangle$$

is provided by a tapered amplifier[9] (TA) [108], which is seeded by a grating stabilized diode laser in Littrow configuration. The frequency of the latter is shifted and stabilized with respect to the frequency of the so called master laser by means of an offset lock [109]. The wavelength of the master laser, likewise a grating stabilized diode laser in Littrow configuration, is monitored with a Doppler free spectroscopy and stabilized with a FM spectroscopy to the (1,2) crossover which is 212 MHz red detuned relative to the cooling transition. Hence, a stabilization of the cooling light in a detuning range of up to −212 MHz is possible. Similar to the repumping light, the

[9]TA: M2K Lasers MTK-TA-785 (1 W), diode: Sharp GH0781JA2C (120 mW)

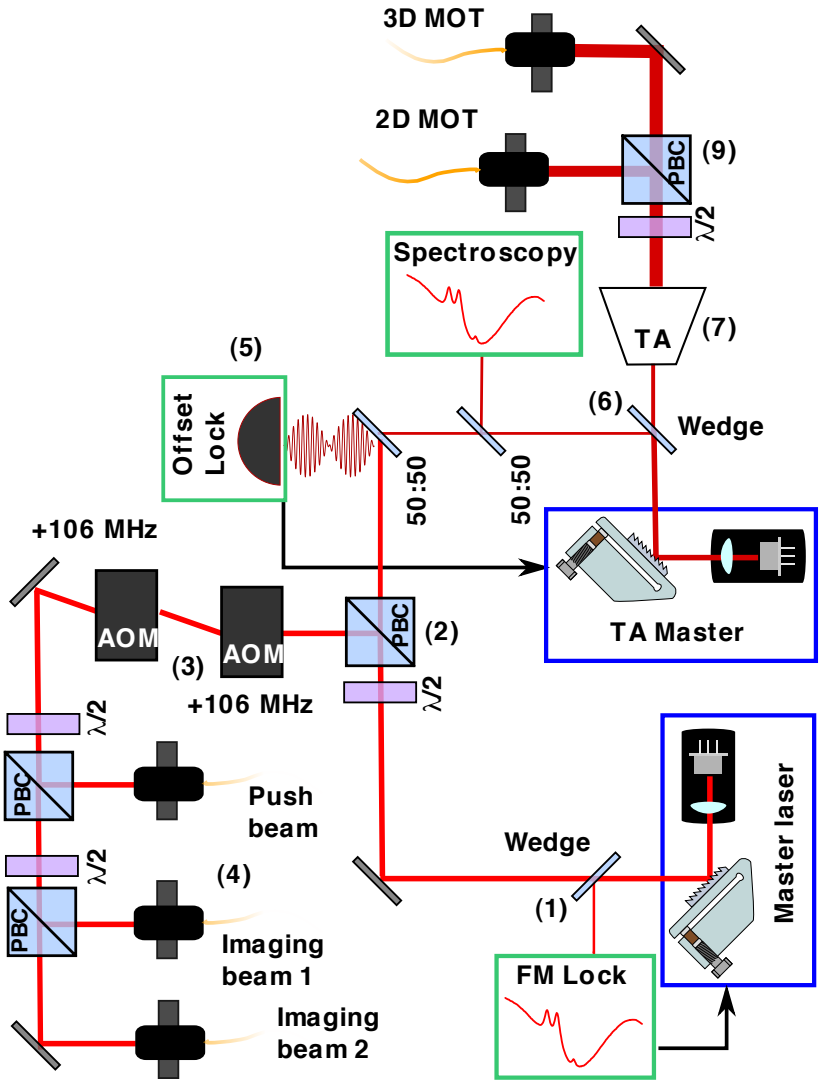

Figure 4.6: Simplified picture of the laser setup for the cooling and imaging beams. A small part of the master laser is coupled out (1) on a glass wedge and used to stabilize the master's frequency. The main part of the beam is asymmetrically split (2) with a half-wave plate and PBC. The larger part is shifted in frequency using two AOMs (3), split in three beams and coupled into optical fibers (4). The smaller part is used to stabilize the TA's seed laser via an offset lock (5). For this stabilization, a small fraction of the seed laser's power is coupled out (6) whereas the main part is amplified in the TA (7), divided into two and coupled into optical fibers (8).

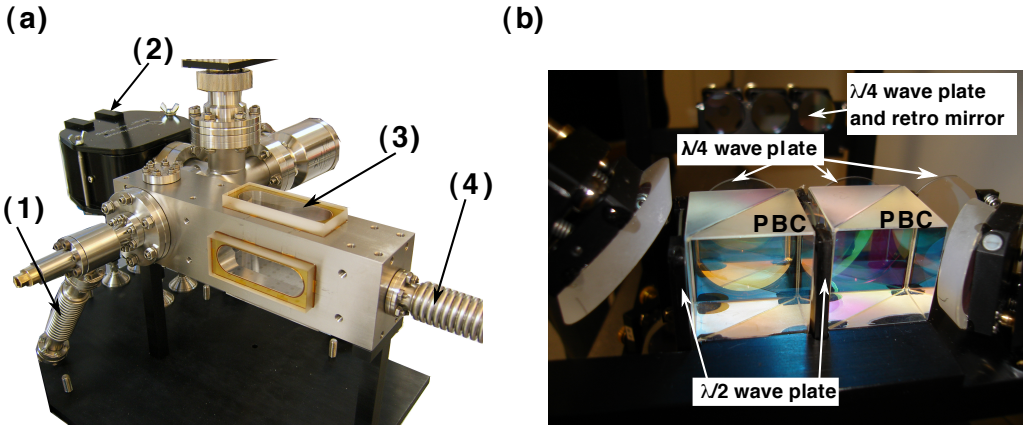

Figure 4.7: (a) Picture of the 2D-MOT. A valve connects the Rb oven (1) to the chamber. An ion getter pump (2) assures a pressure of $\sim 2 \times 10^{-7}$ mbar. The windows (3) are glued to the body to keep the system as small as possible. The 2D-MOT is mounted to the main chamber with a flexible bellow (4). (b) Picture of the horizontal axis of the 2D-MOT. The combined repumper and cooling light enters from the right side. The first half set of wave plate and polarizing beam splitter cube reflect one third of the intensity. The next half wave plate cube section divides the remaining laser power into two. Each beam is individually retro reflected. The correct polarization of each reflected beam is ensured by quarter wave plates.

cooling light is split into two beams and each beam is coupled into a polarization maintaining single mode optical fiber. The power of the 2D-MOT cooling light is 150 mW and the 3D-MOT cooling light power amounts to 100 mW. The remaining light of the master laser is shifted by 212 MHz towards the resonance with two acousto-optical modulators and split into three beams, each of them is coupled into a single mode polarization maintaining optical fiber. One fiber provides 0.7 mW for the push beam for the 2D-MOT whereas the two other provide each an imaging beam for the absorption imaging which will be described later. An overview of the setup can be seen in figure 4.6.

2D-MOT

The setup and the characteristics of the 2D-MOT is described in detail elsewhere [101]. This section will therefore give a brief summary of the 2D-MOT setup.

The 2D-MOT chamber, which can be seen in figure 4.7 is made of titanium and has a rectangular shape. The dimensions of the base body are $(260 \times 70 \times 55)$ mm^3. It has two elongated through bore-holes with a diameter of 25 mm and a length of 81 mm. The pressure in the 2D-MOT chamber is of about 2×10^{-7} mbar.

The cooling and repumping light beams are combined on a polarization beam splitter cube. The combined beam is enlarged by a telescope to a diameter of 25 mm, and then split into two beams, one for the horizontal and one for the vertical axis. The elliptical beam shape, which is needed, due to of the elongated cooling volume, is mimicked by three circular beams close to each other. The three beams are obtained from one beam using two polarization beam splitter cubes and half wave plates (see figure 4.7(b)). The magnetic field gradient of the 2D-MOT is 15 G/cm. In order to increase the flux of the 2D-MOT a near resonant push beam is employed. The 2D-MOT achieves an overall flux of 3×10^8 atoms/s.

3D-MOT

The atom beam provided by the 2D-MOT is captured in the main chamber by a 3D-MOT in standard six-beam configuration [103]. The vertical axis of the vacuum chamber is not accessible for laser beams because of the electron column. The 3D-MOT is therefore oriented in such a way that the direction of the strongest magnetic field gradient lies perpendicular to the optical dipole trap axis in the horizontal plane of the main chamber, while the two other axes are placed on the diagonals, as it can be seen in figure 4.4.

The cooling and repumping light beams are individually enlarged to a diameter of 25 mm and afterwards combined on a polarizing beam splitter cube. The combined beam is then divided into six beams, and overlapped in the center of the main chamber.

The quadrupole field of standard magneto-optical traps is typically generated by two coils in Anti-Helmholtz configuration. However, the electron column uses magnetic lenses, with a pole piece made of a iron-nickel alloy which acts like a μ-metal, causing a deformation of all magnetic fields. We circumvent this problem by using in total six coils which are oriented perpendicular to each other around the chamber. The combined field of all six coils creates a spherical magnetic quadrupole field with the desired geometry and a volume of about 1 cm^3. Within this volume, the magnetic field gradient grows linearly in each direction and resembles the field of a

spherical quadrupole. The field minimum is located 13 mm below the tip of the electron column and the field gradient is 10 G/cm along the strong axis.

4.2.2 Optical Dipole Traps

There are two kinds of traps which are suitable to reach Bose-Einstein condensation: magnetic and optical dipole traps. Magnetic traps use the force on the magnetic dipole moment to trap the atoms in an inhomogeneous magnetic field, while optical dipole traps use the induced electric dipole force which a far detuned laser beam exerts on a neutral atom.

Since an inhomogeneous magnetic field would strongly distort the electron beam, we choose an all-optical approach [110, 111, 112, 113, 18, 114, 115, 116] for the production of the quantum gas. Furthermore, optical dipole traps offer a high efficiency in loading and evaporating atoms and are therefore a favorable alternative to magnetic traps whenever experimental issus complicate the use of magnetic trapping potentials.

Optical Dipole Potential

The optical dipole potential for a neutral atom originates from a light induced electric dipole moment of the atom by the oscillating electric field. Consequently, the induced dipole moment oscillates with the same frequency as the light field. The induced dipole moment is given by [117]

$$\mathbf{d} = \alpha(\omega)\,\mathbf{E} \tag{4.1}$$

where the complex polarizability α is a function of the frequency ω of the driving light field. The energy E_{dip} of the induced dipole in an electric field $\mathbf{E}$ is

$$E_{\mathrm{dip}} = -\mathbf{d}\cdot\mathbf{E} \quad . \tag{4.2}$$

The dipole potential is obtained by time averaging E_{dip}, which gives

$$V_{\mathrm{dip}} = -\frac{1}{2\epsilon_0 c}\mathrm{Re}\left[\alpha(\omega)\right] I \quad . \tag{4.3}$$

Here, the speed of light is denoted by c, and ϵ_0 stands for the the vacuum permittivity. The intensity of the light field I can be written as

$$I = \frac{1}{2}\epsilon_0 c|E|^2 \quad . \tag{4.4}$$

An induced oscillating electric dipole can also emit photons. The scattering rate Γ_{scat} at which it absorbs and re-emits light is provided by the imaginary part of the polarizability,

$$\Gamma_{\text{scat}} = \frac{1}{\hbar\epsilon_0 c}\text{Im}\left[\alpha\left(\omega\right)\right] I \quad , \tag{4.5}$$

where $\hbar$ is the reduced Planck constant.

Considering only one optical transition of frequency ω_0, the polarizability of a two level atom is given by [117]

$$\alpha\left(\omega\right) = \frac{6\pi\epsilon_0 c^3}{\omega_0^2} \cdot \frac{\Gamma}{\omega_0^2 - \omega^2 - i\left(\omega^3/\omega_0^2\right)\Gamma} \quad , \tag{4.6}$$

with Γ being the decay rate of the excited level. The decay rate can be calculated using the dipole matrix element between the ground $|g\rangle$ and excited state $|e\rangle$

$$\Gamma = \frac{\omega_0^3}{3\pi\epsilon_0\hbar c^3}\left|\langle e|\hat{d}|g\rangle\right|^2 \quad , \tag{4.7}$$

where $\hat{d} = -e\mathbf{r}$ denotes the electric dipole operator and e is the elementary charge. Inserting (4.6) in (4.3) and (4.5), one obtains

$$V_{\text{dip}}\left(\mathbf{r}\right) = -\frac{3\pi c^2}{2\omega_0^3}\left(\frac{\Gamma}{\omega_0 - \omega} + \frac{\Gamma}{\omega_0 + \omega}\right) I\left(\mathbf{r}\right) \quad , \tag{4.8}$$

$$\Gamma_{\text{scat}}\left(\mathbf{r}\right) = \frac{3\pi c^2}{2\hbar\omega_0^3}\left(\frac{\omega}{\omega_0}\right)^3\left(\frac{\Gamma}{\omega_0 - \omega} + \frac{\Gamma}{\omega_0 + \omega}\right)^2 I\left(\mathbf{r}\right) \quad . \tag{4.9}$$

In the case of near resonant light, so that the detuning $\Delta = \omega - \omega_0$ fulfills $|\Delta| \ll \omega_0$, one can neglect the counter rotating term with the resonance at $\omega = -\omega_0$. This is commonly know as the rotating wave approximation (RWA). With this simplification the optical dipole potential and the scattering rate reduce to [117]

$$V_{\text{dip}}\left(\mathbf{r}\right) = \frac{3\pi c^2}{2\omega_0^3}\frac{\Gamma}{\Delta} I\left(\mathbf{r}\right) \quad , \tag{4.10}$$

$$\Gamma_{\text{scat}}\left(\mathbf{r}\right) = \frac{3\pi c^2}{2\hbar\omega_0^3}\frac{\Gamma^2}{\Delta^2} I\left(\mathbf{r}\right) \quad . \tag{4.11}$$

A comparison of (4.10) and (4.11) yields

$$\hbar\Gamma_{\text{scat}} = \left(\frac{\Gamma}{\Delta}\right) V_{\text{dip}} \quad . \tag{4.12}$$

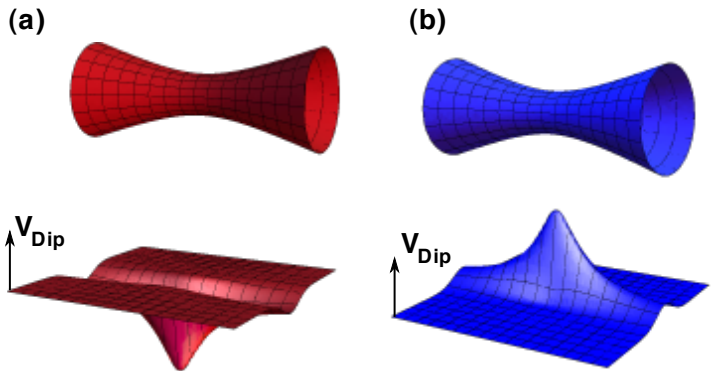

Figure 4.8: Optical dipole potential of a red (a) and blue (b) detuned, focused laser beam with a Gaussian beam profile. Red detuned light forms an attractive potential while blue detuned light creates a repulsive potential.

The dipole potential scales with I/Δ whereas the scattering rate is proportional to I/Δ^2. Hence, it is more favorable to use high intensities at a larger detuning.

If the driving frequency is below the atomic resonance $\omega < \omega_0$, i.e. $\Delta < 0$, the light field is red detuned. In this case the dipole potential is attractive and the atoms are therefore driven towards regions with high light intensity. If the driving frequency is larger than the atomic resonance $\omega > \omega_0$, i.e. $\Delta > 0$, the light field is blue detuned. In this case the dipole interaction repels atoms out of the field. Figure 4.8 illustrates the optical dipole potentials of a focused red and blue detuned Gaussian beam, respectively.

Multi-Zeeman-Level Atoms

Real atoms employed in dipole trapping experiments have electronic transitions with a more complex Zeeman-level sub-structure. The dipole potential will in general depend on the particular sub-state of the atom. To determine the energy shift for a multi-level atom in the ground state $|i\rangle$ the transitions to all excited states $|j\rangle$ have to be taken into account. The energy shift is then given in second order perturbation theory [60] by:

$$\Delta E_i = \sum_{i \neq j} \frac{|\langle j|\hat{d}_{ij}|i\rangle|^2}{E_i - E_j} \,, \tag{4.13}$$

where E_i denotes the unperturbed energy of the ith state. The dipole matrix element $\hat{d}_{ij} = \langle e_j|\hat{d}|g_i\rangle$ for these transition can be determined by the Wigner-

Eckart Theorem [41] which predicts that the dipole matrix element is given by the product of a real transition coefficient or specific line strength c_{ij} and the reduced dipole matrix element $||\hat{d}||$. The resulting dipole potential is obtained by the sum over all excited states [117]

$$V_{\mathrm{dip}}(\mathbf{r}) = \frac{3\pi c^2 \Gamma}{2\omega_0^3} I(\mathbf{r}) \times \sum_j \frac{c_{ij}^2}{\Delta_{ij}} \quad , \tag{4.14}$$

with the spontaneous decay rate Γ corresponding to equation (4.7) and the specific detunings Δ_{ij}.

All experiments presented in this work have been carried out with the ^{87}Rb isotope, which is an alkali atom with a nuclear spin of $I = 3/2$. The fine structure splitting of the D-line doublet $^2S_{1/2} \rightarrow ^2P_{1/2}, ^2P_{3/2}$ with transition frequencies of 795 nm and 780 nm respectively, results from the spin-orbit coupling. The coupling to the nuclear spin causes a hyperfine splitting of the ground state of about 6.8 GHz and splitting of the excited states on the order of hundred MHz. If the laser detuning is large compared to excited state hyperfine splitting, the hyperfine structure cannot be resolved. In this case the following expression for the dipole potential can be derived [117]:

$$V_{\mathrm{dip}}(\mathbf{r}) = \frac{\pi c^2 \Gamma}{2\omega_0^3} \left(\frac{2 + P\, g_F\, m_F}{\Delta_{2,F}} + \frac{1 - P\, g_F\, m_F}{\Delta_{1,F}} \right) I(\mathbf{r}) \quad . \tag{4.15}$$

Here, g_F denotes the Landé factor, m_F stands for the magnetic quantum number, and $P = 0$ for linear and $P = \pm 1$ for $\sigma^{\pm}$ polarized light. The detunings relative to the D_1 and D_2 are represented by $\Delta_{1,F}$ - and $\Delta_{2,F}$ - line. Equation (4.15) can be further simplified if the laser detuning is also large compared to the fine structure and the polarization of the laser light is linear. The dipole potential is then given by the two level result (4.10)

$$V_{\mathrm{dip}}(\mathbf{r}) = \frac{\hbar \Gamma^2}{8\Delta} \frac{I(\mathbf{r})}{I_{\mathrm{sat}}} \tag{4.16}$$

with a detuning relative to the center of the D_1- and D_2-line. The saturation intensity is denoted by

$$I_{\mathrm{sat}} = \frac{\hbar \Gamma \omega_0^3}{12\pi c^2} \quad . \tag{4.17}$$

Quasi-Electrostatic Traps

A typical time scale for evaporative cooling is several seconds to several tens of seconds. To be able to trap cold atoms for such a period in an optical

dipole trap the scattering rates have to be sufficiently small. As the dipole force is proportional to I/Δ whereas the scattering rate is proportional to I/Δ^2 it is favorable to use a far detuned laser and compensate the smaller dipole force with laser power. The simplest way to create an optical dipole trap which is suitable for Bose-Einstein condensation is a focused CO_2 laser beam [111, 113, 118]. The advantage of the CO_2 laser is that it offers high power and, due the wavelength of 10.6 μm, an particularly large detuning.

If the frequency ω of the trapping light is much smaller than the frequency ω_0 of the transition into the first excited state, the trapping light field can be regarded as a quasi static electric field, polarizing the atom [117]. Since the rotating wave approximation is no longer valid in the case of a quasi-electrostatic trap the dipole potential has to be derived from (4.8) by quasi-electrostatic approximation $\omega \ll \omega_0$, yielding

$$V_{\mathrm{dip}}(\mathbf{r}) = -\frac{3\pi c^2}{\omega_0^3}\frac{\Gamma}{\omega_0} I(\mathbf{r}) \quad . \tag{4.18}$$

The scattering rate which is proportional to the dipole potential is given by

$$\hbar\Gamma_{\mathrm{scat}}(\mathbf{r}) = 2\left(\frac{\omega}{\omega_0}\right)^3 \frac{\Gamma}{\omega_0} V_{\mathrm{dip}}(\mathbf{r}) \quad . \tag{4.19}$$

Due to the almost negligible scattering rates the quasi-electrostatic trap represents an ideal realization of a conservative trap.

Experimental Setup of the CO_2 Dipole Trap

In the presented experiment the employed CO_2 laser[10] has a nominal power of 60 W. The intensity of the optical dipole trap is controlled by an AOM[11] while a small fraction of the beam is used to monitor the mode spectrum with a Fabry-Perot interferometer.

The AOM is driven with up to 30 W of radio frequency (rf) power at a frequency between 30 and 50 MHz. The fraction of the rf-power absorbed inside the germanium crystal, leads to unwanted thermal effects. During the evaporative cooling, the laser power has to be reduced by a factor of 200, implying that the rf-power and therefore the dissipated power in the AOM is as well reduced. The smaller the amount of dissipated power the smaller is the heating of the crystal. Since the position of the diffracted

[10] Coherent GEM 50 Select
[11] IntraAction, AGM-406B1

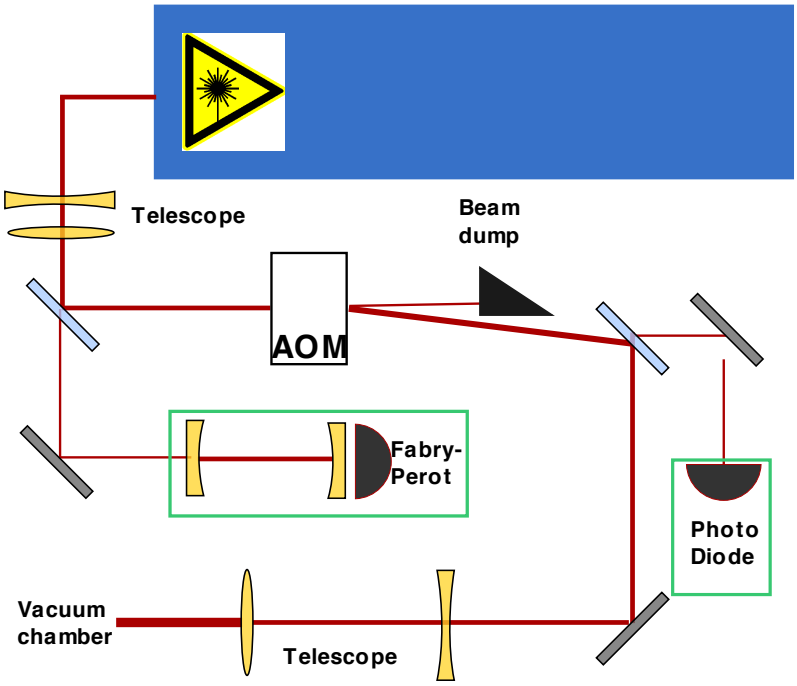

Figure 4.9: Schematic picture of the CO_2 laser setup. The laser provides power up to 60 W and a beam diameter of 4 mm. A telescope enlarges the beam which is then adjusted through an AOM. The beam diameter of the first diffraction order is further increased and provides the light for the optical dipole trap. Small parts of the light beam are used to monitor the power and mode of the laser.

beam also depends on the temperature of the crystal a change of temperature results in a shifted position of the diffracted beam, a phenomenon known as pointing instability. This effect can be reduced by using two radio frequencies (35 MHz and 45 MHz) which are simultaneously applied to the AOM and whose combined power is constant [119, 120]. However, only one frequency (45 MHz) fullfills the Bragg condition for efficient diffraction. Thus, the ratio of the power between these two frequencies determines the laser intensity in the dipole trap. The achieved pointing stability is better than 2 mm at a distance of 2 m behind the AOM.

The non diffracted beam is dumped after the AOM and the main part of the beam is then enlarged by a second telescope and adjusted through the vacuum chamber. Again, a small fraction of the beam is coupled out

and used to monitor and stabilize the power of the diffracted beam. The setup of the CO_2 laser is shown in figure 4.9.

The laser beam is focused with an aspheric lens to a diffraction-limited beam waist of 30 μm. The lens has a focal length of 63 mm and is mounted inside the vacuum chamber as described in section 4.1. The focus of the CO_2 laser overlaps with the center of the MOT. An identical lens is used to collimate the beam again before exiting the main chamber.

4.2.3 Experimental Cycle

We will give a brief overview of the experimental cycle. This implies the timing system, the loading of the optical dipole trap, and the conventional absorption imaging system.

Timing System

To execute all necessary tasks for Bose-Einstein condensation a timing system is needed. This section gives a brief review of our timing system, a detailed description can be found in [121].

A precise control of the setup is crucial to the success of the experiment. It is realized by a real-time computer system[12] featuring 8 analog and 32 digital output channels. Each channel can be individually set each microsecond with a jitter of < 20 ns. The scripting language Python[13] running in an interpreter realizes the definition of the experimental sequence and the configuration of the real-time device. The same program transfers the sequence to the real-time hardware over an Ethernet connection on which it is autonomously executed.

Loading the Dipole Trap

Each experimental cycle starts with the loading of the MOT. This is accomplished by switching on the 2D-MOT which includes the cooling and repumping light, the push beam and four magnetic coils. The cooling light beam has a power of 150 mW and is controlled by a mechanical shutter. The resonant push beam and the light of the repumping transition $|5sS_{1/2}(F = 1)\rangle \rightarrow |5sP_{3/2}(F' = 2)\rangle$ are enabled by acousto-optical modulators and mechanical shutters, respectively. The power of the repuming

[12] Jäger Messtechnik AD-win Pro II

[13] www.python.org

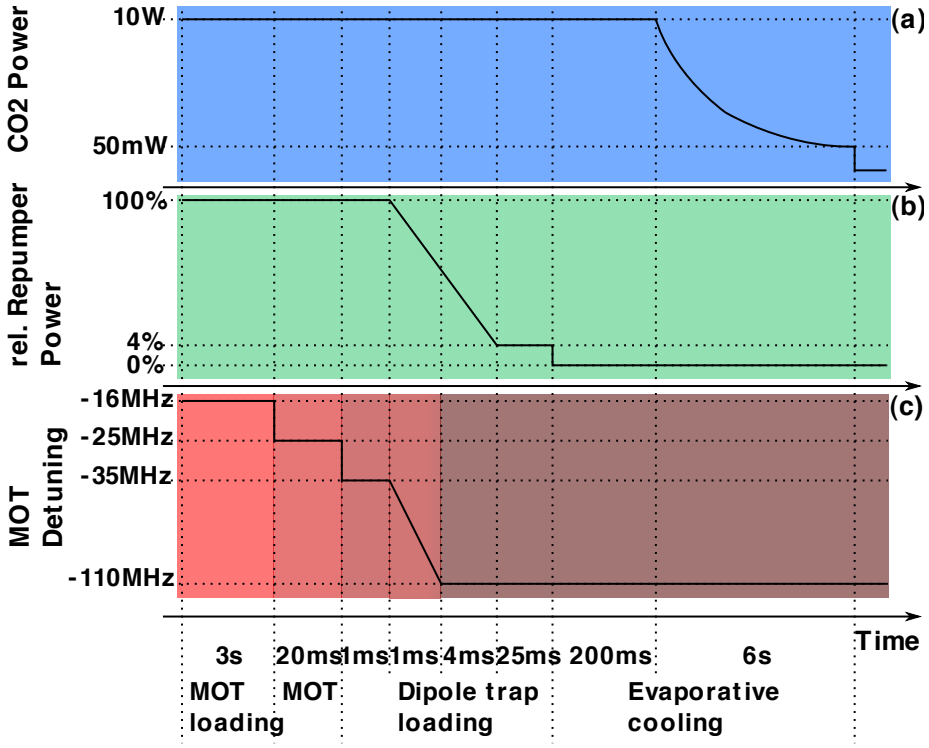

Figure 4.10: Schematic illustration of the loading process of the optical dipole trap. The vertical lines highlight special time steps on the time line (abscissa) during the experimental cycle. Note, that the time intervals are not true to scale. The upper graph depicts the progression of the CO_2-power. The power is kept constant until the beginning of the evaporation. The middle graph illustrates the characteristics of the repumper power. The lower graph constitutes the different detuning steps during the dipole trap loading.

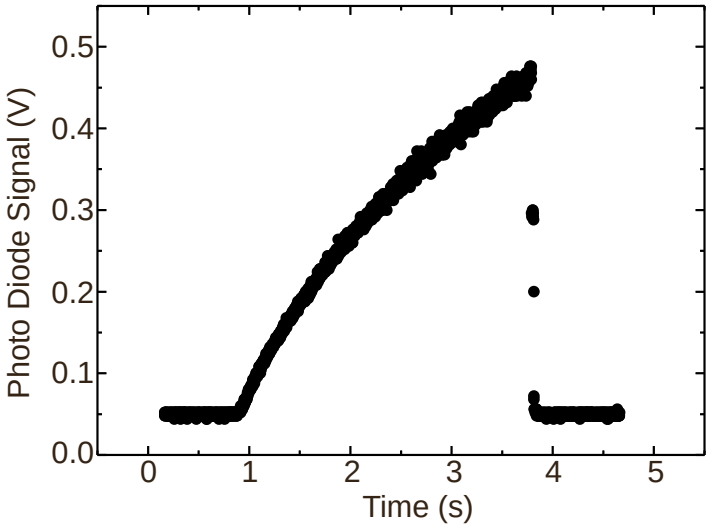

Figure 4.11: Loading of the MOT. The fluorescence signal is monitored with a photo diode. The fluorescence signal of 450 mV corresponds to 1×10^9 trapped atoms in the 3D-MOT. The atoms are then transfered into the optical dipole trap and the MOT-beams are switched off, indicated by the sudden drop of the fluorescence signal.

light in the 2D-MOT is 7 mW and the push beam uses 0.7 mW. Figure 4.10 shows a schematic overview of the timing of the loading process.

Synchronized to the 2D-MOT, the light and the magnetic coils of the 3D-MOT are engaged. The power of the cooling light in the 3D-MOT is 100mW and the repumper has 6 mW. Since the cooling light for the 2D- and 3D-MOT are obtained from one laser and no additional AOM is employed, both magneto-optical traps have to use the same detuning of -16 MHz. After a loading time of 3 s the 3D-MOT contains about 1×10^9 atoms. The fluorescence signal of the 3D-MOT can be seen in figure 4.11.

The CO_2 laser is activated and set to 10 W at the beginning of every cycle, as depicted in figure 4.10 (a). The optical dipole trap at this time has trapping frequencies of $\omega_{\mathrm{ax}} = 2\pi \times 180$ Hz in the axial and $\omega_{\mathrm{rad}} = 2\pi \times 2860$ Hz in the radial direction of the dipole trap.

After the loading time of three seconds all the laser beams and the magnetic fields of the 2D-MOT are switched off. In order to further cool and

compress the atoms in the 3D-MOT, a stepwise increase of the MOT-beam detuning is initialized with the end of the loading phase. Starting with -25 MHz for 20 ms, a sequence of -35 MHz for 1 ms is followed by a linear ramp down to -110 MHz with in 1 ms. The different steps of the detuning are depicted in figure 4.10 (c).

The power of the repumping light is linearly reduced to 4% of its original value simultaneously to the beginning of the detuning ramp to create a temporal dark-MOT [122]. Unlike the detuning, the repumping power is changed over 5 ms. The cooling light with the final detuning of -110 MHz and the reduced repumping power is kept for another 25 ms after which all MOT-lights are switched off. The evolution of the repumping light power can be seen in figure 4.10 (b). Due to the weak repumping light, the atoms are pumped into the $|5S_{1/2}(F = 1)\rangle$ ground state. The magnetic field of the 3D-MOT is switched off, after the atoms are transfered into the optical dipole trap. The atoms are then further cooled towards quantum degeneracy by evaporative cooling which is described in the following section 4.2.4.

Conventional Imaging System

Although the focus of this work is high resolution imaging with the aid of a focused electron beam, the experiment is equipped with two CCD cameras[14] that allow for conventional absorption imaging [76] of the atom cloud from two directions.

4.2.4 All-Optical BEC

The last cooling step on the way to a Bose-Einstein condensate is evaporative cooling [123, 124, 125], which is achieved in an optical dipole trap by lowering the intensity of the trapping light.

The starting power of 10 W corresponds to a trap depth of 530 μK. With the described loading sequence we load 4×10^6 atoms with a temperature of 170 μK into the dipole trap. Since an optical dipole trap is not sensitive to magnetic substates, all magnetic substates of the $F = 1$ manifold are trapped, which results in a spinor condensate. The phase space density at this point is $n\lambda_{\mathrm{dB}}^3 = 5 \times 10^{-5}$. The dipole trap depth is held constant for 200 ms to allow for plain evaporation, during which the temperature of the ensemble is reduced to 70 μK, whereas the phase space density is

[14] Apogee Alta U1

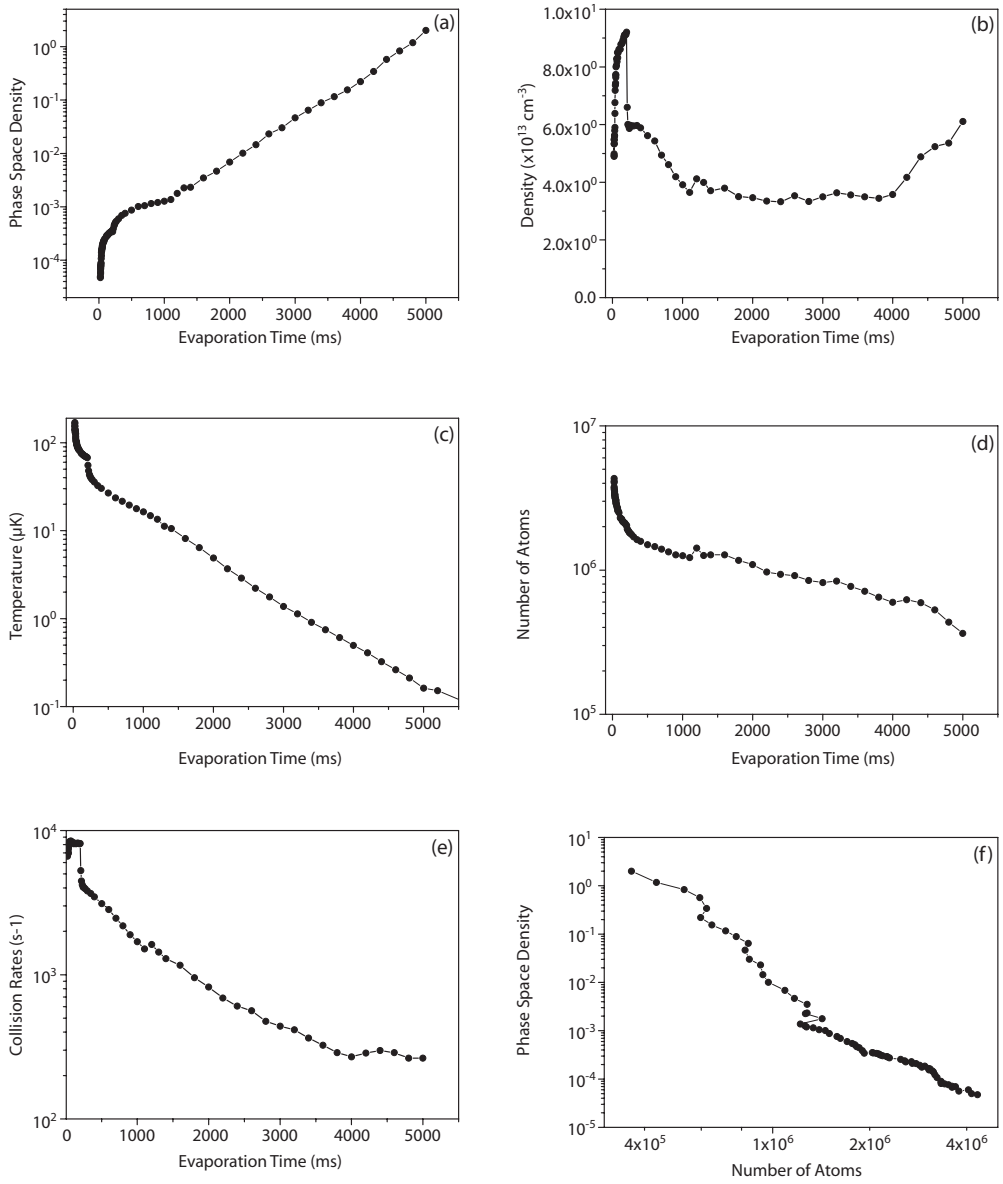

Figure 4.12: (a) Time evolution of the phase space density during the evaporation. (b) displays the evolution of the density of the cloud. The decrease in temperature is shown in (c). Due to the lowering of the optical dipole trap's intensity the number of atoms decreases during the evaporation (d) and the collision rate drops by almost two orders of magnitude as depicted in (e). (f) shows the phase space density as a function of the atom number. As the number of atoms decreases the phase space density is increased.

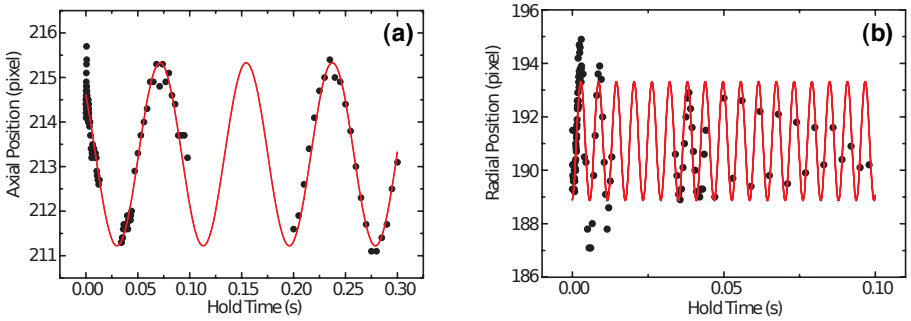

Figure 4.13: (a) Measurement of the axial trap frequency of the optical dipole trap. The obtained trap frequency is $\omega_{\mathrm{ax}} = 2\pi \times 12\,\mathrm{Hz}$. (b) shows the measurement of the radial trap frequency which is found to be $\omega_{\mathrm{rad}} = 2\pi \times 170\,\mathrm{Hz}$.

increased to $n\lambda_{\mathrm{dB}}^3 = 3.5 \times 10^{-4}$. The evolution of phase space density, the temperature, the collision rate, the atom number, and the density during the evaporation are shown in figure 4.12.

Further evaporation is achieved by lowering the intensity of the optical dipole trap. The best result is found for a sum of two exponential ramps with a time constant of 10 ms and an amplitude of 4 W for the fast decay. The slow decay has a time constant of 950 ms and an amplitude of 6 W. The evaporation ramp is indicated in figure 4.10 (a). The critical temperature for Bose-Einstein condensation is reached at 160 nK with typically 3×10^5 atoms. An almost pure condensate with about 1×10^5 atoms is obtained for a final laser intensity of 50 mW, with corresponding trapping frequencies of $\omega_{\mathrm{ax}} = 2\pi \times 12\,\mathrm{Hz}$ and $\omega_{\mathrm{rad}} = 2\pi \times 170\,\mathrm{Hz}$.

An atomic cloud trapped in a parabolic trap that is pulled away from its equilibrium position, will start to oscillate in the trap without damping [126, 127, 128]. The oscillation frequency corresponds to the trapping frequency and can be obtained by measuring the condensates position for different holding times in the trap. The outcome of such a measurement for a CO_2 laser intensity of 50 mW is shown in figure 4.13.

If the expansion time is long enough the recorded density distribution corresponds to the momentum distribution of the initial spacial distribution in the trap. A BEC in the Tomas-Fermi limit expands anisotropically whereas

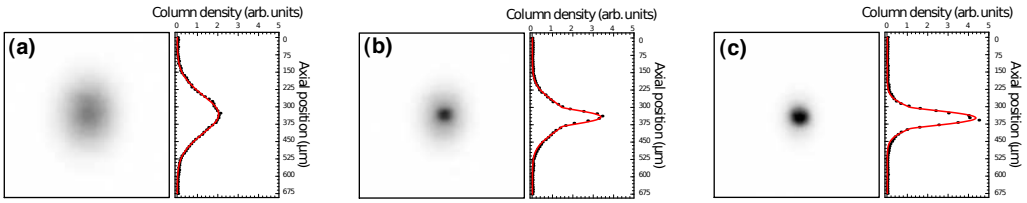

Figure 4.14: Absorption images of the atomic cloud after 15ms time of flight for different temperatures. (a) Thermal cloud ($T = 260$nK, $N_{\mathrm{th}} = 3.8{\times}10^5$). (b) Bimodal distribution ($T = 90$ nK, $N_0 = 6 \times 10^4$, $N_{\mathrm{th}} = 2.1 \times 10^5$). (c) BEC ($N_0 = 1.2 \times 10^5$). The graphs on the right-hand side show a cut through the cloud center along the axial direction together with the corresponding fit.

a thermal cloud shows an isotropic distribution. The recorded combined density profile can be fitted with a bimodal distribution consisting of a parabola for the condensed fraction and a Gaussian distribution for the thermal atoms. From the modeled function the condensate fraction, number of atoms and temperature can be extracted. Figure 4.14 shows typical absorption images of atom clouds released from the trap at different temperatures.

Chapter 5

Electron Microscopy of an Ultracold Quantum Gas

In this chapter we will concentrate on imaging an ultracold atom cloud with the aid of the electron microscope, starting with the introduction of the employed electron microscope, followed by the description of the ion optic and detector system. After the necessary hardware has been introduced, we will present the new imaging technique for ultracold quantum gases, beginning with the working principle, and the experimental sequence. The proof of principle is given by imaging the density distribution of a trapped Bose-Einstein condensate. The obtained density profiles are compared to the theoretical description and possible perturbation and heating effects are discussed. This chapter ends with an estimation of the detection efficiency of the imaging technique.

5.1 Electron Column

In order to build an electron microscope that is able to image ultracold atoms, the electron column has to fulfill several requirements. The characteristic interaction length, which was introduced in section 2.1.5, typically is on the order of half a micrometer or even smaller. Therefore the electron column should provide an electron beam that can be focused to a diameter of a few hundred nanometers and below. Furthermore, the current of the electron beam should be as high as possible since the probability for a scattering event between the electron beam and the atomic sample is proportional to it. And finally, the electron column has to be UHV compatible, because the tip of the electron microscope and the quantum gas have

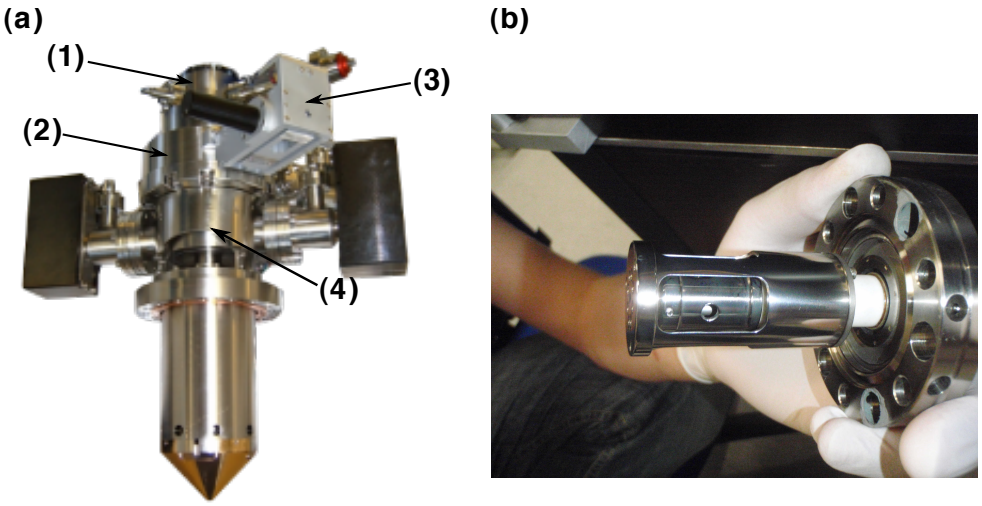

Figure 5.1: (a) shows a picture of the electron column. The column consists of three different vacuum chambers: the gun chamber (1) which holds the electron emitter, the aperture chamber (2) in which a movable stage (3) with several apertures is mounted, and the so called intermediated (4) chamber which mainly consists of a pneumatic isolation valve. (b) shows a picture of the electron emitter.

to share the same vacuum chamber. On the basis of this set of requirements we chose a custom made electron column[1].

The columns electron source is a thermal ZrO-Schottky emitter, which provides an electron beam with an energy up to 6keV. A picture of the column and the electron emitter is shown in figure 5.1. ZrO-Schottky emitters are virtual source point cathodes [83, 129]. In contrast to conventional crossover mode cathodes, whose electron optical system uses the crossover as the object, the virtual source cathodes system uses a virtual crossover which is located behind the physical cathode, see figure 5.2. The column consists of three different vacuum chambers: the gun chamber which holds the electron emitter, the aperture chamber in which a movable stage with several apertures is mounted, and the so called intermediated chamber which mainly consists of a pneumatic isolation valve. Each vacuum chamber of the electron column is equipped with individual ion getter pumps. Since electron emitters have a limited life time, typically 12,000 hours for a ZrO-Schottky

[1]Delong Instruments, http://www.dicomps.com

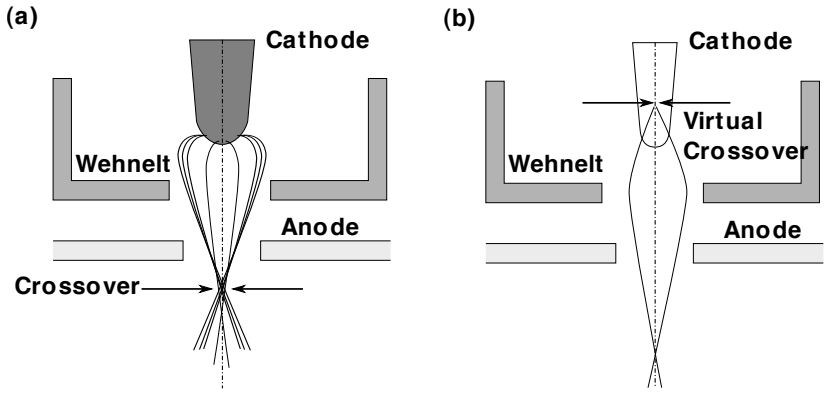

Figure 5.2: (a) conventional crossover cathode. The electron trajectories form a real crossover behind the anode. (b) virtual crossover cathode. The electron trajectories are bent in such a way that they appear to have emerged from a virtual source located behind the physical cathode.

emitter, it is important that the gun chamber can be vented and the emitter exchanged without effecting the main chamber of the experimental setup. Figure 5.3 shows an overview of the internal setup of the electron column.

The electron column has two magnetic lenses [83] to focus the beam at a working distance of 13 mm below the tip of the electron column. The distance between the two lenses is 35 cm. The magnetic field produced inside the second lens amounts to 2000 G which is guided in the μ-metal pole piece of the electron column tip. Due to the self-shielding of the pole piece, the magnetic field at the atoms position is reduced to 1 G. Hence, any influence of the magnetic lens on the atoms can be neglected.

The geometry of the magnetic lenses is to such an extend, that the virtual electron source is magnified by a factor of four at the position of the atoms. For an assumed virtual electron source size of 20 nm FWHM[2] one would obtain an electron beam with a FWHM of 80 nm. The size of the actual probe is substantially larger due to spherical aberration errors. These errors can be reduced by inserting apertures into the electron beam. Thereby are the radial extension of the beam and the spherical aberration decreased. On the other hand it reduces the beam current. For every application a suitable set of resolution and beam current has to be found. The trade-off between resolution and beam current is a common feature of charged

[2] **F**ull **w**idth at **h**alf **m**aximum

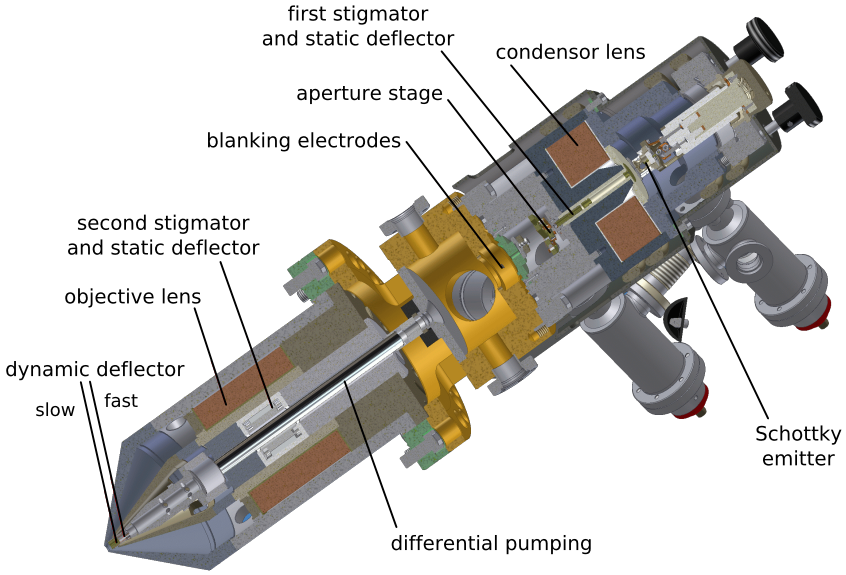

Figure 5.3: Technical drawing of the column. The electron beam is generated by a thermal ZrO-Schottky emitter. A magnetic lens collimates the beam which is shaped by electrostatic deflector and stigmator units. A variable aperture can be used to control the beam current and width. The blanking unit can dump the beam inside the column. A second pair of deflectors and stigmators is used to correct the beam shape before the second magnetic lens focuses the beam onto the specimen. The beam can be scanned via two scanning units, a fast and a slow one.

particle optics. Some typical working points are listed in table 5.1. The apertures can only correct for spherical aberrations. Astigmatic aberrations and displacement of the electron beam, caused by the lenses, have to be eliminated by additional units. The latter is overcome by electrostatic deflectors and astigmatic aberrations are corrected by stigmators [129]. The deflectors and stigmators are placed in a combined unit behind each lens.

The movable aperture strip with apertures of 300 μm, 250 μm, 150 μm, 100 μm, 50 μm, and 20 μm is placed underneath the first deflector and stigmator stage in the aperture chamber together, with an electrostatic blanking unit which allows for the dumping of the electron beam inside the column with a frequency up to 5 MHz. Two physically separated scanning units, consisting of electrostatic quadrupoles, can move the electron beam

FWHM	Current	Aperture	Energy
90 nm	12 nA	50 μm	6 keV
250 nm	100 nA	100 μm	6 keV
5 μm	800 nA	no aperture	6 keV
400 nm	18 nA	50 μm	3 keV

Table 5.1: Typical working points of the electron column. The aperture defines the radial extension of the electron beam inside the column, and therefore influences the beam current and the contribution of the spot size stemming from spherical aberrations. The performance of the electron microscope worsens for decreasing beam energy.

over the atom cloud. The fast scan unit has a field of view of $200\mu\text{m} \times 200\mu\text{m}$ and can be moved with a bandwidth of 10 MHz. The slow scan unit offers scans with 20 kHz and a field of view of 1 mm $\times$ 1 mm.

The alignment and characterization of the electron beam prior to a measurement is done with a so called test target, which is usually a periodically structured copper substrate, for instance a copper mesh. We have mounted

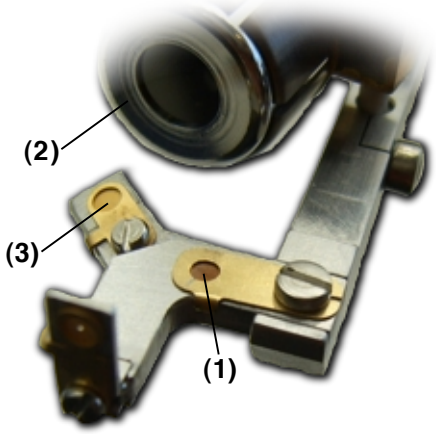

Figure 5.4: Picture of the test target holder. The copper mesh test target (1) is used to align the beam. The MCP (2) serves as the detector for scattered electrons which are used to compile the image in the normal electron microscope mode. The result of the alignment can be observed by scanning the beam over the edge of the hole (3). By fitting an error function to the obtained line scan one can determine the electron beam diameter.

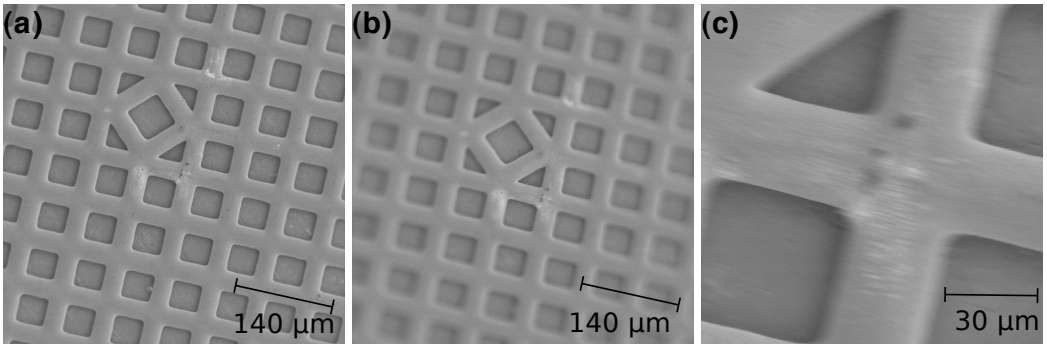

Figure 5.5: Electron beam adjustment with the mesh test target. (a) shows the test target after alignment. (b) shows a low quality field of view caused by misalign deflector elements. (c) shows an image that is blurred horizontally due to astigmatism.

two separate test targets on a movable test target holder, which was introduced in section 4.1, and can be seen in detail in figure 5.4. The first test target is a copper mesh, and the second is a hole with a diameter of 200 μm. Furthermore, a MCP[3] is placed on the holder, that detects secondary and backscattered electrons from the test targets.

The electron column offers two operation modes. In the first mode, all parameters, from beam energy to excitation of the magnetic lenses of the electron column and the scanning units, are computer controlled. The image is composed from secondary and backscattered electrons from the test targets detected by the MCP on the test target holder. This mode is used to align and characterize the electron beam. In the second operation mode, the scan units and the blanker are controlled by applying a voltage to an external input. This mode is employed for imaging ultracold quantum gases.

5.1.1 Alignment and Characterization of the Electron Beam

The alignment starts by setting the desired beam energy and inserting the cooper mesh test target into the electron beam. The upper lens focuses the beam on the specimen while the second lens, deflectors and stigmators are switched off. The deflectors are aligned to achieve the best field of view. This means that the image should be evenly sharp over the largest possible

[3] **M**ulti **C**hannel **P**late

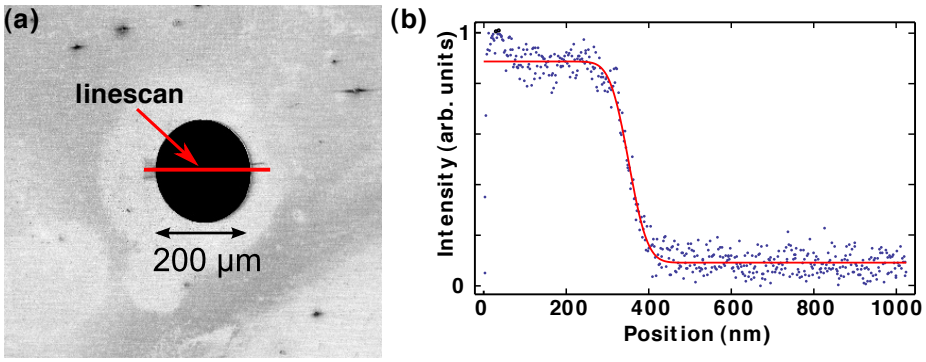

Figure 5.6: (a) shows an image of the hole taken with the scanning electron microscope. The axis of the line scan is indicated by the red line. (b) shows the result of the line scan with an error function fit.

area, as indicated in figure 5.5. After aligning the deflectors the stigmators are optimized for smallest possible distortion of the image.

For the next alignment step the current in the first magnetic lens is slightly decreased whereas the current in the second lens is increased. The result of the decreased excitation in the first lens is a parallel electron beam between the two lenses. The beam is now focused by the second magnetic lens on the specimen. The alignment procedure is repeated with the second pair of deflectors which are again optimized on best field of view like the first pair. To minimize the spherical aberrations an aperture is inserted in such a way that the image experiences minimal distortion. After inserting the aperture the fine adjustment is done by optimizing the second stigmator and the fine focus of the second lens.

To determine the beam diameter, the test target has to be changed from the mesh test target to the hole test target. Since the hole test target and the mesh test target have slightly different vertical positions, the fine focusing with the second lens and stigmator has to be repeated on the hole target. The beam diameter is obtained by taking a line scan over the edge of the hole and fitting the measured line scan with an error function from which the beam diameter is determined.

Apart from the higher resolution, electron imaging systems have another advantage over optical imaging methods: the depth of focus of an electron imaging system is larger compared to an optical imaging system. In

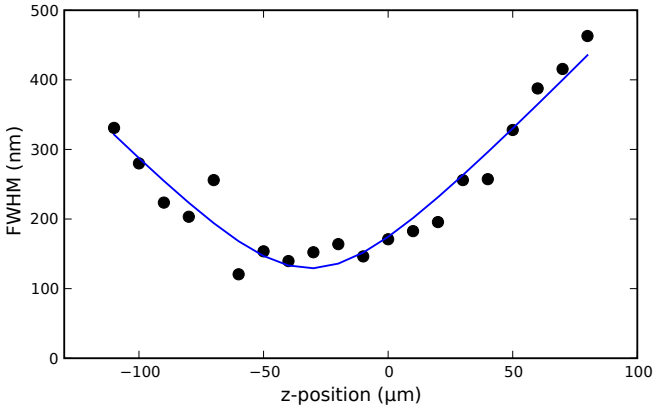

Figure 5.7: Depth of focus measurement of the electron beam. The FWHM diameter of the electron beam is determined with the test target at different positions along the propagation axis of the beam. The settings of the electron optics were left unchanged during the measurement.

our apparatus the depth of focus is obtained by measuring the FWHM of the electron beam at several vertical positions without refocusing. This is achieved by moving the hole target in different positions along the beam axis. Figure 5.7 shows the result for an electron beam with a FWHM of 120 nm. At larger distances from the focus the diameter of the beam starts to increase linearly. In the language of Gaussian beam optics this would correspond to a Rayleigh length of 35 μm and a beam waist of 130 nm [130]. For a vertical extension of the atom cloud, of 6 μm, the electron beam diameter can therefore be assumed as constant.

5.2 Ion Optics and Ion Detector

The ions are produced in the middle of the chamber from where they have to be extracted and guided towards an ion detector. A schematic overview and a picture of the employed ion optics can be seen in figure 5.8. The ion detector is a channeltron[4], which is a tube-shaped continuous dynode electron multiplier. The extracted ions are not detected by the channeltron directly. They are attracted by the high negative voltage of -4.8 kV of the conversion dynode instead. The ions produce secondary electrons which are then accelerated towards the channeltron. The input of the channeltron has a voltage of -2.2 kV and is grounded at the end. The conversion efficiency

[4]DeTech, Model 402A-H

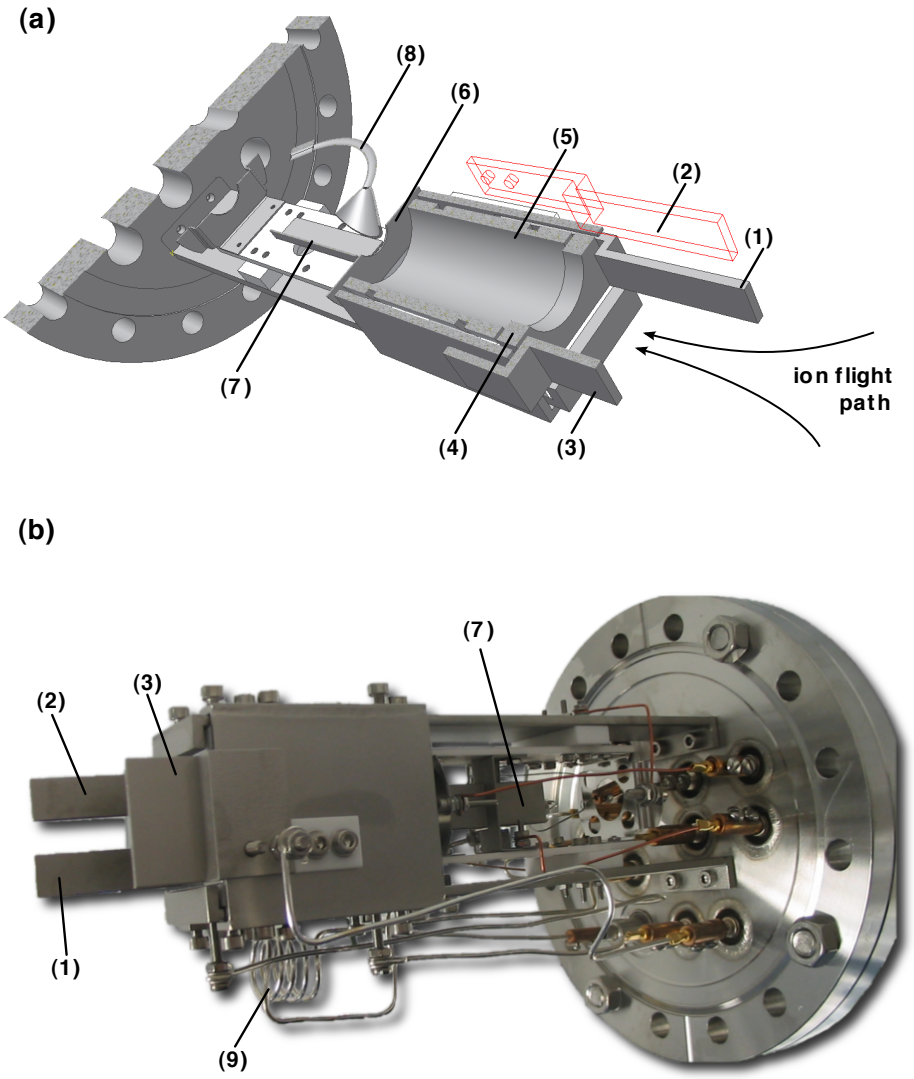

Figure 5.8: (a) Sliced model of the ion optics setup. The ions are guided into the detection unit by the lower left electrode (1), the upper left electrode (2) and the right electrode (3). The forward ring electrode (4), the cylinder electrode (5) and the rear ring electrode (6) direct the ions towards the conversion dynode (7) and the channeltron detector (8). (b) Picture of the assembled unit. The whole setup is mounted on a CF100 flange. A radio frequency (9) and a microwave antenna, which cannot be seen on this picture, are placed as well on the flange.

of the conversion dynode is almost 100% [131]. A detected ion causes a negative voltage peak at the anode of the channeltron of 10 to 60 mV.

The output signal is converted into a TTL[5] pulse by a discriminator. Each single ion is represented by a single pulse. A multi channel scaler card[6] (MCS) records each event. The card has 65536 channels with a variable bin length. Every channel records the events in a certain time window resulting in a time-resolved ion signal. A computer configures the card and saves the obtained signal.

5.2.1 Time of Flight Spectrum

The detector cannot distinguish between singly charged ions and multiply charged ions. Due to the different charge-to-mass-ratio, singly and multiply charged ions have different travel times until they reach the ion detector. The fraction of the differently charged ions can be obtained by taking a time of flight spectrum.

For measuring the time of flight spectrum a BEC is prepared in the optical dipole trap underneath the electron microscope. The atoms are illuminated with the electron beam 1000 times for an interval of 100 ns. The electron beam is not moved, it is held constant on the center of the atom cloud. The MCS card is started simultaneously with the illumination. The complete cycle is repeated several times to improve the statistic. The result is shown in figure 5.9. About 80% of the ions are singly charged, but one also finds higher charged ions up to Rb^{6+}. Every peak in the time of flight spectrum represents an ionization state. The singly charged ions need 18 μs to reach the detector. It should be noted that the height of the peaks gives only an estimate of the production rate of the different states, because the detection efficiency of the different states may vary due to different kinetic energies.

5.3 Imaging a Bose-Einstein-Condensate

In the preceding section the electron column, the ion optics, and the ion detector were introduced and characterized. The following section will present the new imaging technique which allows for high resolution imaging of a trapped Bose-Einstein condensate. We start with the description of the

[5] **T**ransistor-**T**ransistor **L**ogic
[6] Ortec MCS-PCI, http://www.ortec.com

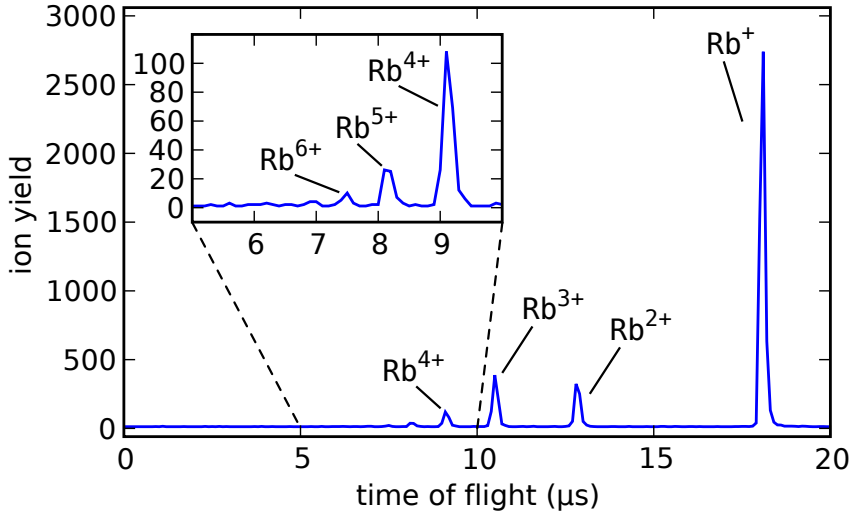

Figure 5.9: Time of flight spectrum of ^{87}Rb atoms ionized by electron impact ionization. The peaks in this spectrum correspond to multiply charged ions up to Rb^{6+} [132]. The singly charged ions amount to about 80% of all events.

working principle and the experimental sequence, before showing first result of the new imaging method.

5.3.1 Working Principle

The imaging technique uses a focused electron beam which is scanned over the trapped atom cloud. A fraction of the atoms is ionized and those produced ions are extracted and subsequently detected with the aid of ion optics and an ion detector. The knowledge of the scan pattern and the obtained ion signal allows us to reconstruct the image of the atom cloud. An illustration of the working principle is depicted in figure 5.10.

Scan Pattern

In order to move the electron beam in any arbitrary scan pattern, one has to use the second control mode of the electron column. The voltages for the scanning unit are generated using waveform generators or the analog channels of the experiment control (see chapter 4.2.3). The blanker is controlled by a digital channel.

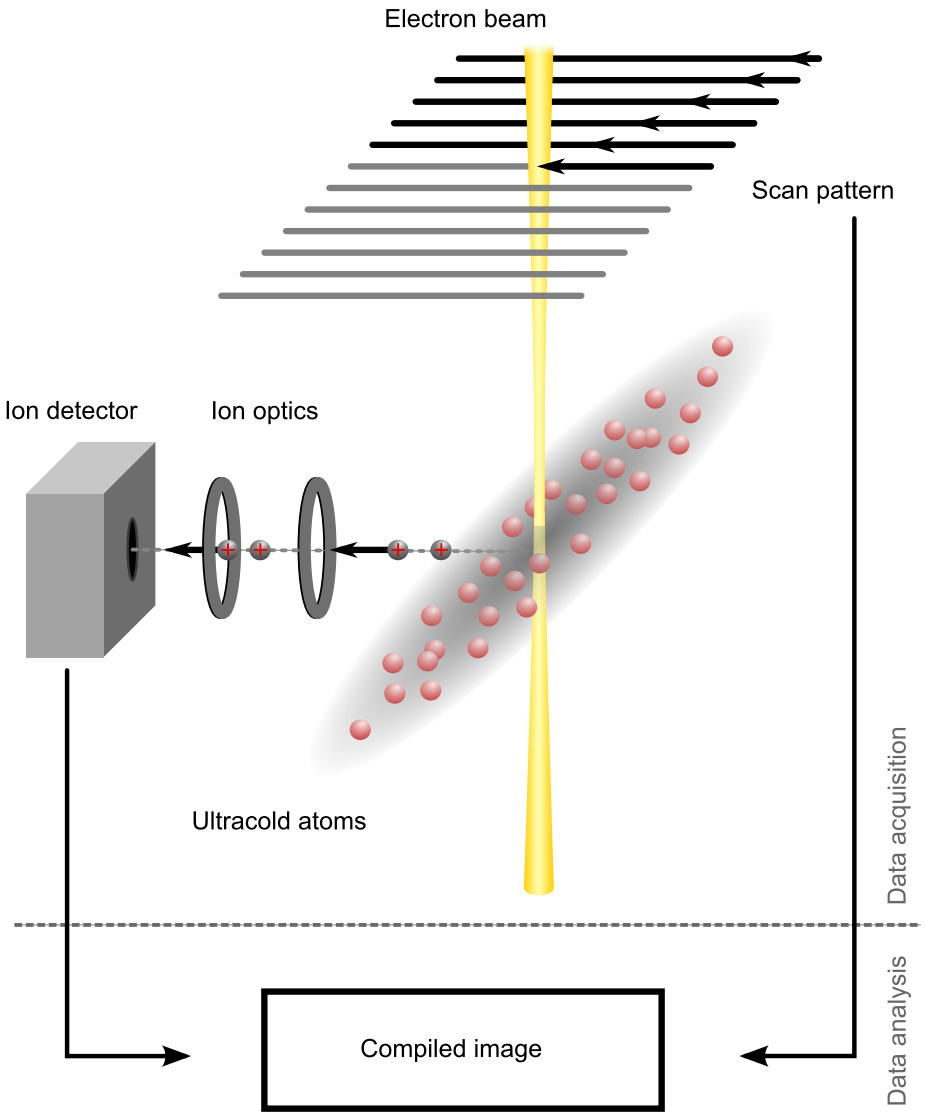

Figure 5.10: Illustration of the working principle. A focused electron beam is moved over the ultracold atom cloud along a scan pattern. Atoms which are hit by an electron are ionized with a certain probability. These ions are extracted using ion optics and subsequently detected by an ion detector. From the obtained time resolved ion signal and the knowledge of the scan pattern one can compile an image of the scanned atom cloud.

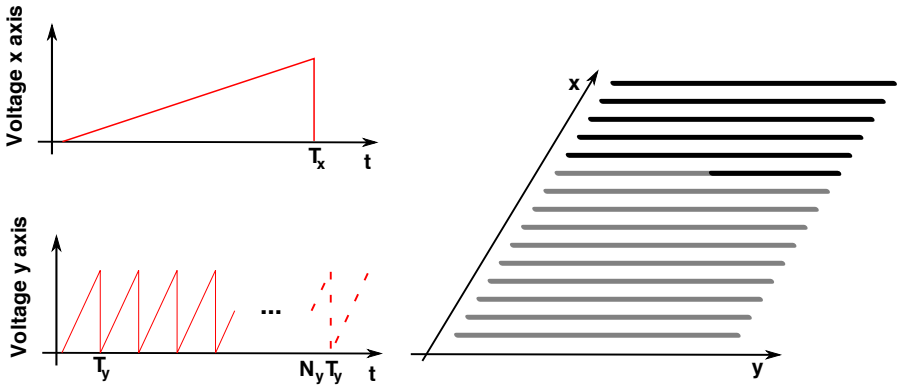

Figure 5.11: Illustration of the scan patterns generation.

The employed scan pattern is comparable to that in television picture tubes and it is generated by two waveform generators: one for each imaging axis. The first generator provides the deflection along the x-axis using a saw tooth voltage form. The second generator sets the deflection along the y-axis and uses a repetition of several identical saw tooth voltage waveforms. The scan pattern is depicted in figure 5.11. The electron beam is therefore continuously moved and not in discrete steps. The length of the individual scan patterns depends on the number of pixels N_x, N_y in the image, and the dwell time Δt on each pixel. The image duration is then

$$T = N_x \times N_y \times \Delta T \quad , \tag{5.1}$$

while the length of the scan pattern in y direction is $T_y = N_y \Delta t$, and $T_x = N_x N_y \Delta t$ in x direction, respectively. The voltage amplitudes are defined prior to the imaging process from the conversion factors

$$f_x = f_y = \frac{1}{55.43} \frac{V}{\mu m} \quad , \tag{5.2}$$

and transfered to the waveform generators via Ethernet. The conversion factors are first estimated from electron microscopy images of the test targets and later refined by imaging atoms in an optical lattices, comparing the result to the theoretical value, see chapter 6.

The lower limit for the dwell time is given by the smallest time bin of the MCS card which is 100 ns. The ion signal intensity is, in case of small depletion, proportional to the dwell time.

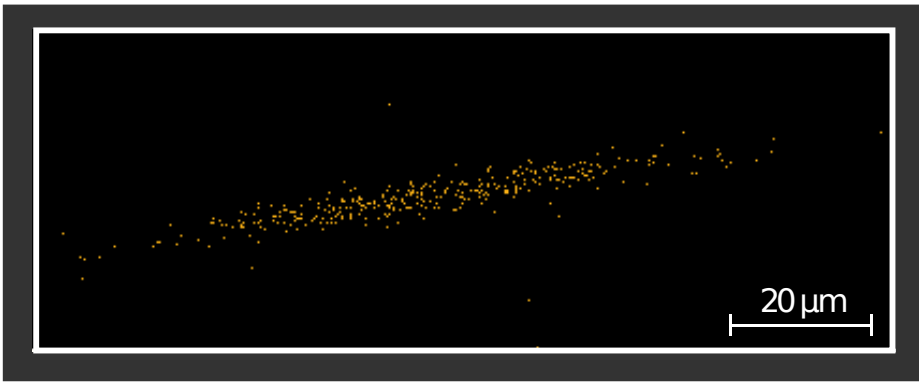

Figure 5.12: Scanning electron microscope image of a BEC. It shows a single shot image of the whole atom cloud with about 350 ions. The image consists of 150 × 400 pixels with a pixel size of 300 nm × 300 nm. The dwell time of is 2 μs, resulting in an overall image time of 120 ms. The electron beam has a FWHM of 140 nm and a current of 20 nA.

5.3.2 Experimental Sequence

The maximum field of view of the slow scan unit is 1 mm × 1 mm. Since the distortion of the electron beam is the smallest for zero deflection, the BEC has to be prepared as close as possible to the center of the scan field. This is achieved by scanning the electron beam symmetrically over the middle of the scan field. If the atom cloud is not properly aligned within of the scan field, the position of the optical dipole trap is adjusted so that the center of the atom cloud and the scan field coincide. The position of the optical dipole trap is moved by slightly changing the direction of the laser beam.

After aligning the BEC underneath the tip of the electron column the signal processing setup is changed and the ion detector signal is given to the MCS. A single experimental run consists of making a BEC, scanning the atom cloud with the focused electron beam, and recording ion signal. After the electron exposure the cloud is released from the trap and a standard absorption image of the remaining atoms is taken to analyze the momentum distribution. The BEC has the form of a cigar, thus a rectangular scan pattern with 150 × 400 pixels is chosen. The size of each pixel is 300 nm × 300 nm and the dwell time is 2 μs, resulting in an image time of 120 ms. An image obtained in a single experimental run (single shot) is shown in figure 5.12, consisting of about 350 ions.

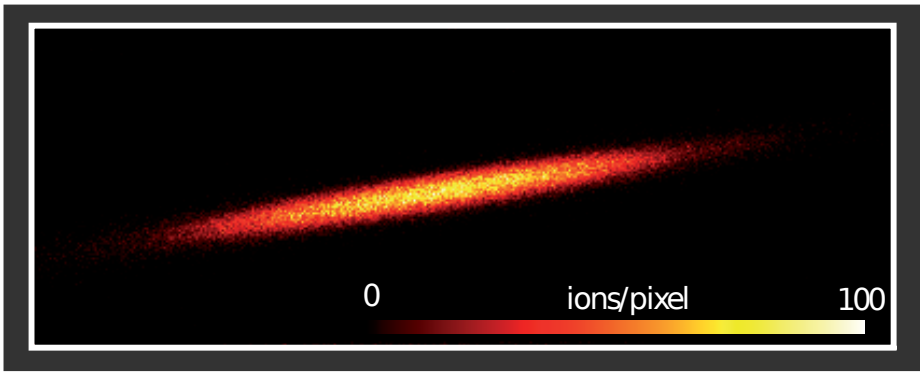

Figure 5.13: Sum of 300 single shot images. The image shows the sum of 300 single shot images, obtained in 300 individual measurements. Figure 5.12 is part of the presented sum of images, which has a total number of 10^5 ions.

5.3.3 Imaging a Bulk BEC

In a Bose-Einstein condensate all atoms occupy the same quantum state and the many-body wavefunction Ψ separates into the product of N identical single-particle wavefunctions ϕ

$$\Psi\left(\mathbf{x}_1, \ldots, \mathbf{x}_n\right) = \prod_{i=1}^{N} \phi\left(\mathbf{x}_i\right) \quad , \tag{5.3}$$

where N denotes the number of atoms in the condensate and $\mathbf{x}_i$ the atoms positions. Therefore the interpretation of the image involves quantum-mechanical concepts: as the single particle wave function ϕ extends over the whole atomic cloud, the spatially resolved detection of an atom can be understood as a projective measurement in position space. As a consequence, the retrieved image is intrinsically probabilistic. This is in contrast to almost all microscopy images showing the distribution of individual atoms, as in these cases the location of the atoms is already fixed prior to their detection. To check whether the obtained distribution in a single shot image is indeed a probabilistic selection, several images have to be summed and the result compared to a theoretical density profile. An image of 300 summed single shots can be seen in figure 5.13. Each BEC is only scanned once to reduce perturbations of the condensate. The total number of detected ions in the summed image is 10^5 which is comparable to the original number of atoms in the BEC.

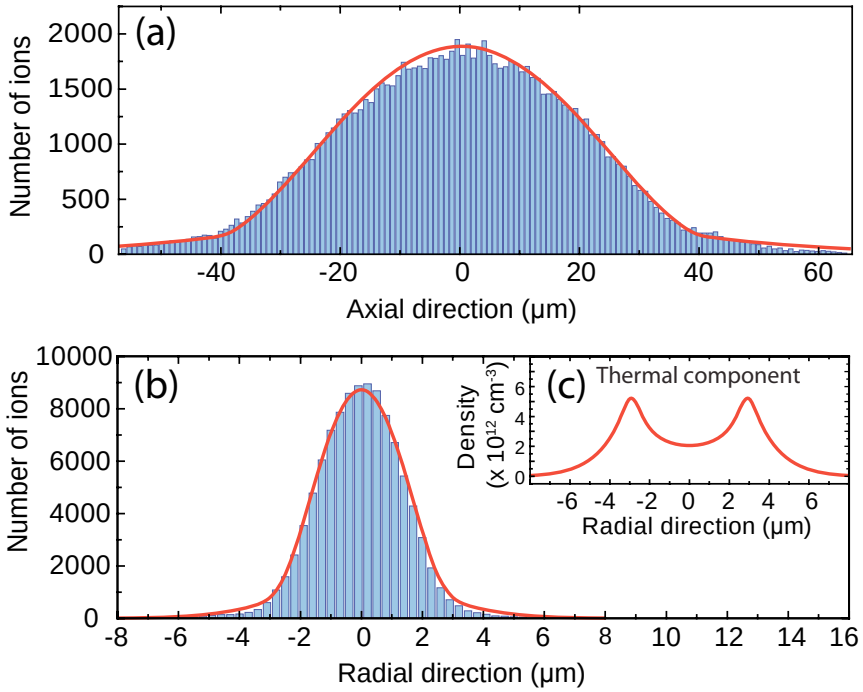

Figure 5.14: Analysis of a BEC. (a) and (b) show the measured axial and radial density distribution (blue columns) of the condensate, integrated along the radial and axial direction, respectively. The density distribution is compared to a theoretical distribution (red line) based on the semi-ideal model. (c) shows the radial density of the thermal component in the trap center as calculated from the model. The minimum is due to the repulsion from the condensate fraction.

The obtained density profile has to be compared to a theoretical density profile which is given by the semi-ideal model [61, 62, 63] and takes the repulsion of the thermal atoms by the condensate into account, see chapter 2.2.2. The solution $\Psi_0(\mathbf{r})$ of the time-independent Gross-Pitaevskii equation (2.49) is obtained numerically using the imaginary time propagation method [133, 134]. The solution describes the condensed atoms in the cloud and can be used to model a repulsive potential for the thermal atoms which is given in equation (2.71). As it can be seen in figure 5.14 the calculated density distribution agrees well with the experimental data. The calculated thermal component is shown in figure 5.14(c). Accordingly, it can be concluded that the single shot images are indeed a probabilistic selection of the atomic distribution.

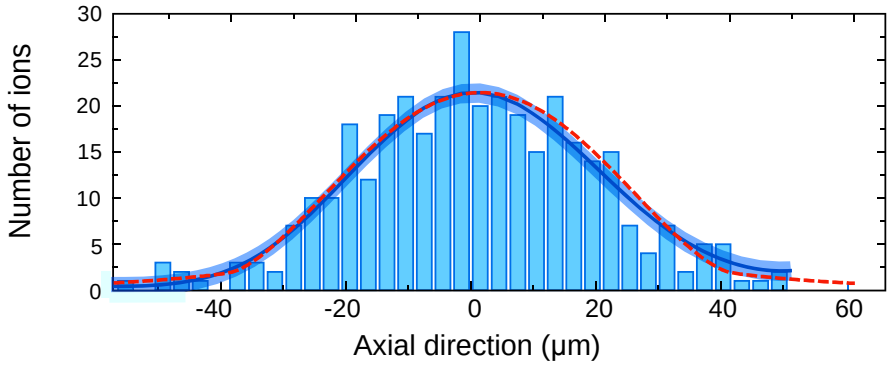

Figure 5.15: Estimated density distribution. The blue line shows the estimated density distribution in the axial direction for the single shot image in figure 5.12. The data is binned over 3 μm and is represented by the blue columns. The blue shaded area indicated the uncertainty of the estimated distribution. For comparison, the red, dashed line presents the solution of the theoretical modal and is the same as in figure 5.14(a).

The analysis in figure 5.14 gives an impression of how accurately the shape of the condensate would be determined if all atoms were detected in an idealized experiment. As the effective number of detected atoms per run is only 350 on average, the question of how much information can be extracted from a single image arises. This can be answered by applying a method for the reconstruction of a probability density from discrete experimental data [135]. This approach avoids the use of histograms and directly evaluates the cumulated data with the help of a Fourier expansion. It does not require the knowledge of the shape of the distribution. The estimated density distribution for the single shot shown in figure 5.12 is presented in figure 5.15. The shape in the center region is well reproduced and only the wings of the distribution show larger deviations due to poor statistics. By processing all 300 images of the images in figure 5.13 in the same manner and evaluating the FWHM of their density distribution, we find an average of 50.5 ± 2.5 μm. This is comparable with an FWHM of 48.9 μm obtained from the theoretical model in figure 5.14. Hence, the precision to which the size of the condensate is determined in a single image is 5%.

5.4 Perturbation and Heating of the Condensate

Electron microscopy of ultracold atoms is an imaging method that removes measured atoms from the ensemble by electron impact ionization. Hence, the question arises whether the removal of single atoms from the condensate changes the condensate itself during the imaging process. To ensure a measurement on the originally prepared quantum gas, the imaging process has to proceed faster than the propagation of information in the condensate. This means that an information about a perturbation reaches a position after it has been imaged.

5.4.1 Perturbations

Local perturbations in a Bose-Einstein condensate can be accessed in the framework of the microscopic theory developed by Bogoliubov, see section 2.1.3. One of the main results is, that the dispersion relation of perturbations features two characteristic regimes. The dispersion relation is free particle-like for high energies and phonon-like for low energies.

The high energy regime of the excitations corresponds to atoms with sufficiently high energies to leave the atomic cloud, which cannot be avoided.

The excitations in the low energy regime, which are phonon-like, propagate in the condensate with the sound velocity (see section 2.1.3)

$$c = \sqrt{\frac{4\pi\hbar^2 a_s n(\mathbf{r})}{m^2}} \quad . \tag{5.4}$$

The peak density in the condensate amounts to $n_0 = 6 \times 10^{13}\,\mathrm{cm}^{-3}$, which yields $c \sim 1.4\,\mathrm{mm/s}$. The imaging should therefore proceed faster than this to ensure that an unperturbed condensate is imaged.

The parameters for figure 5.13 are 400×150 pixel, with a pixel size of $300\,\mathrm{nm} \times 300\,\mathrm{nm}$ and a dwell time of $2\,\mu\mathrm{s}$, which corresponds to an image time of 120 ms and hence to an imaging speed of $v \sim 1\,\mathrm{mm/s}$. This is only slightly slower than the speed of sound in the center of the trap . From the absorption images taken after the illumination with the electron beam no sign of perturbation is found, see also next chapter.

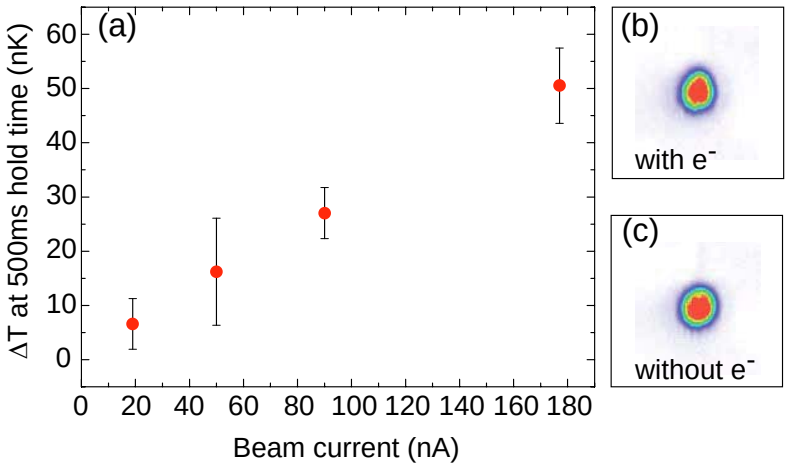

Figure 5.16: (a) shows the temperature difference between an illuminated and a non-illuminated atom cloud after a holding time of 500 ms. (b) presents the absorption image of an illuminated BEC and (c) shows the absorption image of a BEC that has not been illuminated. The electron beam has a beam diameter of 140 nm FWHM and a beam current of 20 nA. No significant difference between the two images can be found apart from a reduced atom number of 7%.

5.4.2 Heating

The effect of heating due to the imaging process with electrons is characterized by taking absorption images after the atom cloud has been illuminated with electrons. These images are compared to absorption images of a non-illuminated cloud. To measure the effect of heating on the atom cloud, a bimodal distribution with a condensate fraction of about 25% is prepared in the dipole trap. We subsequently rise the final trap intensity from 80 mW to 200 mW in 200 ms by a linear ramp in order to inhibit the loss of heated atoms. After the preparation the atom cloud is imaged with the electron beam using the same image parameters as in the scan shown in figure (5.13). After the exposure the atoms are held in the trap for 500 ms before they are imaged with absorption imaging. To account for long term drifts in the atom number, which results also in a temperature change, the atom cloud is exposed to the electron beam only every second run. A set of 100 measurements consists therefore of 50 illuminated and 50 non illuminated images are taken. We find for the temperature of the cloud that one imaging process with a beam current of 20 nA amounts to a heating of 6 nK. Figure

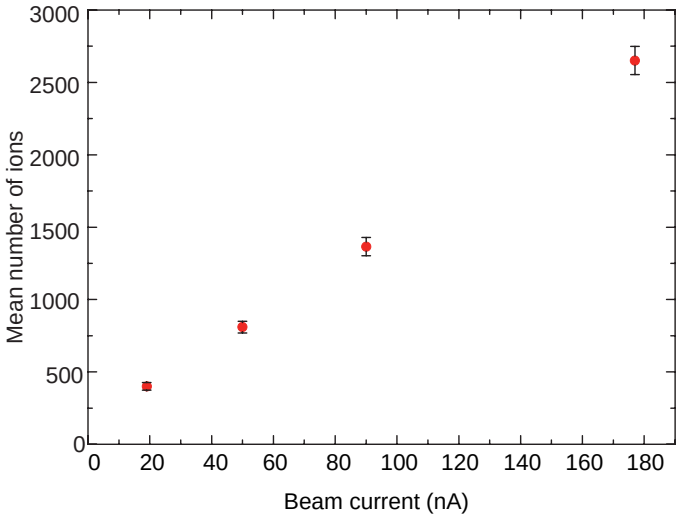

Figure 5.17: The mean number of detected ions in a single shot image.

5.16 shows the temperature gain of the atomic sample after the electron illumination for different electron beam currents.

The average atom loss in an imaging process is determined in a similar experiment, but without the additional ramp up of the optical dipole trap laser intensity. We find a typical atom loss of 7% (see also chapter 5.5). In conclusion, the effects of the imaging process on the atomic ensemble are very small and do not account for a limitation to the application of the imaging technique.

5.5 Detection Efficiency

In the last section of this chapter we will discuss the detection efficiency of the new imaging technique.

For an electron beam with a beam current of I, the number of scattered atoms can be approximated for short dwell times by

$$N_{\mathrm{scat}} = N\sigma_{\mathrm{tot}}\frac{IT}{eA} \quad , \tag{5.5}$$

where N denotes the number of atoms in the sample, σ_{tot} represents the total scattering cross section (3.29), the electron charge is labeled by e, and

T and A represent the image duration and area, respectively. Using equation (5.5) we find that about 3000 atoms are scattered by electrons in each of the single shot image composing figure 5.13. We find a typical atom loss of 7% for the imaging process in these measurements. This corresponds to 7000 atoms, and we therefore conclude that about one additional atom is lost for every scattered atom.

To obtain the number of ionized atoms N_{ion} one has to replace the total scattering cross section in (5.5) by the ionization cross section (3.28). For the single shot images of figure 5.13 this number amounts to 1200 ions. This number has to be compared to the number of detected ions N_{det} which is given by

$$N_{\text{det}} = N_{\text{ion}} \times \eta_{\text{det}} \quad , \tag{5.6}$$

where η_{det} represents the detection efficiency, being a product of the unknown detector efficiency η_{chan}, and the efficiency of the ion optics η_{ion}. From the detected number of ions and the number of ionized atoms we find a detector efficiency of 30% . Figure 5.17 shows the mean number of detected ions in a single shot image for different beam currents, which shows that the number of produced ions is proportional to the current. The detection efficiency of the method is then given by

$$\eta = \eta_{\text{prod}} \times \eta_{\text{det}} \quad . \tag{5.7}$$

With a production efficiency η_{prod} of 40% we find an overall detection efficiency of 12% .

5.6 Conclusion

By imaging the *in situ* density distribution of a ^{87}Rb Bose-Einstein condensate, with good agreement to the theoretical density profile, the functionality of the method was demonstrated. Moreover, the perturbation caused by the detection process is very small, which provides the possibility of complementary measurements in position and momentum space of a single many-body system. The current detection efficiency of the system is so far limited to 12%, which could be increased by a more efficient ion detection hardware. However, it should be possible to increase the detection efficiency by subsequent photoionization of inelastically scattered atoms [85]. The small perturbation of the system in combination with a higher detection efficiency could allow for the repeated imaging of the same condensate for a direct observation of the dynamic evolution of a system.

Chapter 6

Single Site Resolution Imaging and Manipulation of Optical Lattices

In the previous chapter 5, the working principle and functionality of the imaging technique was demonstrated by probing the density distribution of a Bose-Einstein condensate in an optical dipole trap. The results are in good agreement with the theoretical description, but do not yet allow for the determination of the spatial resolution of the imaging method. In order to determine the resolution, a target with a known structure is needed. A Bose-Einstein condensate loaded in an optical lattice constitutes a perfect candidate for a periodically structured target. Furthermore, optical lattices provide a artificial crystal to study condensed matter phenomena and represent a broad research area in the field of ultracold quantum gases.

There are ambitions to use lattice-based systems of ultracold atoms as quantum simulators [136, 137] or to investigate unsolved problems in the field of condensed-matter physics [28]. Furthermore, a system of 10^4 or more periodically ordered particles would constitute a truly large-scale system for implementations in quantum information processing [138]. However, for many applications it is either helpful or imperative to resolve and even manipulate single lattice sites of an optical lattice. Whereas the manipulation of single lattice sites demands a better spatial resolution than the mere image.

This chapter discusses the high resolution imaging and manipulation of ultracold atoms, confined in an optical lattice potential. We start with a brief

introduction on the properties of periodic potentials as traps for ultracold bosonic samples. After the presentation of the experimental lattice setup, we will concentrate on high resolution imaging of ultracold atoms in one- and two-dimensional optical lattices. Finally, the capability of the imaging technique to address and manipulate single lattice sites is demonstrated by creating geometrically tailored quantum systems.

6.1 Bose-Einstein Condensates in Optical Lattices

Optical lattices are usually obtained by two, or more interfering laser beams that form a standing wave. Due to the optical dipole potential, caused by detuned light, the standing wave represents a periodic potential for neutral atoms. This forms a model solid state system in which the neutral atoms play the role of electrons. An advantage of optical lattices when mimicking a solid state system is, that all parameters can be controlled by the employed light. The lattices constant depends on the wavelength and the angle under which the laser beams interfere, whereas the potential depth can be set by the laser power. In order to represent a valid model system the lattice constant of the periodic potential should enable sufficient high tunnel rates between neighboring sites for small lattice depth and moreover suppress tunneling between second neighbors. For bosonic atoms this regime is known as the Bose-Hubbard regime and achieved so far for lattice constants between 400 nm and 600 nm.

6.1.1 Periodic Optical Dipole Potentials

Optical dipole traps offer a wide range of possible trapping geometries depending only on the chosen beam geometry. A periodic potential structure can be obtained by two superimposed counter propagating laser beams. If these beams interfere, the resulting interference pattern forms a periodic potential. For a review and further information than can be given in this section, see reference [139] and references therein.

One Dimensional Lattice Potential

The simplest possible periodic structure is a one dimensional optical lattice, which can be obtained by retro-reflecting a Gaussian laser beam. The electric field amplitude of a Gaussian laser beam, which travels along the

$\hat{e}_z$-direction with a wave vector $\mathbf{k}$ and neglecting polarization effects, is described by

$$E(\varrho, z, t) = E_0 e^{-\varrho^2/w^2} \cdot \mathrm{Re}\left[e^{i\mathbf{k}\cdot\mathbf{z}} \cdot e^{i\omega t}\right] \quad , \tag{6.1}$$

where ϱ stands for the radial coordinate in the plane perpendicular to the propagation direction and w denotes the beam waist of the focused beam. For two counter propagating laser beam with wave vectors $\mathbf{k_1} = \mathbf{k}$ and $\mathbf{k_2} = -\mathbf{k}$, respectively the resulting interference patter of the intensity integrated over time is given by

$$I(\varrho, z) = |E_k(\varrho, z, t) + E_{-k}(\varrho, z, t)|^2 = 4E_0 e^{-2\frac{\varrho^2}{w^2}} \cos^2(kz) \quad . \tag{6.2}$$

In the following, we will consider only laser frequencies which are red detuned with respect to the atomic transition frequency ($\omega < \omega_0$), because all experiments with optical lattices presented below have been performed with red detuned potentials. As it has been discussed in section 4.2.2, the atoms are attracted by the anti nodes of the standing wave (6.2). The optical dipole potential of this intensity distribution is

$$V_{\mathrm{dip}}(\varrho, z) = -V_0 \cdot e^{-2\frac{\varrho^2}{w^2}} \cdot \cos^2(kz) \quad , \tag{6.3}$$

where $k = 2\pi/\lambda$ denotes the absolute value of the wave vector, λ stands for the laser wavelength, and V_0 is the maximal achievable potential depth, which is four times larger than the potential depth of the laser beam without retro-reflection due to the constructive interference. The potential created by a retro-reflected beam is periodic along the propagation direction with periodicity of $\lambda/2$. The minima of the potential (6.3) will from now on be referred to as lattice sites. A transverse confinement of the atoms is given by the Gaussian profile of the beam in the plane perpendicular to its propagation.

In the more general case of beams intersecting under an angle θ as depicted in figure 6.1 the lattice spacing d is given by

$$d = \frac{\lambda}{2\sin(\theta/2)} \quad , \tag{6.4}$$

including the case of retro-reflection for $\theta = \pi$. The absolute value of the lattice wave vector than amounts to

$$k_{\mathrm{lat}} = \frac{\pi}{d} = \frac{2\pi}{\lambda} \cdot \sin(\theta/2) \quad . \tag{6.5}$$

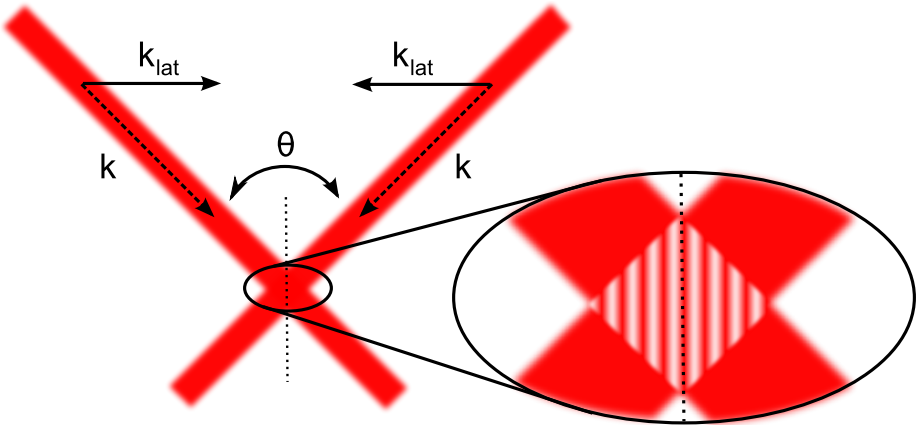

Figure 6.1: An optical lattice formed by two interfering laser beams under an angle θ. The polarization is linear and perpendicular to the image plane. The reciprocal lattice vector k_{lat} which is related to the k-vectors of the individual laser beams is given by $k_{lat} = k \sin(\theta/2)$.

It is convenient to express the depth of the lattice potential in units of the recoil energy

$$E_R = \frac{\hbar^2 k_{\mathrm{lat}}^2}{2m} \quad , \tag{6.6}$$

where m stands for the mass of a single atom and k_{lat} is the lattice wave vector defined by equation (6.5). The lattice depth is then denoted by $s = V_0/E_R$.

Dimensionality

So far the discussion of optical lattice potentials considered solely the one dimensional case. However, the concept can be extended to two and three dimensional optical lattices, by adding another pair of laser beams for each axis. Depending whether all of these individual laser beams interfere or only the counter propagating pairs, one has to distinguish two cases. If multiple beams interfere, they will form an interference pattern depending on the relative phase of the beams [95, 140]. In the simple case in which the different axes are detuned from another or have different polarizations, the problem separates and each axis forms an independent one dimensional lattice. The optical lattices in the presented experiments are detuned from each other and have perpendicular polarizations so that they always separate. A 1D lattice cuts a cigar shaped BEC into pancake-like structures, a 2D lattice forms tubes perpendicular to the two axes, and with a 3D optical

lattices one can realize a simple cubic crystal. By using different potential depths on one or two lattice axes it is possible to freeze out the motion of the atoms in these directions and create low dimensional systems in the remaining axes.

6.1.2 Band Structure and Bloch Waves

The concept of a particle in a periodic potential is a familiar problem in solid state physics, where the periodic potential is formed by the periodic arranged ions in the solid. A characteristic for the movement of electrons in such a periodic potential is the emergence of a structure of energy bands. The dispersion relation is no longer continuous as in the free particle case, but shows certain forbidden regions which arise from the periodic potential.

The same techniques apply to ultracold atoms in optical lattices. Since the single axes of higher dimensional lattices separate, the discussion of an atom in a periodic optical potential can be restricted to one dimension. For a more detailed description and further information than can be given in this section see [141, 142].

A single atom in a periodic potential $V(x)$ with periodicity d is described by the Schrödinger equation

$$\hat{H}\Phi_q^{(n)} = E_q^{(n)}\Phi_q^{(n)} \qquad \text{with} \qquad \hat{H} = \frac{1}{2m}\hat{p}^2 + \hat{V}_{\text{lat}}(x) \quad , \tag{6.7}$$

where $\hat{p}$ stands for the momentum operator of the atom and m for the atomic mass. The index n denotes the energy band and the Schrödinger equation (6.7) has to be solved for each energy band to find the corresponding eigenfunctions $\Phi_q^{(n)}$ and eigenvalues $E_q^{(n)}$. The quasi momentum q characterizes the phase difference between different lattice sites. If a BEC, which is fixed relative to the optical lattice, is loaded into the periodic potential a state with $q = 0$ will be prepared. The solutions of the Schrödinger equation are called Bloch functions. They are a product of a plane wave $\exp(iqx/\hbar)$ and a function $u_q^{(n)}(x)$ which has the same periodicity d as the lattice potential

$$\Phi_q^{(n)} = e^{\frac{iqx}{\hbar}} u_q^{(n)}(x) \quad . \tag{6.8}$$

Since the quasi momentum q is only unique up to the reciprocal lattice vector k_{lat}, it is convenient to restrict it to the first Brillouin zone

$$-\hbar k_{\text{lat}} < q < \hbar k_{\text{lat}} \quad . \tag{6.9}$$

Numerical Solution

A solution for the Schrödinger equation (6.7) can be found by inserting the ansatz (6.8) into (6.7) [140]. A periodic function $f(x)$ with periodicity τ can be expressed as a Fourier series

$$f(x) = \sum_j c_j e^{i\frac{2\pi}{\tau}jx} \quad , \tag{6.10}$$

where c_j denotes the Fourier coefficients. The potential $V(x)$ and the function $u_q^{(n)}(x)$ share by definition the same periodicity $d = \pi/k_{\mathrm{lat}}$, their Fourier expansion is therefore given by:

$$V_{\mathrm{lat}}(x) = \sum_l V_l e^{i2lk_{\mathrm{lat}}x} \qquad \text{and} \qquad u_q^{(n)}(x) = \sum_m c_m^{(n,q)} e^{i2mk_{\mathrm{lat}}x} \quad . \tag{6.11}$$

The periodic potential can be as well written in complex notation and is then given by

$$V_{\mathrm{lat}}(x) = V_{\mathrm{dip}}(x) = -V_0 \cos^2(k_{\mathrm{lat}}x) = -\frac{1}{4}V_0\left(e^{2ik_{\mathrm{lat}}x} + e^{-2ik_{\mathrm{lat}}x} + 2\right). \tag{6.12}$$

Comparing the coefficients with equation (6.11) only the terms with $l = \pm 1$ and $l = 0$ contribute in the expansion of the potential. Inserting this into equation (6.7) yields

$$\sum_l H_{l,l'} c_l^{(n,l)} = E_q^{(n)} c_l^{(n,l)} \quad , \tag{6.13}$$

with

$$H_{l,l'} = \begin{cases} (2l + q/\hbar k_{\mathrm{lat}})^2 E_R - V_0/2 & \text{for} \quad l = l' \\ -1/4V_0 & \text{for} \quad |l - l'| = 1 \\ 0 & \text{else} \end{cases} \quad , \tag{6.14}$$

being a symmetrical square matrix and E_R the recoil energy. The coefficients $c_l^{(n,l)}$ become negligibly small for large $|l|$. One can therefore restrict the matrix to $-5 \leq l \leq +5$ [143]. The resulting 11×11 matrix can be diagonalized by a computer algebra system. Both, the dispersion relation, which is depicted in figure 6.2, and the Fourier coefficients $c_l^{(n,l)}$ for the Bloch function are obtained from the diagonalized matrix.

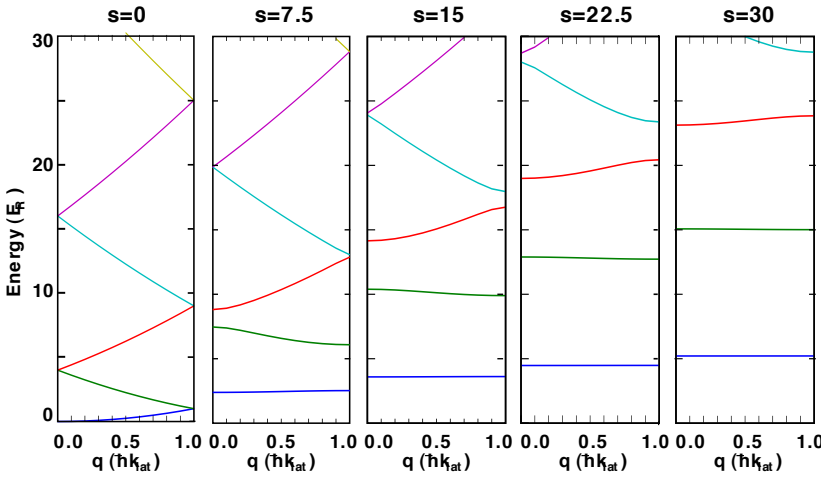

Figure 6.2: Dispersion relation for an atom in an optical lattice. The energy in units of the recoil energy E_R is shown on the ordinate and the quasi-momentum q in units of $\hbar k_{\mathrm{lat}}$ is depicted on the abscissas. Since the dispersion relation for a simple cubic lattice is symmetric, the reduced zone scheme is only depicted for positive quasi momenta. For no lattice, i.e. $s = 0$ the parabola of a free particle is recovered. A band structure with an energy gap between the energy levels emerges for higher lattice depths. For very deep lattices the levels converge to the discrete level scheme of a quantum harmonic oscillator.

Wannier Functions

The Bloch functions represent a complete set of solutions in momentum space. They are completely delocalized in position space. To obtain solutions which are a basis set in position space one can take the Fourier transform

$$\mathcal{W}_n\left(x - x_i\right) = \frac{1}{\sqrt{\mathcal{N}}} \sum_q e^{-iqx_i/\hbar} \Phi_q^{(n)}\left(x\right) \quad . \tag{6.15}$$

The functions $\mathcal{W}_n\left(x - x_i\right)$ are called Wannier functions, $\mathcal{N}$ is a normalization factor and n gives the band index. The Wannier functions are wave packets of Bloch functions centered around a lattice site x_i. This means that Wannier functions are well suited to calculate local properties of a single lattice site. For shallower lattices the Wannier function is localized at one lattices site but has wings which overlap with the adjacent sites. This results in a higher overlap integral and therefore in higher tunneling rates.

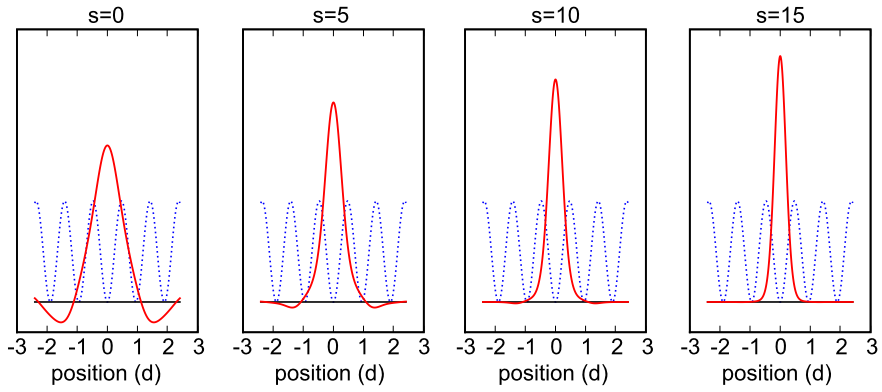

Figure 6.3: Wannier functions of the first band of a 1D lattice for different lattice depths. The localized Wannier functions (solid red line) overlap with the neighboring lattice sites in the case of a shallow lattice. The deeper the optical lattice is, the more the Wannier function approaches a Gaussian. The dotted blue line indicates the periodicity of the optical lattice.

As one can see in figure 6.3 the wings of the Wannier function overlap more with neighboring lattice sites for shallow lattices. The deeper the lattice the more the Wannier function resembles a Gaussian. The overlap with the neighboring sites is suppressed and the tunneling rate is smaller.

Harmonic Approximation

For deep lattices the Wannier function can be approximated by a Gaussian. This is consistent with a harmonic approximation of the trapping potential. The trapping frequencies at a single lattice site are given by

$$\omega_{\mathrm{lat}}^2 = \frac{1}{m}\frac{\partial^2 V(x)}{\partial x^2} \quad . \tag{6.16}$$

In case of the harmonic approximation this simplifies to

$$\omega_{\mathrm{lat,harm}}^2 = V_0 \frac{2k_{\mathrm{lat}}^2}{m} \quad . \tag{6.17}$$

As one can see from figure 6.4 the harmonic approximation overestimates the trapping frequency for a given potential depth.

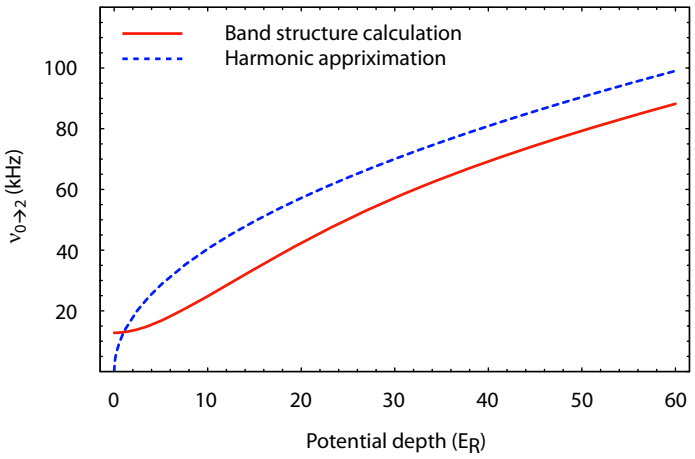

Figure 6.4: The solid red curve shows the transition frequency from the lowest band to the second band, calculated with a band structure calculation. The dashed blue curve gives the same transition frequency in the harmonic approximation. For a given potential depth the harmonic approximation overestimates the transition frequency.

6.2 Realization and Imaging of Optical Lattices

After the brief review of Bose-Einstein condensates in optical lattices, we will now attend to the realization and imaging of ultracold atoms in periodic potentials.

Starting with the experimental setup of the laser system for the lattice potential, we outline the loading scheme of the latter. On the basis of atoms in a 1D optical lattice as a structured target, we determine an upper boundary for our imaging systems resolution.

6.2.1 Experimental Setup

The laser light for the optical lattices is provided by two tapered amplifiers, each set to a wavelength of 852 nm. The first TA[1] provides a beam with up to 300 mW of laser power, while the second laser[2] supplies laser light with 290 mW. The wavelength of both lasers is stabilized on a cesium transition

[1] TA: Toptica TA-0850-0500 (500mW), diode: Uniphase SDL-5411-G1 (100mW)
[2] TA: Eagleyard EYP-TPA-0850 (1W), diode: Uniphase SDL-5411-G1 (100mW)

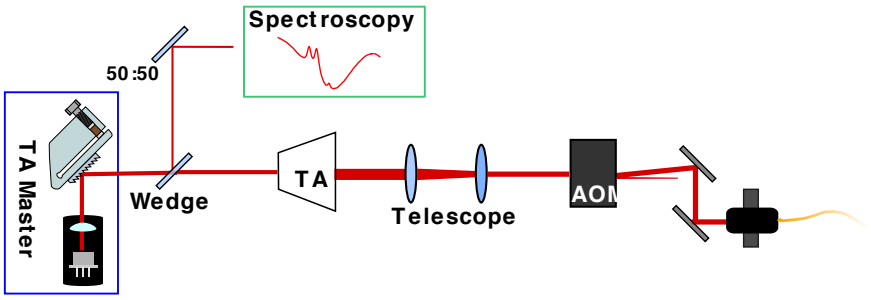

Figure 6.5: Setup of the laser system for the optical lattices. A grating stabilized diode laser is amplified by a tapered amplifier. A small part of the beam is used to frequency stabilize the seed laser. The beam from the TA is then demagnified with a telescope and adjusted through an AOM. The first deflection order is coupled into an optical fiber.

via a Doppler free spectroscopy. The laser setup for the optical lattices is illustrated in figure 6.5.

Each laser beam is coupled into an optical fibers to clean the mode profile. The intensity of each lattice beam is actively controlled by a stabilization unit that adjusts the RF power of an AOM and thereby the beam intensity. For this, a small fraction of the beam is coupled out and monitored on a photo diode. The signal voltage of this photo diode is fed to the active stabilization unit, which compares the measured value to a reference voltage of a waveform generator[3]. The stabilization unit has a bandwidth of 100 kHz.

The experimental setup with the electron microscope in the vertical axis and the CO_2 optical dipole trap restricts the optical access for the lattices. The ZnSn windows and lenses for the dipole trap are not transparent for near infrared light of the optical lattices so that a retro reflected lattice along the dipole trap cannot be realized. The lattice is therefore accomplished by two interfering laser beams which intersect under an angle of 90° as it can be seen in figure 6.6 The two beams are obtained by splitting one beam into two using a half wave plate and a polarizing beam splitter cube. The perpendicular, second lattice is build in the same way. The beam diameters at the position of the atoms are 120 μm for the axis along the dipole trap and 200 μm for the second lattice axis perpendicular to the dipole trap. Equation (6.4) shows that the wavelength and the configura-

[3] Agilent 33220A

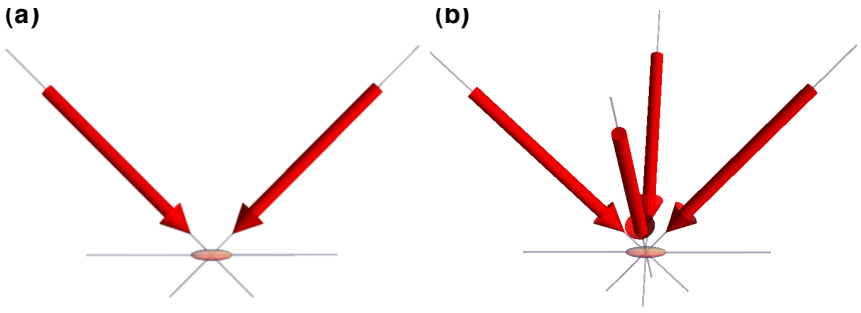

Figure 6.6: Beam configuration of the 1D and 2D optical lattice. The lattices are formed by two laser beams which interfere under an angle of $\pi/2$. (a) shows the configuration of first lattice axis and (b) the configuration of the 2D optical lattice. The two sets of laser beams form independent interference patters since they are detuned by 160 MHz and have perpendicular polarizations. The 1D lattice in (a) forms pancake like structures perpendicular to the dipole trap. The 2D lattice in (b) forms vertical tubes. Image taken from [144].

tion of the lattice produce a periodic potential with a spacing of 600 nm. A detailed description of the optical lattice setup can be found in [95, 144].

Preparation of a BEC in an Optical Lattices

In order to load a BEC into a periodic potential, all laser beams that form the optical lattice have to be superimposed at the position of the BEC. To

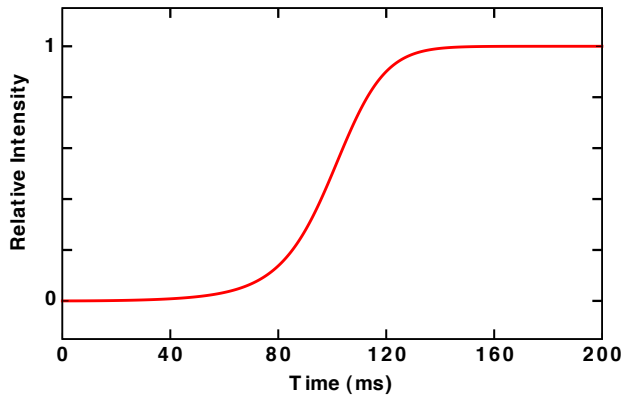

Figure 6.7: s-shaped waveform used to ramp up the optical lattice potential.

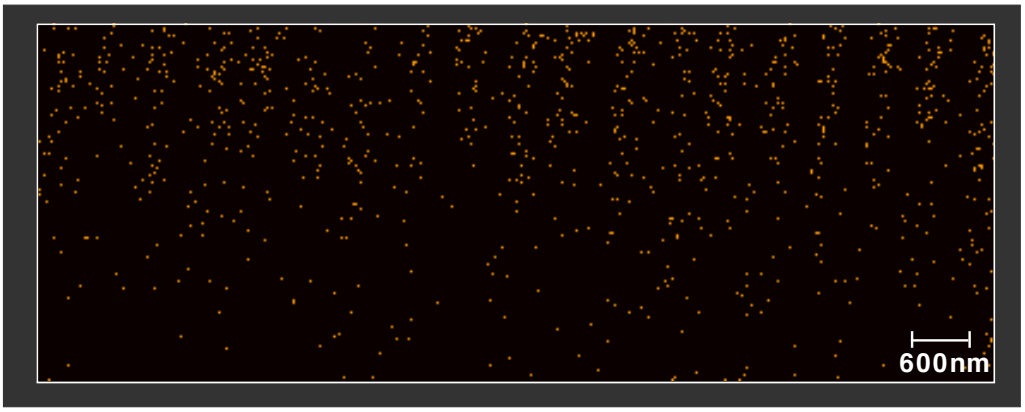

Figure 6.8: Single shot image of an 1D optical lattice with a period of $d = 600\,\mathrm{nm}$. The image size is 150×400 pixels with a pixel size of $25\,\mathrm{nm} \times 25\,\mathrm{nm}$ and a pixel dwell time of $2\,\mu\mathrm{s}$.

avoid cross interference between the standing waves, both lattice axes have orthogonal polarization and are detuned by 160 MHz in order to average any residual interference patterns on a time scale of a few tens of nano seconds.

To avoid any excitation in the system, especially population of higher vibrational bands, the intensity of the laser beams is slowly increased. The ramps have a s-shape [145] and last 200 ms. Figure 6.7 shows the waveform which is used to ramp up the optical lattice potential. The maximal available light intensity is 104 mW for the parallel and 80 mW for the perpendicular axis. This corresponds to a lattice depth of up to $20\,\mathrm{E}_R$.

6.2.2 Resolving Single Sites of an 1D Lattice

The working principle for imaging the density distribution of ultracold atoms in an optical lattice is the same as described in section 5.3 for a Bose-Einstein condensate. The BEC is prepared underneath the electron microscope and loaded into the optical lattice potential. The sample is held in place while it is scanned with the focused electron beam as depicted in figure 5.10.

Figure 6.8 presents a single shot image of atoms in an 1D lattice. The image size is 150×400 pixels with a pixel size of $25\,\mathrm{nm} \times 25\,\mathrm{nm}$. The dwell time on each pixel is $2\,\mu\mathrm{s}$, which leads to a total imaging time of 120 ms. The electron beam current and the FWHM diameter were 10 nA and 95 nm.

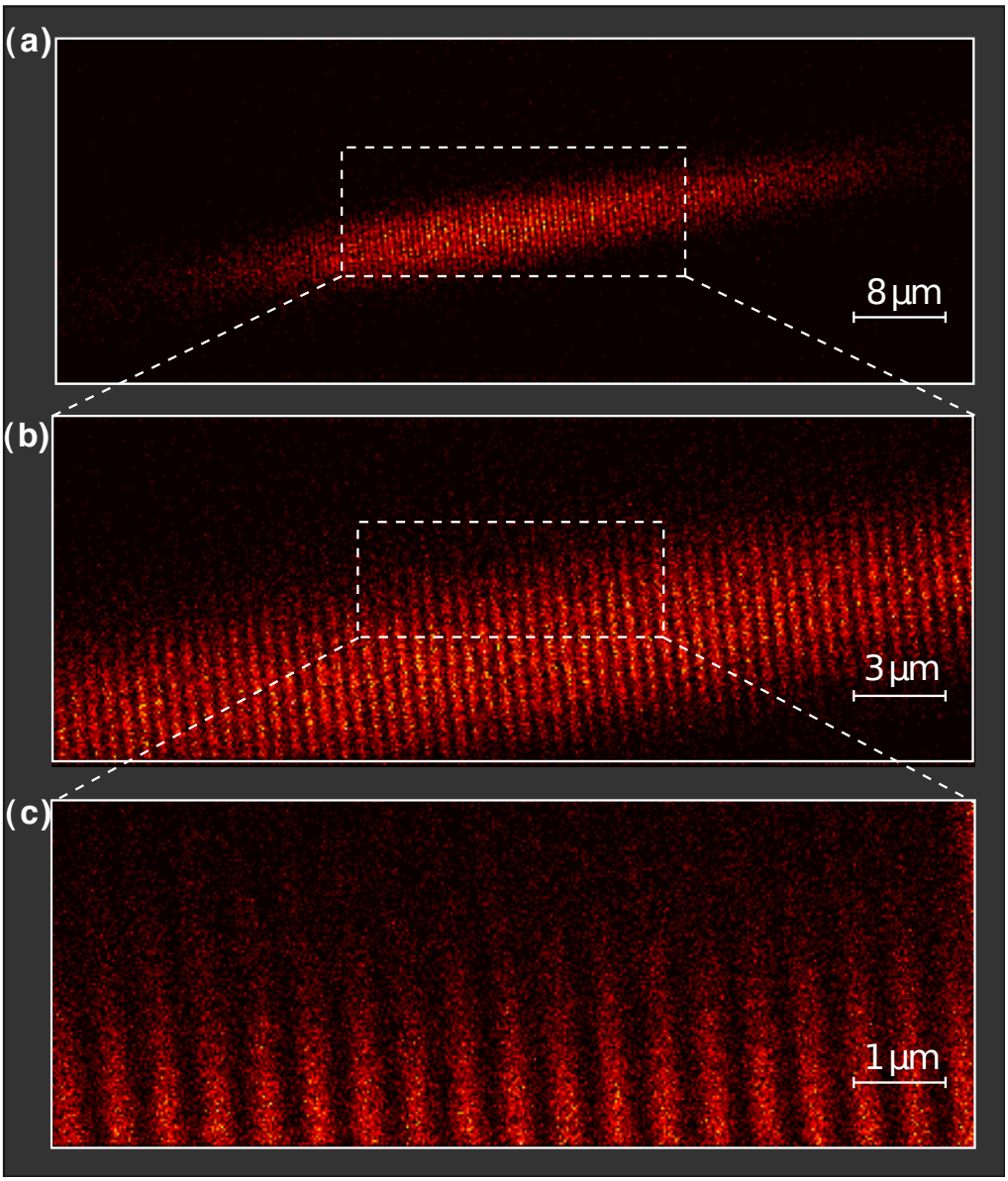

Figure 6.9: Images of a Bose-Einstein condensate loaded in an 1D optical lattice along the dipole trap axis. Each image is the sum of 50 individual images with an average number of ions of 350 for (a), 1200 for (b), and 1100 for (c). The images have a size of 150×400 pixels with a pixel size of $200\,\text{nm} \times 200\,\text{nm}$ in (a), $75\,\text{nm} \times 75\,\text{nm}$ in (b), and $25\,\text{nm} \times 25\,\text{nm}$ in (c). The FWHM diameter of the electron beam is 95 nm.

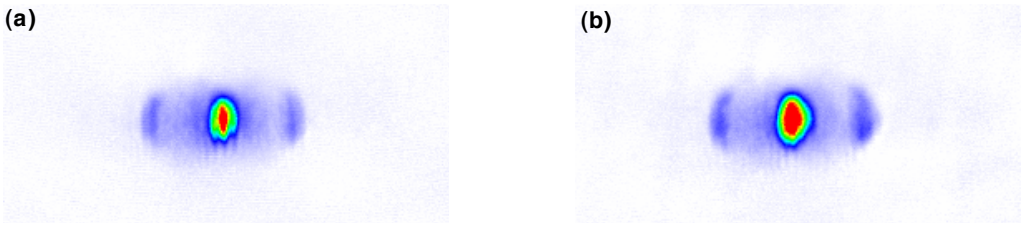

Figure 6.10: (a) presents the absorption image of an 1D lattice that was illuminated by the electron beam, while (b) shows the corresponding image without electron beam exposure.

The optical lattice has a period of $d = 600\,\mathrm{nm}$ and a depth of $18\,\mathrm{E}_R$. The image is composed of about 1000 single ions. This is already enough data to reveal the one dimension periodic structure of about 19 lattice sites.

Figure 6.9 shows a sequence of electron microscope images of the one dimensional optical lattice with increasing resolution. The atomic density distribution in each lattice well has a radially symmetric pancake-shape, with a diameter of 6 μm and a thickness of 300 nm. Using an electron beam with a FWHM diameter of 95 nm the periodic structure of the lattice potential is clearly resolved with high contrast. This documents the large depth of focus of the electron optical imaging system.

Conservation of Phase Coherence

In the preceding section, we showed that it is possible to image the density distribution of atoms trapped in a periodic optical potential with the aid of a focused electron beam. The information of this distribution is received from the subset of atoms which is ionized by the electron beam. We now will examine the effect of the imaging process on the remaining atoms in the optical lattice.

One of the most remarkable properties of a Bose-Einstein condensate is its macroscopic phase coherence. In lattice potentials, this phase coherence can easily be verified by the interference pattern formed by the atoms in time of flight. Two absorption images of the atoms after a ballistic expansion of 15 ms, with and without exposure to the electron beam are shown in figure 6.10. The only visible difference is a loss of atoms, comparable to the case of a BEC in the dipole trap discussed in section 5.4.2. The appearance of the characteristic diffraction peaks demonstrates that the

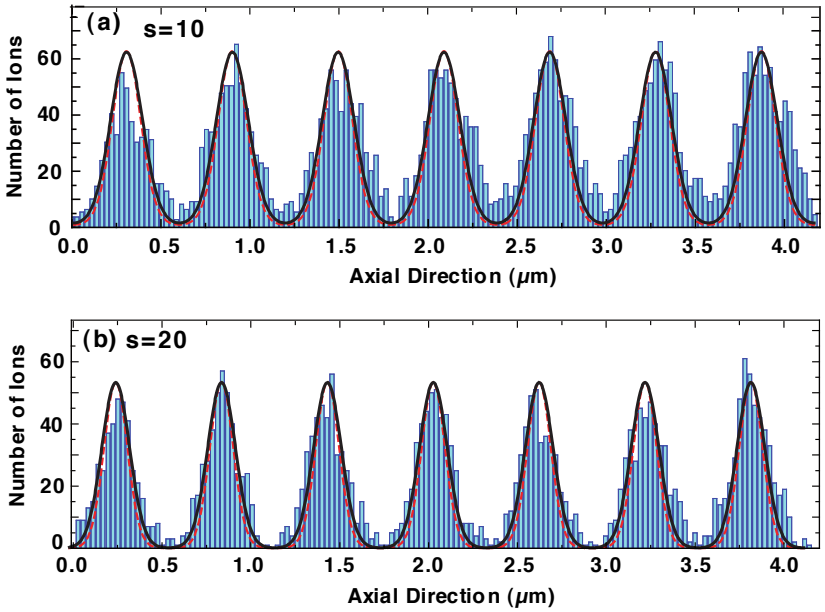

Figure 6.11: Ground state of a BEC in a 1D optical lattice. The graphs show integrated line scans for a lattice depth of $s = 10$ (a) and $s = 20$ (b). The blue columns are the experimental data, which are compared to a theoretical model (black line) based on the ground state in the lattice potential (red, dashed line) convoled with a Gaussian electron beam profile with 95 nm FWHM.

partial measurement of a subset of atoms does not destroy the coherence of the remaining system. Furthermore, this is an example of a complementary measurement in position and momentum space on a single many-body quantum system.

Determination of Resolution

For a quantitative analysis of the measured density distribution the obtained data has to be compared to the theoretical model. In a non-interacting model, this density distribution is given by Bloch functions (6.8). Furthermore, a model that describes the outcome of the imaging process has to take into account the finite extension of the electron beam. This means that the Bloch functions have to be convolved with the electron beam profile. A comparison between the obtained data and the theoretical model is presented in figure 6.11. The image shows the integrated line scans of a one dimensional lattice for lattice depths of $s = 10$ and $s = 20$. These

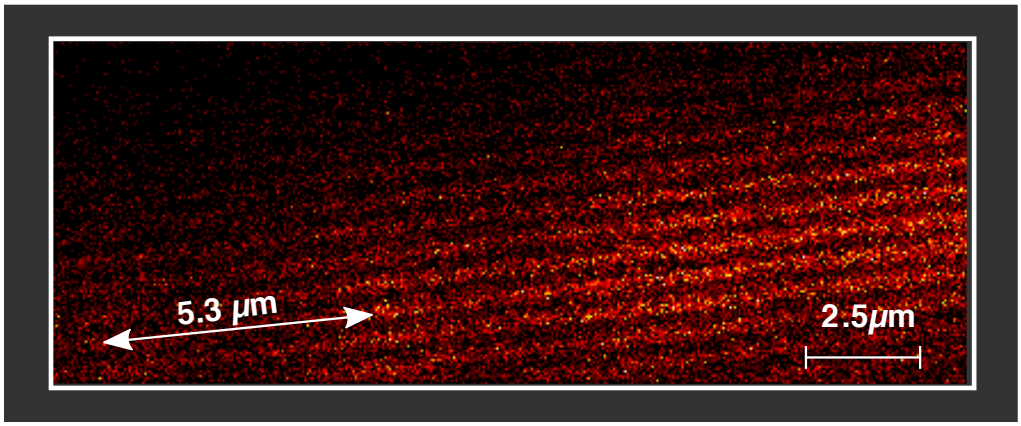

Figure 6.12: Image of a Bose-Einstein condensate loaded in a one-dimensional optical lattice with a depth of $18E_R$ perpendicular to the dipole trap axis. The image is the sum of 50 individual images with an average number of 900 ions. Each image consists of 150×400 pixels, with a pixel size of $50\,\text{nm} \times 50\,\text{nm}$. The pixel dwell time is $2\,\mu$s and the electron beam has a focus diameter of 95 nm FWHM. The additional periodic structure which is visible along the optical dipole trap axis is caused by a small retro-reflection of the CO_2 laser.

line scans are compared to the corresponding Bloch functions with zero quasi-momentum convolved with an electron beam of 95 nm FWHM. The periodic structure and the shape of the individual on-site wave functions are well reproduced for both data sets.

Although the size of the electron beam can be determined independently by scanning the beam across the edge of the test target hole, as described in section 5.1.1 the actual resolution of the imaging system is unknown. We define the resolution as the distance between two neighboring point-like scatterers where the signal intensity in between drops to 75%. This definition is analogue to the Rayleigh criterion [146] in optics and translate into a resolution of

$$r = 1.18\,\text{FWHM} \tag{6.18}$$

assuming a Gaussian beam profile. For an electron beam with a FWHM diameter of 95 nm this corresponds to a resolution of 115 nm. We conclude from the good agreement between the experimental line scan and the theoretical model in figure 6.11, that our imaging technique indeed achieves a

spatial resolution of better than 150 nm [96]. The spatial resolution can be further improved by using an electron beam with a smaller diameter.

Second Axis

In order to extend the existing 1D lattice to a 2D lattice, a second, orthogonal lattice is needed. Figure 6.12 shows an image of the second optical lattice which also has a period of 600 nm.

The atomic density distribution at each lattice site resembles an ellipsoid, with a short half axis of 6 μm, a long half axis of 100 μm, and a thickness of 300 nm. A slight periodic density modulation orthogonal to the lattice axis is visible in figure 6.12. This is caused by a small retro-reflection of the CO_2 dipole trap. Although the periodic structure of the lattice potential is resolved, the lattice structure is not reproduced with the same high contrast as the first lattice axis. The reason for this will be discussed in the following section.

6.2.3 Resolving Single Sites of a 2D lattice

After imaging each lattice axis individually, figure 6.13 presents a single shot image of a 2D optical lattice. Like in figure 6.8 where the single shot image of a 1D lattice is shown, this is enough data to reveal the two dimensional periodic structure, showing approximately 90 lattice sites. Again, the statistics can be further improved by summing over several experimental runs. Figure 6.14 presents the results for increasing image resolution. For each image 30 experimental runs are summed.

Approximately, 1200 lattice sites are occupied with atoms, which can be deduced from the extension of the cloud in figure 6.14 (a). For a typical condensate with about 10^5 atoms this results in an average occupancy of 80 atoms per site. The typical number in the center of the cloud is significantly higher, due to higher atomic densities.

Image Correction

The optical lattices can exhibit short and long term drifts, which is revealed in a blurring of the summed image. This can be seen in figure 6.15, which shows a comparison of 50 (a) and 300 (b) summed images of the second lattice axis. Although the lattice structure is clearly visible for 50 summed image, it has almost completely vanished for 300. To understand this effect,

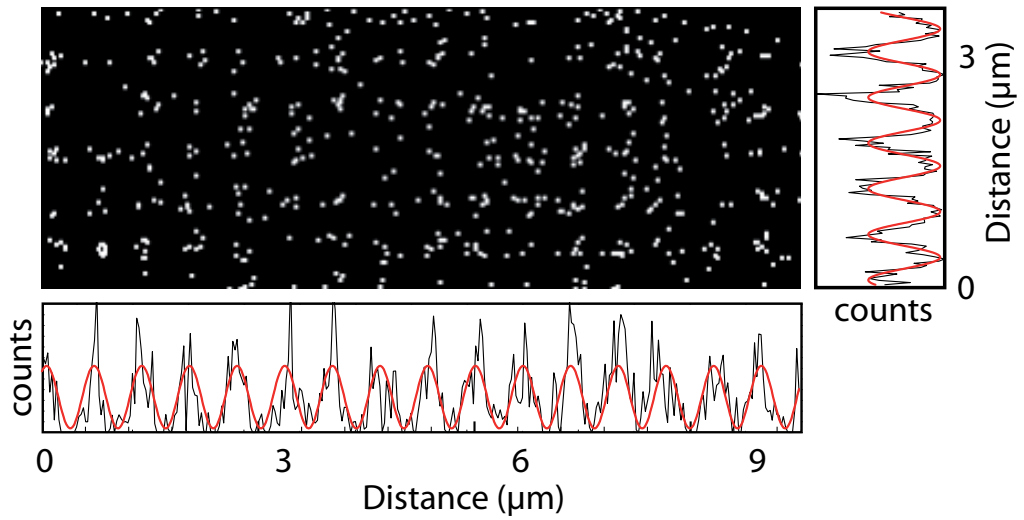

Figure 6.13: Single shot image of the central part of the cloud. Each dot corresponds to a detected ion. The 2D lattice has a lattice depth of 18 E_R. The image consists of 150×400 pixels with a pixel size of $50\text{nm} \times 50\text{nm}$. The pixel dwell time is 2μs and the electron beam diameter is 95nm FWHM. The image is composed of 800 single ions. The integrated line scans, represented by the black lines, are shown on the side. The red line is a sine fit to the data which can be used to determine the position of the lattice.

the position of the lattice sites in each image is analyzed [147]. The position of the lattice sites is characterized by the phase of the sine function, which is fitted to each line scan as it can be seen in figure 6.13.

To illustrate the drift motion for a sequence of 300 images the lattice position is translated in a phase between 0 and 2π and is presented in figure 6.16 (a) and (b). From this analysis we find that the first axis is relatively stable over the whole measurement time of 1.5 hours of the sequence. However, the second lattice axis exhibits an almost uniform distribution. This gets more obvious if we represent each lattice position by a unity vector, whose direction is given by the corresponding phase, and plot all 300 unity vectors successively (figure 6.16(c),(d)). In this picture, a perfect stable lattice would be represented by a straight line, small long term drifts would appear as large circles, and short term fluctuations would lead to a pronounced zigzag shape. We assign the short term fluctuations of the lattice to mechanical vibrations of the setup and air turbulences in both arms of each lattice axes, while the long term drifts are probably caused by ther-

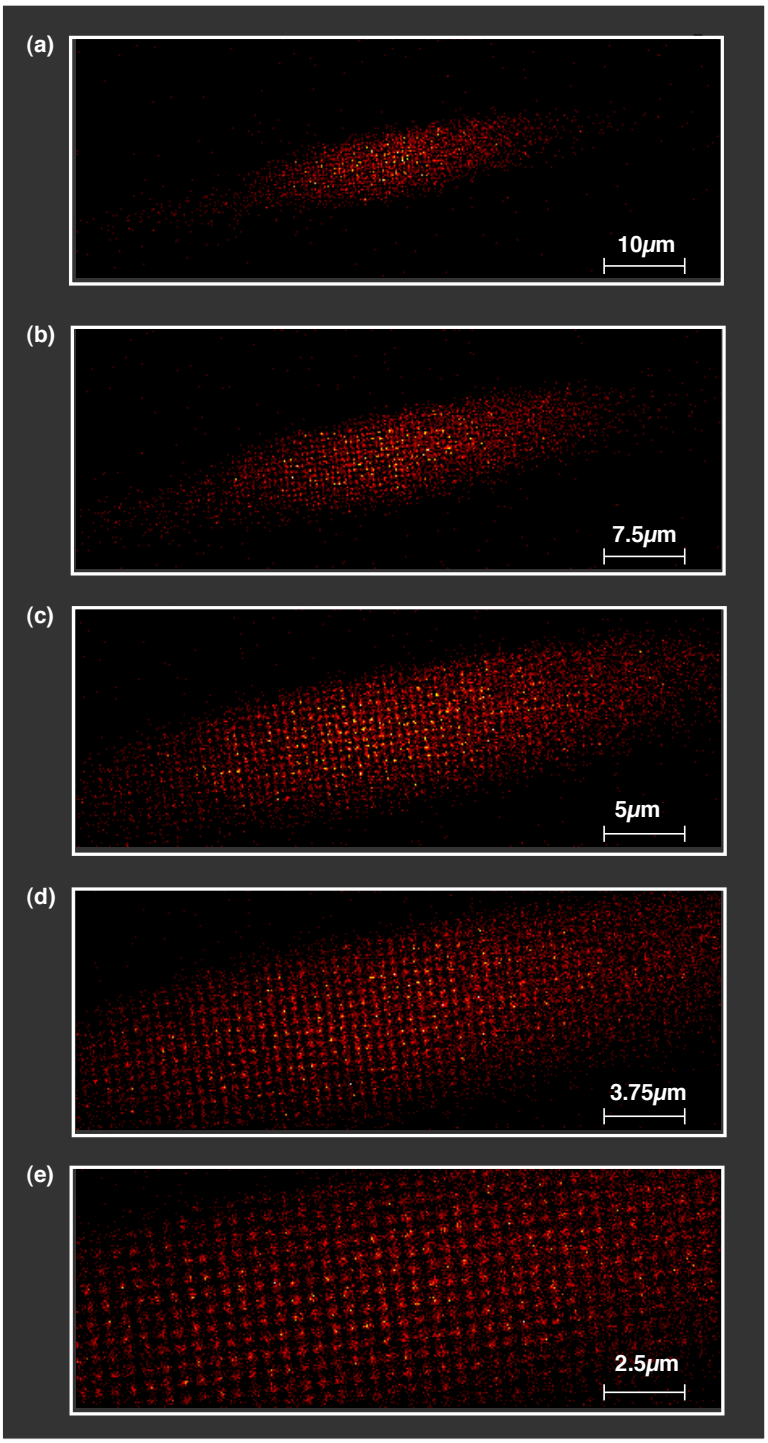

Figure 6.14: Imaging a 2D optical lattice with increasing resolution. Each image is the sum of 30 individual images.

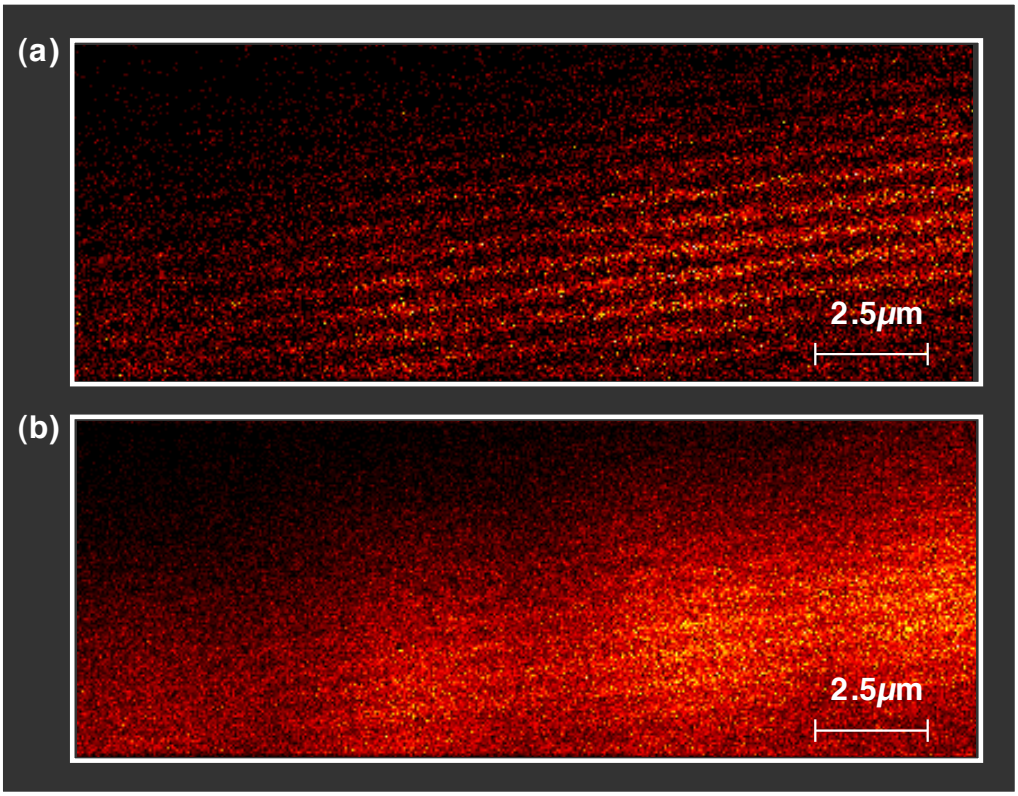

Figure 6.15: Image blurring due to lattice fluctuations. (a) shows the sum of 50 images, while (b) presents the sum of 300 images. The data from which the image (a) is compiled, is a subset of the data shown in (b).

malization processes of the experimental setup. The observation of larger fluctuation and drifts in the second axis are compatible with a less stable optomechanical setup of this axis.

In order to sum 300 lattice images like it was done in section 5.3.3 for the BEC, the phase shift of each image has to be corrected in a post-process. From the fit to the line scan, the actual phase of the lattice is extracted, then the image is accordingly displaced prior to the summation. A detailed description of the image correction process can be found in [144, 147]. In figure 6.17 the result of the correction process is presented using the example of the second lattice axis. Figure 6.17(a) shows the uncorrected sum while the result of the correction process can be seen in figure 6.17(b). The data in both images belong to the same measurement sequence. Due to the

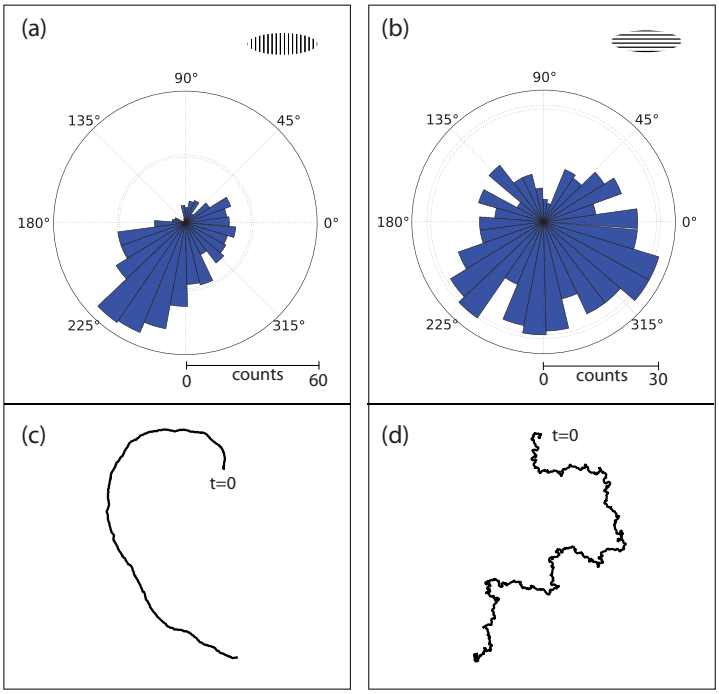

Figure 6.16: Drifts of the optical lattice. (a), and (b) show the appearance of the lattice position, translated into a phase between 0 and 2π, for 300 experimental runs corresponding to 1.5 hours of measurement time. (a) presents the lattice drifts of the first lattice axis, while (b) shows the drifts of the second axis. (c), and (d) illustrate the drift dynamics of the data in (a) and (b). Each lattice position is represented by a unity vector whose direction is given by the corresponding phase. All 300 vectors are successively plotted.

correction process, the lattice structure, which hardly visible in the first image, becomes visible again.

After the presentation of the corrected image of the second lattice axis, a high resolution image of a Bose-Einstein condensate in a 2D optical lattice is shown in figure 6.18. This image is the sum of 260 individual experimental realizations and it is corrected for lattice fluctuations.

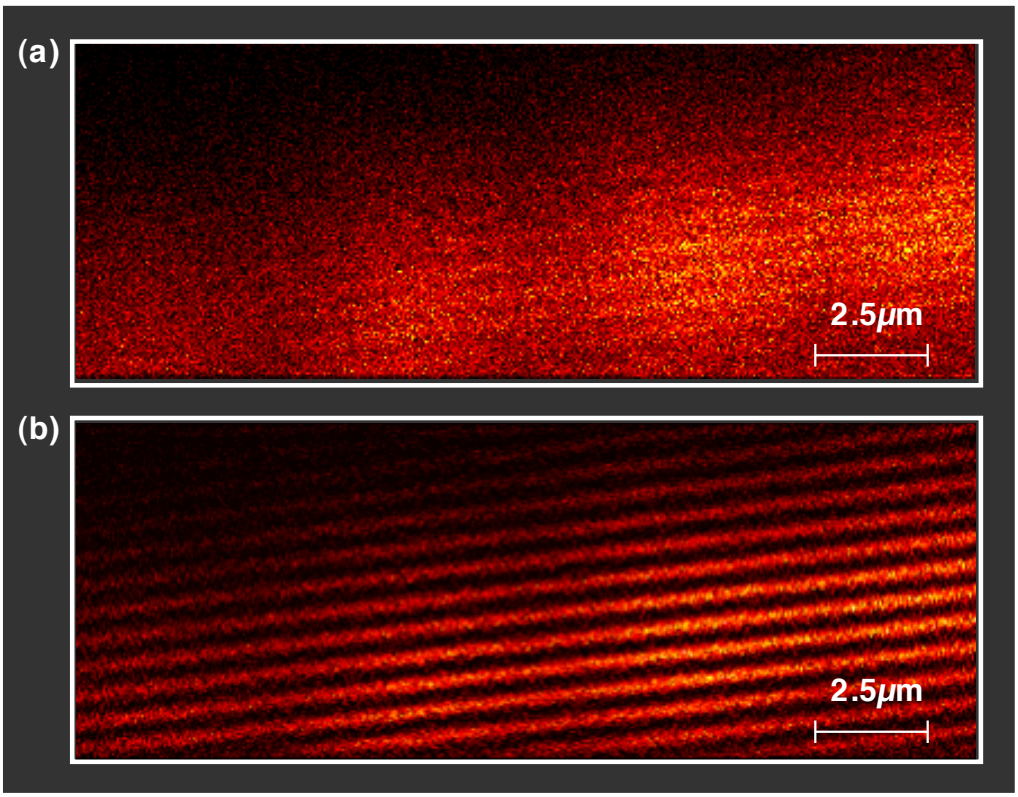

Figure 6.17: Result of the image correction. (a) shows the sum of 300 individual images of the perpendicular optical lattice. In this picture the lattice structure is hardly visible due to lattice fluctuations and drifts. By determining the actual position of the lattice sites in each image and displacing the image accordingly prior to the summation, the lattice structure becomes visible again. (b) shows the result including the correction process. The summed data in both images is the same.

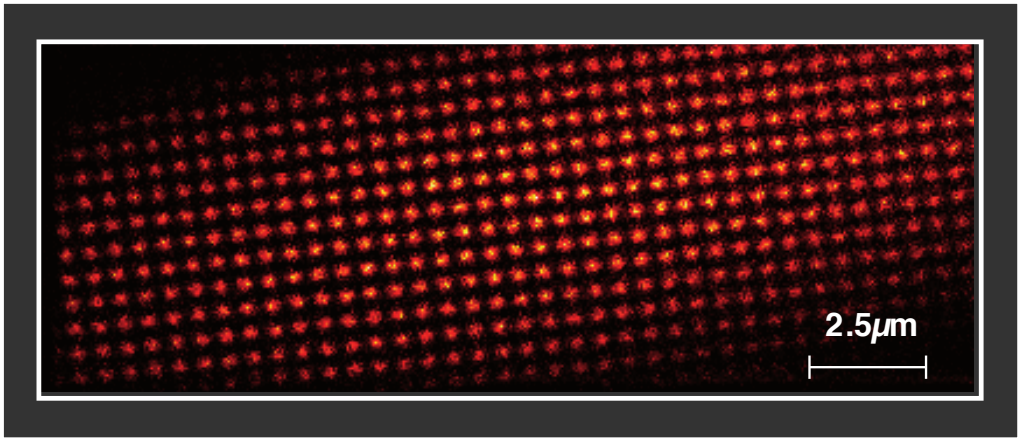

Figure 6.18: Phase corrected electron microscope image of ultracold atoms confined in a 2D optical lattice with 600 nm lattice spacing. The image is a sum of 260 individual images. Each site has a tube-like shape with an extension of 6 μm perpendicular to the projection plane. The lattice sites in the center contain about 80 atoms.

6.3 Dissipative Manipulation of Single Lattice Sites

One general difficulty in the field of ultracold quantum gases in optical lattices is the addressability in these systems, which so far has only been demonstrated for thermal atoms in a lattice with 5 μm lattice spacing [148]. Not-only a site selective read-out, but also a manipulation of single lattice sites is essential in this context.

In this section the spatially resolved dissipative manipulation of an ultracold quantum gas in an one- and two dimensional optical lattice is demonstrated.

6.3.1 Addressing of Single Lattice Sites

The experiments start with the loading of a BEC into an one dimensional optical lattice with a depths of 18 E_R. This lattice depth is deep enough to supress refilling of the lattice site. In order to manipulate a single lattice site by dissipative removal of atoms, the electron beam has to be pointed at the lattice sites for a certain amount of time. For an accurate removal of a lattice site, the knowledge if its position is crucial. Thus it is before determined in an additional measurement.

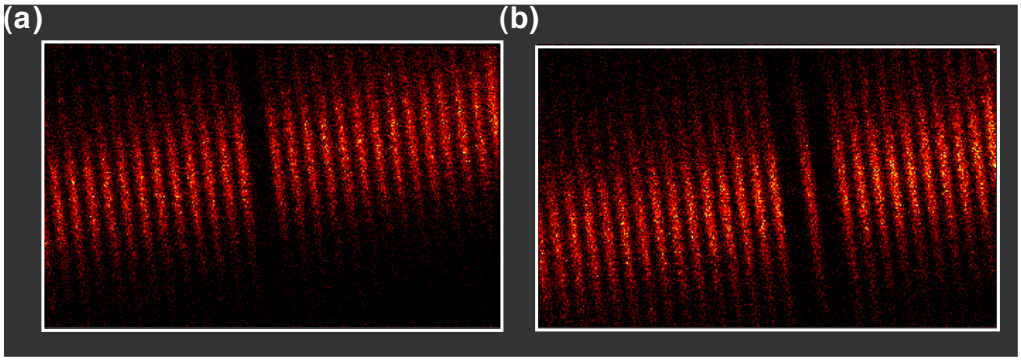

Figure 6.19: Single-site addressability in an 1D lattice. The atoms are removed from the optical lattice by pointing the electron beam at specific sites for 35 ms. The image is taken directly after the preparation. (a) shows a single emptied site (phase corrected sum over 127 images). The lattice depth (18 E_R) is deep enough to suppress refilling of the lattice site. (b) presents the preparation of an isolated site (phase corrected sum over 142 images).

Figure 6.19 presents the removal of specific lattice sites of an one dimensional optical lattice. The sites are addressed by pointing the electron beam at a specific site for 35 ms to remove the atoms. As the atoms are free to move in the radial direction we only slightly move the electron beam across the central part of the lattice site. After the preparation stage the atomic distribution is imaged as described before.

In the previous section the long term drifts and short term fluctuations of the optical lattices have been discussed. Depending on the drifts and the data acquisition times it may occur that during the preparation stage the electron beam points between two lattice sites, thus partially emptying both of them. This can be compensated for by analyzing the lattice phase of each image. If the phase is found to deviate more than acceptable from the ideal position the image is discarded. For the images in figure 6.19 we have tolerated all phases in an interval of $\pm 0.5\pi$, which corresponds to a discrepancy of 150 nm. The first image in figure 6.19 shows a emptied single lattice site. The data documents that this can be accomplished without affecting the neighboring lattice sites. In the second image the preparation of an isolated lattice site is presented. Again, this can be done without

additional losses in the non-addressed sites. This is possible because the electron beam is much smaller then the lattice spacing.

6.3.2 Preparation of Arbitrary Patterns

Addressing single sites in a two dimensional optical lattice [149] is achieved analog to addressing of single sites in an one dimensional lattice. The BEC is loaded into the 2D lattice. Then the electron beam is pointed at selected sites for a preparation time of $1-3$ms per site in order to remove the atoms. The preparation time depends on the number of addressed sites, because the maximal available holding time of the optical lattice at maximum power is limited due to technical reasons. This means that the addressing and imaging of the atoms has to be finished in 220 ms.

Thereafter the imaging procedure is started. Four elementary examples are presented in figure 6.20. The upper left image (figure 6.20(a)) shows a single defect in the lattice structure. This resembles a Schottky defect in a solid and is an ideal starting point to study the tunneling dynamics close to a defect. In the upper right image (figure 6.20(b)) the opposite situation is presented which corresponds to an isolated lattice site. Such a mesoscopic ensemble can act as a paradigm for Rydberg blockade studies as the spatial extension of ensemble is very small [150]. A chain and a ring of lattice sites are shown in figure 6.20 (c) and (d) in order to illustrate the large variety of achievable geometries. Of course, this preparation technique allows for any pattern that fits to the underlying quadratic lattice geometry as can be seen in figure 6.20(e).

In section 6.3.1 was pointed out, that lattice drifts and fluctuations can lead to errors in the addressing protocol, which cannot be compensated for in a post-processing procedure.

Depletion of a Tube

Apart from the complete depletion of a single lattice site, it is as well important to prepare partially filled site, for instance to observe Josephson oscillation [151, 152] between two adjacent sites.

Figure 6.21 shows the decay of the remaining fraction of atoms as a function of addressing time for two different distances of the electron beam from the site center of a 2D lattice. Starting with equation (3.31) the dependence of

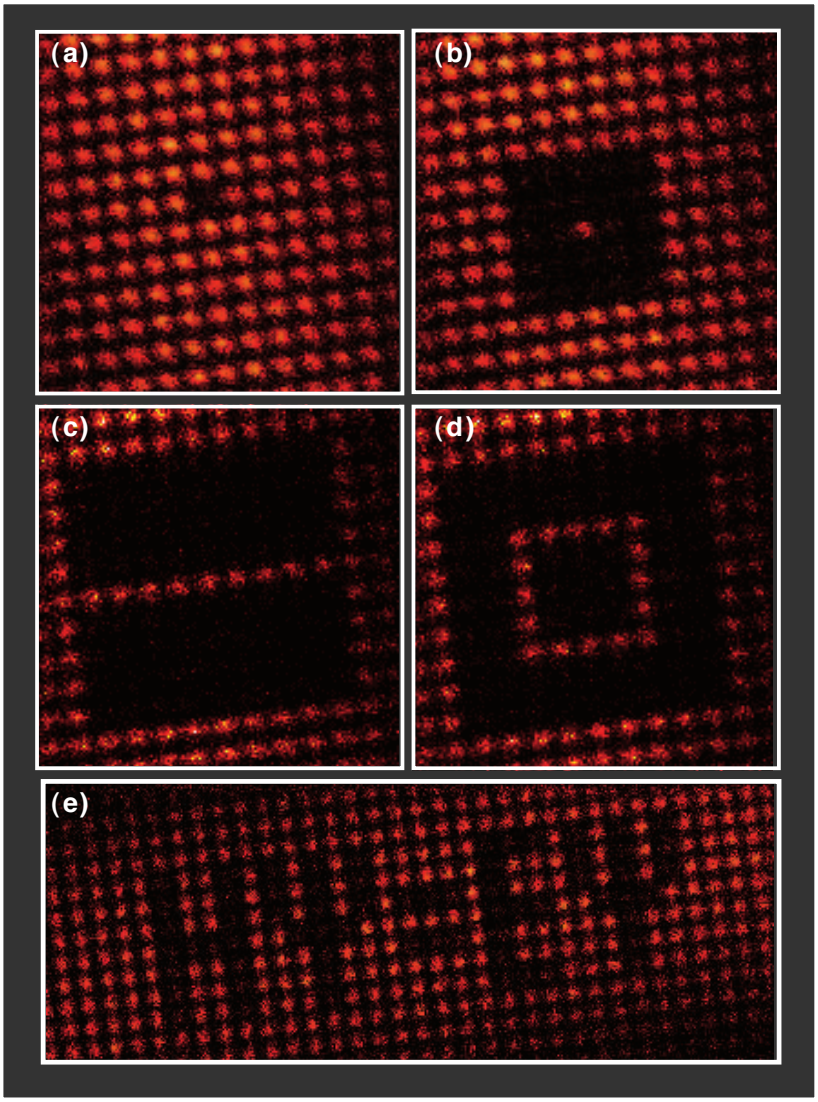

Figure 6.20: Arbitrary patterns in a 2D optical lattice. Between 150 and 250 images from individual experimental realizations have been summed for each pattern. (a) shows a single defect in the lattice structure, while (b) presents an isolated lattice site. The preparation time for (a) and (b) is 3 ms per site. A chain and a ring of lattice sites is shown in (c) and (d). The preparation time in these images is 2 ms per lattice site. The imaging time in the images (a)-(d) is 45 ms which corresponds to 150×150 pixels with a pixel dwell time of 2 μs. Image (e) presents an arbitrary 2D pattern in an image with 150×400 pixels. The preparation time is 1.5 ms per site. For these images, phases in an interval of $\pm 0.6\pi$ have been accepted. With this acceptance interval, we have to discard on average 65% of all images.

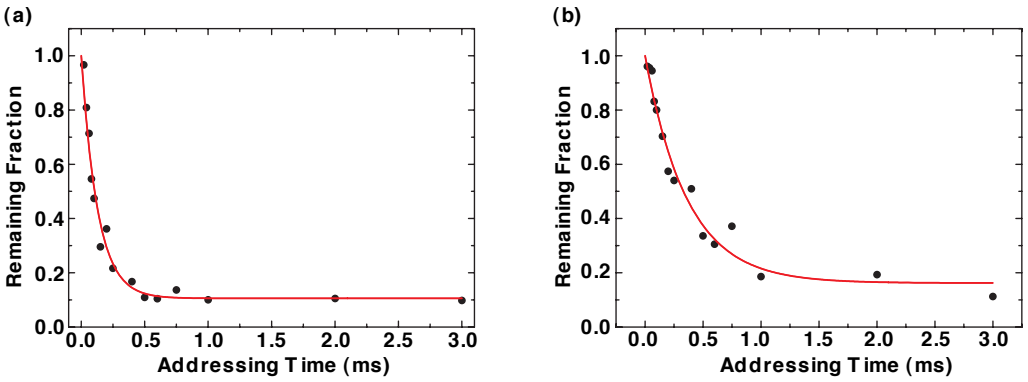

Figure 6.21: Depletion of a 2D lattice site at different distances to the tube center. The solid, red line is a fit with an exponential decay. (a) shows the decay for 90 nm distance, and (b) for 210 nm. The offset of 10% represents atoms that are refilling the lattice site between the end of the preparation and the instant of imaging.

the depletion time constant on the position x_0 of the electron beam can be described by

$$\tau(x_0, y_0) = \left[\frac{\sigma_{\text{tot}}}{q} \int |\psi_{\text{tube}}(x - x_0, y - y_0)|^2 J(x, y) dx dy \right]^{-1}, \qquad (6.19)$$

where the integral denotes the overlap between the electron beam's current density $J(x, y)$, and the density distribution of a 2D lattice site $|\psi_{\text{tube}}(x, y)|^2$. Note, that density dependent losses and the extension of the cloud in the vertical axis have been neglected in this model.

The measured decay constants are shown in figure 6.22. Whereas for central hits we find a time constant of 100 μs, it is more than ten times larger if the electron beam points at the edge of a lattice site. For all positions an exponential decay of the number of atoms is found. For an assumed Gaussian beam profile of the electron beam we find from equation (6.19) a decay constant of 110 μs for a central hit. However, for larger distances from the center we measure a faster decay then expected, indicating that the electron beam profile is not truly Gaussian.

In terms of writing time the result of figure 6.22 means a lattice site can be prepared with our setup in about one millisecond, if it is hit in the center. If we allow for a preparation time of 100 ms, a total of 100 sites can be

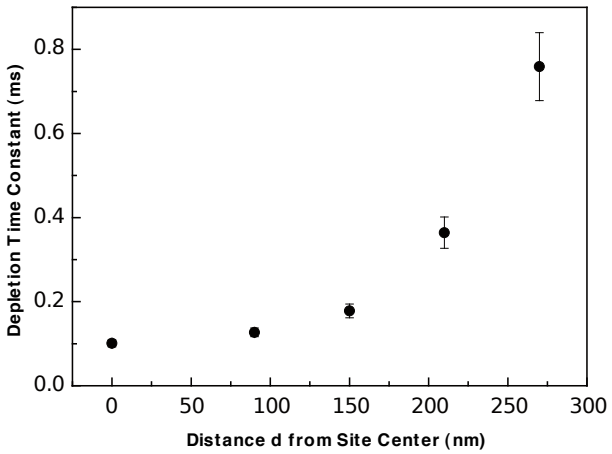

Figure 6.22: Dependence of the depletion time constant of the distance from site center.

emptied. This is sufficient to tailor a large part of a quantum gas in an optical lattice.

Tunneling

A single atom released from a site in a 1D optical lattice periodically tunnels through the lattice with partial revivals at each lattice sites. The characteristic tunneling time, which separates the revivals is given by

$$t = \frac{h}{4J}. \tag{6.20}$$

Between two revivals in the same lattice site, the probability amplitude of the atom goes to zero and we identify $t = h/8J$ as the single particle tunneling time in a 1D lattice. In a 2D lattice, the revivals are more peaked but still occur with a periodicity of $h/4J$. Therefore, the reference tunneling time in the 2D lattice system is taken to be $h/8J$. The lattice depth in the images shown in figure 6.20 is $18\,\mathrm{E_R}$ which results in a tunneling time of $t = 20$ ms. As the preparation time, which is 144 ms for figure 6.20(c) plus the subsequent imaging duration of 45 ms is ten times larger than the tunneling time t, one might expect that a substantial fraction of atoms refills the site after preparation, leaving no visible structure in the image. However, only a small population of about 12% on average is found in the addressed lattice sites. A higher fraction of 25% is found for the single defect in figure 6.20(a) - in accordance with what on might expect as atoms

from four neighboring sites can tunnel into the defect. The isolated lattice site are stables as well as it can be seen in figure 6.20(b). The population in the isolated site decays only 55% of its initial value. For the chain and the ring (figure 6.20(c) and (d)) even higher values of 80%-90% remaining population are found. These results suggest that tunneling in the patterned gas is highly suppressed.

In order to explain the observation, we have to look at the system in more detail. The radial oscillation frequency in each tube is $\omega_{\mathrm{rad}} = 2\pi \times 12\,\mathrm{kHz}$, while the axial frequency is $\omega_{\mathrm{ax}} = 2\pi \times 170\,\mathrm{Hz}$. With a temperature of $T = 100\,\mathrm{nK}$ and a chemical potential of $\mu = h \times 2\,\mathrm{kHz}$, the gas in each tube can be considered as one dimensional. The atoms are radially in the ground state, but they occupy more then ten vibrational modes in the axial direction. The central line density amounts to $n_{1D} = 15\,\mu\mathrm{m}^{-1}$ and results in an interaction strengths of $\gamma = 0.08$. The dynamical evolution of the system after its preparation therefore corresponds to that of an array of coupled, weakly interaction 1D Bose gases. An atom tunneling from a filled site with N atoms has to overcome the total interaction energy of NU. As NU equals the chemical potential, such tunneling processes are highly off-resonant and cannot be compensated by the small tunneling coupling J. Consequently the tunneling dynamic is suppressed. While tunneling of all N particles together is energetically allowed, it is highly unlikely as it requires a Nth-order tunneling process. In fact, the tunneling dynamics in the patterned gas has similarities with nonlinear self-trapping [153] and the observation of repulsively bound pairs [154]. However, as the axial level splitting is much smaller then the interaction energy, tunneling into vibrational excited axial modes of an empty tube might occur as an additional relaxation process.

6.4 Conclusion

By imaging the *in situ* density distribution of a ^{87}Rb Bose-Einstein condensate in a one dimensional optical lattice, with good agreement to the theoretical density profile, the spatial resolution of the method was determined. Moreover, the spatial resolution is good enough to remove atoms from single lattice sites of an 1D and 2D optical lattice, thus demonstrating single site addressability. It was found that the addressed patterns were remarkably stable even for moderate lattice depths, allowing for the creation of a tailored array of mesoscopic ensembles. The possibility to manipulate and observe the occupancy of single lattice sites of an optical lattice will

allow for the studying of tunneling processes in periodic potential in detail. The understanding of the atoms removal process is the starting point for the preparation of different site populations, which could lead to the observation of atomic oscillations [151, 152]. Moreover, the formation of vertical tubes created by the two dimensional optical lattice constitutes an array of mesoscopic ensembles of ultracold atoms. The preparation of arbitrary patterns of such ensembles represents a major step towards tailored quantum systems. In combination with the creation of Rydberg states [85] and exploiting the so-called Rydberg blockade [155, 156], a large number of quantum optical application such as single atom and single photon sources or the creation of Greenberger-Horne-Zeilinger-like states could been realized [150].

Chapter 7

Outlook

The new imaging method for ultracold quantum gases, described in this work paves the way for a various number of applications. The combination of high spatial resolution, single-atom sensitivity, and *in situ* detection opens up new possibilities for the preparation, as well as manipulation and characterization of ultracold quantum gases.

In the future, the addition of a third lattice to the setup gives the possibility to create a variety of systems such as a 3D Mott insulator. At present, the imaging technique offers two dimensional imaging in which the position of the detected atom along the electron beam axis cannot be reconstructed with the existing detection system. However, this can be overcome by implementing an ion extraction system that images the position of the ion along this axis onto a spatial sensitive ion detector. In this way the position of the atom could be reconstructed and the imaging technique becomes fully three dimensional [70].

The presented scheme for arbitrary tailoring quantum gases becomes especially attractive in combination with single site occupancy. A single atom per lattice site can be prepared directly via a 2D Mott insulating state or by removing all but one lattice plane from a 3D Mott insulator [23]. The latter could be used to obtain a two-dimensional array of sites with a well defined occupancy, by emptying all but one lattice plane perpendicular to the electron beam. This can be accomplished for example by a magnetic field gradient in combination with a microwave transition to a different hyperfine ground state and subsequent removal of the transfered atoms with a resonant laser beam. A 2D Mott insulator can also be realized by adding a potential that strongly confines the atoms in the vertical axis,

which would allow for the preparation of a large variety of low dimensional systems [24, 25, 26, 27]. Moreover, the magnetic field of the electron beam may even be used to drive transitions in these atoms. Consequently, the local manipulation of atoms, hitherto dissipative, could be made coherent, which is a prerequisite for many proposals in the field of quantum computation [32].

Although the bonus of single-atom sensitivity has not yet been exploited, it will allow for the measurement of spatial and temporal correlations in trapped quantum gases. The detection of higher-order correlations [157] is a high potential method to probe interacting many-body states with strong correlations, as demonstrated in previous experimental work in trapped gases [158] and expanding [79, 159, 160, 161, 162] gases. The presented imaging method, which features both high spatial resolution and single atom sensitivity, offers the possibility to not only characterize the density distribution but also measure the correlations of low dimensional systems. In particular, in the Tonks-Girardeau regime of impenetrable bosons, where the bosonic wave function can be mapped on its fermionic counterpart [163], the local second order correlation function is strongly reduced due to the "fermionization" of the bosonic wave function [25]. Since the electron beam can be moved at any position and within small time steps, also non-local [164] and temporal correlation functions, which are so far experimentally unexplored, could be measured.

Appendix A

Constants and Rubidium Data

A.1 Constants

Planck's constant	h	$6,626 \cdot 10^{-34}$	Js
Boltzman's constant	k_B	$1,381 \cdot 10^{-23}$	J/K
Bohr's magneton	μ_B	$9,274 \cdot 10^{-24}$	J/T
Vacuum permittivity	ϵ_0	$8,854 \cdot 10^{-12}$	As/VM
Elementary charge	e	$1,602 \cdot 10^{-19}$	C
Speed of light	c	$2,998 \cdot 10^{8}$	m/s

Table A.1: Physical constants

A.2 Rubidium Data

Mass	m	$1,443 \cdot 10^{-25}$	kg
Nuclear spin	I	$\frac{3}{2}$	
Wavelength D_1	λ_{D1}	$794,98$	nm
Wavelength D2	λ_{D2}	$780,25$	nm
Saturation intensity	I_{sat}	$1,654$	mW/cm^2
Line width D_1	Γ_{D1}	$2\pi \cdot 5,58$	MHz
Line width D_2	Γ_{D2}	$2\pi \cdot 6,01$	MHz

Table A.2: Properties of ^{87}Rb.

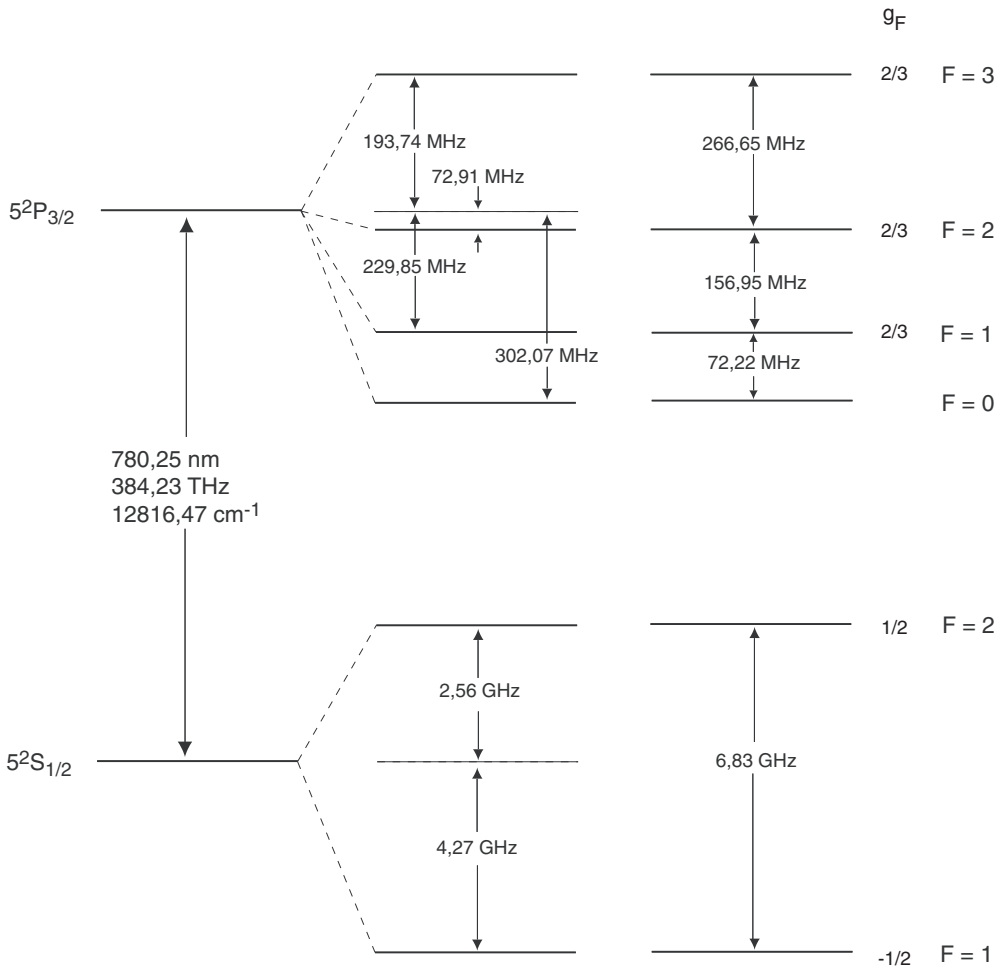

Figure A.1: Hyperfine structure of the D_2-line of ^{87}Rb [165]. Note, energy splitting not true to scale.

Appendix B

Bose-Hubbard-Hamiltonian

A Bose-Einstein condensate trapped in a periodic potential as given in (6.3) can be described by the Bose-Hubbard Hamiltonian [64, 65, 166]

$$\hat{H} = -J \sum_{\langle i,j \rangle} \hat{a}_j^\dagger \hat{a}_i + \frac{U}{2} \sum_i \hat{n}_i \left(\hat{n}_i - 1 \right) + \sum_i \epsilon_i \hat{n}_i. \tag{B.1}$$

Here, $\hat{a}_i$ is the bosonic annihilation operator on site i and $\hat{n}_i \equiv \hat{a}_i^\dagger \hat{a}_i$ denotes the corresponding number operator. Each of the three terms in the Hamiltonian (B.1) describes a different physical mechanisms:

The first term $-J \sum_{\langle i,j \rangle} \hat{a}_j^\dagger \hat{a}_i$ accounts for the tunneling between adjacent lattice wells, denoted by the angle brackets in the sum. By tunneling from site i to site j an atom can lower its energy by

$$J = \int d^3x \mathcal{W}_n^* \left(x - x_i \right) \left(-\frac{\hbar^2 \nabla^2}{2m} + V_{\text{lat}} \right) \mathcal{W}_n \left(x - x_j \right) \tag{B.2}$$

where $\mathcal{W}_n^* \left(x - x_i \right)$ is the localized Wannier function at lattcie site i in the nth energy band as defined in equation (6.15). The tunneling matrix element J is related to the width of the energy band by

$$J = \frac{1}{4} \left(\max E_0^{(n)} - \min E_0^{(n)} \right). \tag{B.3}$$

For the lowest band this correspond to one fourth of the energy difference between $q = 0$ and $q = \hbar k_{\text{lat}}$. An analytical expression for the tunneling element has been derived for deep lattice potentials [166]

$$J \approx \frac{4}{\sqrt{\pi}} \left(\frac{V_{\text{lat}}}{E_R} \right)^{3/4} E_R e^{-2\sqrt{\frac{V_{\text{lat}}}{E_R}}} \tag{B.4}$$

where $V_{\text{lat}} \gg E_R$.

The second term $\frac{U}{2}\sum_i \hat{n}_i\,(\hat{n}_i - 1)$ stands for the on-site interaction. Assuming that there are n_i atoms trapped at lattice site i, than each of the n_i atoms interacts with $(n_i - 1)$ others. In each of these interactions the total energy is raised due to the repulsive interaction of the s-wave scattering for ^{87}Rb by the amount

$$U = \frac{4\pi\hbar^2 a_s}{m}\int d^3x |\mathcal{W}_n\,(x - x_i)\,|^4 \tag{B.5}$$

where $\mathcal{W}_n^*\,(x - x_i)$ denotes the Wannier function of lattice site i in the nth energy band. To calculate the on-site interaction energy one needs to know, apart from the s-wave scattering length a_s, the overlap integral of two particles trapped at a mutual lattice site. For sufficiently deep lattice potentials, i.e. $V_{\text{lat}} \gg E_R$ the harmonic oscillator ground state wave function represents a good approximation for the Wannier function. This harmonic approximation leads to an analytical expression for the on-site interaction energy [166]:

$$U = \sqrt{\frac{8}{\pi}} k_{\text{lat}} a_s E_R \left(\frac{V_{\text{lat}}}{E_R}\right)^{3/4}. \tag{B.6}$$

The last term in (B.1), $\sum_i \epsilon_i n_i$ represents the energy offset of a lattice site i caused by an inhomogeneous trapping potential.

Depending on the ratio between on-site interaction and tunneling, the system can be in two different ground states, which will described briefly in the following. For further information and discussion see [140, 167].

Superfluid Ground State

In the tunneling dominated case, i.e. $U/J \to 0$, the atomic wave is delocalized over the complete lattice, thereby minimizing the total energy. The phase coherence is sustained and at each lattice site a coherent state is found with a number of atoms that obeys a Poissonian distribution. This ground state is called superfluid state.

Mott Insulator Ground State

For dominating on-site interaction, i.e. $U/J \to \infty$, the system arranges to minimize the interaction energy. This results in localized states with a well defined particle number at each lattice site. These states are known as Fock

or number states and as a consequence of the well defined atom number the phase coherence between different lattice sites is lost. This ground state is called Mott-insulating state.

Bibliography

[1] J. Caldwell, B. Turgeon, and X. M. Hua. Hubble Space Telescope Imaging of the North Polar Aurora on Jupiter. *Science*, 257(5076):1512–1515, 1992.

[2] D. Meschede. *Optics, Light, and Lasers*. Wiley-VCH, Berlin, 2006.

[3] M. von Ardenne. Das Elektronen-Rastermikroskop. *Zeitschrift für Physik A*, 109:553, 1938.

[4] C. Davisson and L. H. Germer. The scattering of Electrons by a Single Crystal of Nickel. *Nature*, 119:558, 1927.

[5] R. W. Gurney and E. U. Condon. Quantum Mechanics and Radioactive Disintegration. *Phys. Rev.*, 33(2):127–140, Feb 1929.

[6] J. W. Pan D. Bouwmeester, K. Mattle, M. Eibl, H. Weinfurter, and A. Zeilinger. Experimental quantum teleportation. *Nature*, 390:575, 1997.

[7] M. H. Anderson, J. R. Ensher, M. R. Matthews, C. E. Wieman, and E. A. Cornell. Observation of Bose-Einstein condensation in a dilute atomic vapor. *Science*, 269:198, 1995.

[8] C. C. Bradley, C. A. Sackett, J. J. Tollett, and R. G. Hulet. Evidence of Bose-Einstein Condensation in an Atomic Gas with Attractive Interactions. *Phys. Rev. Let.*, 75:1687, 1995.

[9] K. B. Davis, M.-O. Mewes, M. R. Andrews, N. J. van Druten, D. S. Durfee, D. M. Kurn, and W. Ketterle. Bose-Einstein condensation in a gas of sodium atoms. *Phys. Rev. Let.*, 75:3969, 1995.

[10] E. A. Cornell and C. E. Wieman. Bose-Einstein condensation in a dilute gas, the first 70 years and some recent experiments. *Rev. Mod. Phys.*, 74:875, 2002.

[11] W. Ketterle. When atoms behave as waves: Bose-Einstein condensation and the atom laser. *Rev. Mod. Phys.*, 74:1131, 2002.

[12] A. Einstein. Zur Quantentheorie des idealen Gases. *Sitzungsberichte, Preussische Akademie der Wissenschaften*, Bericht 3:18, 1925.

[13] S. N. Bose. Plancks Gesetz und Lichtquantenhypothese. *Zeitschrift fr Physik*, 26:178, 1924.

[14] J. R. Abo-Shaeer, C. Raman, J. M. Vogels, and W. Ketterle. Observation of Vortex Lattices in Bose-Einstein Condensates. *Science*, 292(5516):476–479, 2001.

[15] R. Gati, J. Albiez, J. Fölling, B. Hemmerling, and M. H. Oberthaler. Realization of a single Josephson junction for Bose-Einstein condensates. *Applied Physics B: Lasers and Optics*, 82:207, 2006.

[16] J. M. Higbie, L. E. Sadler, S. Inouye, A. P. Chikkatur, S. R. Leslie, K. L. Moore, V. Savalli, and D. M. Stamper-Kurn. Direct Nondestructive Imaging of Magnetization in a Spin-1 Bose-Einstein Gas. *Phys. Rev. Lett.*, 95(5):050401, Jul 2005.

[17] J. Kronjäger, C. Becker, M. Brinkmann, R. Walser, P. Navez, K. Bongs, and K. Sengstock. Evolution of a spinor condensate: Coherent dynamics, dephasing, and revivals. *Phys. Rev. A*, 72(6):063619, Dec 2005.

[18] S. Jochim, M. Bartenstein, A. Altmeyer, G. Hendl, S. Riedl, C. Chin, J. Hecker Denschlag, and R. Grimm. Bose-Einstein Condensation of Molecules. *Science*, 302(5653):2101–2103, 2003.

[19] C. A. Regal, C. Ticknor, J. L. Bohn, and D. S. Jin. Creation of ultracold molecules from a Fermi gas of atoms. *Nature*, 424:47, 2003.

[20] M. Greiner, C. A. Regal, and D. S. Jin. Emergence of a molecular Bose-Einstein condensate from a Fermi gas. *Nature*, 426:537, 2003.

[21] L. Verstergaard Hau, S. H. Harris, Z. Dutton, and C. H. Behroozi. Light spped reduction to 17 metres per second in an ultracold atomic gas. *Nature*, 397:594, 1999.

[22] B. P. Anderson and M. A. Kasevich. Macroscopic Quantum Interference from Atomic Tunnel Arrays. *Science*, 282:1686–1689, 1999.

[23] M. Greiner, O. Mandel, T. Esslinger, T. W. Hänsch, and I. Bloch. Quantum phase transition from a superfluid to a Mott insulator in a gas of ultracold atoms. *Nature*, 415(6867):39–44, 2002.

[24] B. Paredes, A. Widera, V. Murg, O. Mandel, S. Fölling, I. Cirac, G. V. Shlyapnikov, and T. W. Hänsch. Tonks-Giradeau gas of ultracold atoms in an optical lattice. *Nature*, 429:277, 2004.

[25] T. Kinoshita, T. Wenger, and D. S. Weiss. Observation of a One-Dimensional Tonks-Girardeau Gas. *Science*, 305(5687):1125, 2004.

[26] Stöferle. T., H. Moritz, C. Schori, M. Köhl, and T. Esslinger. Transition from a Strongly Interacting 1D Superfluid to a Mott Insulator. *Phys. Rev. Lett.*, 92(13):130403, Mar 2004.

[27] Z. Hadzibabic, P. Krüger, M. Cheneau, B. Battelier, and J. Dalibard. Berezinskii-Kosterlitz-Thouless crossover in a trapped atomic gas. *Nature*, 441:1118, 2006.

[28] I. Bloch. Quantum Gases. *Science*, 319(5867):1202–1203, 2008.

[29] D. Jaksch and P. Zoller. The cold atom Hubbard toolbox. *Annals of Physics*, 315:52, 2005.

[30] M. Lewenstein, A. Sanpera, V. Ahufinger, B. Damski, A. Sen, and U. Sen. Ultracold atomic gases in optical lattices: mimicking condensed matter physics and beyond. *Advances in Physics*, 56:243, 2007.

[31] O. Mandel, M. Greiner, A. Widera, T. Rom, T. W. Hänsch, and I. Bloch. Controlled Collisions for Multiparticle Entanglement of Optically Trapped Atoms. *Nature*, 425:937, 2003.

[32] R. Raussendorf and H. J. Briegel. A one-way quantum computer. *Phys. Rev. Lett.*, 86(22):5188–5191, 2001.

[33] M. M. Boyd, T. Zelevinsky, A. D. Ludlow, S. M. Foreman, S. Blatt, T. Ido, and J. Ye. Optical Atomic Coherence at the 1-Second Time Scale. *Science*, 314(5804):1430–1433, 2006.

[34] P. A. M. Dirac. On the Theory of Quantum Mechanics. *Proceedings of the Royal Society of London. Series A, Containing Papers of a Mathematical and Physical Character*, 112(762):661–677, 1926.

[35] E. Fermi. Sulla quantizzazione del gas perfetto monoatomico. *Rend. Lincei*, 3:145–149, 1926.

[36] E. Fermi. On the Quantization of the Monoatomic Ideal Gas. *Arxiv:Cond-mat*, 1999.

[37] E. Fermi. Zur Quantelung des idealen einatomigen Gases. *Zeitschrift für Physik A Hadrons and Nuclei*, 36(11):902–912, 11 1926.

[38] Franz Schwabl. *Statistische Mechanik*. Springer-Verlag Berlin Heidelberg, 2006.

[39] K. Huang. *Statistical Mechanics*. John Wiley & Sons, 1987.

[40] F. Dalfovo, S. Giorgini, L. P. Pitaevskii, and S. Stringari. Theory of Bose-Einstein condensation in trapped gases. *Reviews of Modern Physics*, 71:463, 1999.

[41] J. J. Sakurai. *Modern Quantum Mechanics (2nd Edition)*. Addison Wesley, January 1994.

[42] C. Cohen-Tannoudji, B. Diu, and F. Laloë. *Quantum Mechanics*. Wiley, 1977.

[43] A. Marte. *Feshbach-Resonanzen bei Stössen ultrakalter Rubidiumatome*. PhD thesis, Technische Universität München, 2003.

[44] E. G. M. van Kempen, S. J. J. M. F. Kokkelmans, D. J. Heinzen, and B. J. Verhaar. Interisotope Determination of Ultracold Rubidium Interactions from Three High-Precision Experiments. *Phys. Rev. Lett.*, 88(9):093201, Feb 2002.

[45] N. N. Bogoliubov. On the theory of superfluidity. *Journal of Physics U.S.S.R.*, 11:23, 1947.

[46] C. J. Pethick and H. Smith. *Bose-Einstein condensation in dilute gases*. Cambridge University Press, 2002.

[47] L. P. Pitaevskii and S. Stringari. *Bose-Einstein condensation*. Oxford University Press, 2003.

[48] T. D. Lee and C. N. Yang. Many-Body Problem in Quantum Mechanics and Quantum Statistical Mechanics. *Phys. Rev.*, 105(3):1119–1120, Feb 1957.

[49] E. M. Lifshitz and L. P. Pitaevskii. *Statistical Physics, Part 2*. Pergamon Oxford, 1980.

[50] M. R. Matthews, B. P. Anderson, P. C. Haljan, D. S. Hall, C. E. Wieman, and E. A. Cornell. Vortices in a Bose-Einstein Condensate. *Phys. Rev. Lett.*, 83(13):2498–2501, Sep 1999.

[51] B. P. Anderson, P. C. Haljan, C. E. Wieman, and E. A. Cornell. Vortex Precession in Bose-Einstein Condensates: Observations with Filled and Empty Cores. *Phys. Rev. Lett.*, 85(14):2857–2860, Oct 2000.

[52] A. P. Chikkatur, A. Görlitz, D. M. Stamper-Kurn, S. Inouye, S. Gupta, and W. Ketterle. Suppression and Enhancement of Impurity Scattering in a Bose-Einstein Condensate. *Phys. Rev. Lett.*, 85(3):483–486, Jul 2000.

[53] R. Onofrio, C. Raman, J. M. Vogels, J. R. Abo-Shaeer, A. P. Chikkatur, and W. Ketterle. Observation of Superfluid Flow in a Bose-Einstein Condensed Gas. *Phys. Rev. Lett.*, 85(11):2228–2231, Sep 2000.

[54] K. W. Madison, F. Chevy, W. Wohlleben, and J. Dalibard. Vortex Formation in a Stirred Bose-Einstein Condensate. *Phys. Rev. Lett.*, 84(5):806–809, Jan 2000.

[55] E. Hodby, G. Hechenblaikner, S. A. Hopkins, O. M. Maragò, and C. J. Foot. Vortex Nucleation in Bose-Einstein Condensates in an Oblate, Purely Magnetic Potential. *Phys. Rev. Lett.*, 88(1):010405, Dec 2001.

[56] P. Engels, I. Coddington, P. C. Haljan, and E. A. Cornell. Nonequilibrium Effects of Anisotropic Compression Applied to Vortex Lattices in Bose-Einstein Condensates. *Phys. Rev. Lett.*, 89(10):100403, Aug 2002.

[57] E. P. Gross. Structure of a Quantized Vortex in Boson Systems. *Nuovo Cimento*, 20:451, 1961.

[58] L. P. Pitaevskii. Vortex lines in an imperfect Bose gas. *Sov. Phys.–JETP*, 13:451, 1961.

[59] J. S. Russel. Report on Waves. *Report of the fourteenth meeting of the British Association for the Advancement of Science*, pages pp. 311–390, Plates XLVII–LVII, 1844.

[60] B. H. Bransden and C. J. Joachain. *Physics of Atoms and Molecules*. Longman, 1983.

[61] A. Minguzzi, S. Conti, and M. P. Tosi. The internal energy and condensate fraction of a trapped interacting Bose gas. *Journal of Physics: Condensed Matter*, 9(5):L33–L38, 1997.

[62] M. Naraschewski and D. M. Stamper-Kurn. Analytical description of a trapped semi-ideal Bose gas at finite temperature. *Phys. Rev. A*, 58(3):2423–2426, Sep 1998.

[63] F. Gerbier, J. H. Thywissen, S. Richard, M. Hugbart, P. Bouyer, and A. Aspect. Experimental study of the thermodynamics of an interacting trapped Bose-Einstein condensed gas. *Phys. Rev. A*, 70(1):013607, Jul 2004.

[64] M. P. A. Fisher, P. B. Weichman, G. Grinstein, and D. S. Fisher. Boson localization and the superfluid-insulator transition. *Phys. Rev. B-Condensed Matter*, 40(1):546–70, 1989.

[65] D. Jaksch, C. Bruder, J. I. Cirac, C. W. Gardiner, and P. Zoller. Cold Bosonic Atoms in Optical Lattices. *Phys. Rev. Lett.*, 81(15):3108–3111, 1998.

[66] C. A. Regal, M. Greiner, and D. S. Jin. Observation of Resonance Condensation of Fermionic Atom Pairs. *Phys. Rev. Lett.*, 92(4):040403, Jan 2004.

[67] M. W. Zwierlein, C. A. Stan, C. H. Schunck, S. M. F. Raupach, A. J. Kerman, and W. Ketterle. Condensation of Pairs of Fermionic Atoms near a Feshbach Resonance. *Phys. Rev. Lett.*, 92(12):120403, Mar 2004.

[68] M. Bartenstein, A. Altmeyer, S. Riedl, S. Jochim, C. Chin, J. Hecker Denschlag, and R. Grimm. Crossover from a Molecular Bose-Einstein Condensate to a Degenerate Fermi Gas. *Phys. Rev. Lett.*, 92(12):120401, Mar 2004.

[69] T. Bourdel, L. Khaykovich, J. Cubizolles, J. Zhang, F. Chevy, M. Teichmann, L. Tarruell, S. J. J. M. F. Kokkelmans, and C. Salomon. Experimental Study of the BEC-BCS Crossover Region in Lithium 6. *Phys. Rev. Lett.*, 93(5):050401, Jul 2004.

[70] T. Gericke, C. Utfeld, N. Hommerstad, and H. Ott. A scanning electron microscope for ultracold atoms. *Laser Physics Letters*, 3(8):415, 2006.

[71] T. A. Klar, S. Jakobs, M. Dyba, A. Egner, and S. W. Hell. Fluorescence microscopy with diffraction resolution barrier broken by stimulated emission. *Proc. Natl. Acad. Sci. USA*, 97(15):8206, 2000.

[72] Y. Oshikane, T. Kataoka, M. Okuda, S. Hara, H. Inoue, and M. Nakano. Observation of nanostructure by scanning near-field optical microscope with small sphere probe. *Science and Technology of Advanced Materials*, 8(3):181–185, 2007.

[73] W. Ketterle, D. S. Durfee, and D. M. Stamper-Kurn. Making, probing and understanding Bose-Einstein condensation. *Proceedings of the International School of Physics Enrico Fermi, Bose-Einstein Condensation in Atomic Gases, IOS Press*, 1999.

[74] F. Zernike. *How I Discovered Phase Contrast.* Nobel Lectures, Physics 1942-1964. Elsevier Publishing Company, 1964.

[75] M. R. Andrews, M.-O. Mewes, N. J. van Druten, D. S. Durfee, D. M. Kurn, and W. Ketterle. Direct, Nondestructive Observation of a Bose Condensate. *Science*, 273:84, 1996.

[76] W. Ketterle, D. S. Durfee, and D. M. Stamper-Kurn. Making, probing and understanding Bose-Einstein condensates. In M. Inguscio, S. Stringari, and C. E. Wieman, editors, *Proceedings of the International School of Physics - Enrico Fermi*, page 67. IOS Press, 1999.

[77] M. R. Andrews, D. M. Kurn, H.-J. Miesner, D. S. Durfee, C.G Townsend, S. Inouye, and W. Ketterle. Propagation of Sound in a Bose-Einstein Condensate. *Physical Rev. Let.*, 79:553, 1997.

[78] W. S. Bakr, J. I. Gillen, A. Peng, S. Fölling, and M. Greiner. A quantum gas microscope for detecting single atoms in a Hubbard-regime optical lattice. *Nature*, 462(7269):74–77, 2009.

[79] M. Schellekens, R. Hoppeler, A. Perrin, J. Viana Gomes, D. Boiron, A. Aspect, and C. I. Westbrook. Hanbury Brown Twiss effect for ultracold quantum gases. *Science*, 310:648, 2005.

[80] S. Kraft, A. Günther, J. Fortágh, and C. Zimmermann. Spatially resolved photoionization of ultracold atoms on an atom chip. *Phys. Rev. A*, 75(6):063605, Jun 2007.

[81] H. Ott, E. de Mirandes, F. Ferlaino, G. Roati, V. Türck, G. Modugno, and M. Inguscio. Radio Frequency Selective Addressing of Localized

Atoms in a Periodic Potential. *Phys. Rev. Lett.*, 93(12):120407, Sep 2004.

[82] A. Günther, H. Bender, A. Stibor, J. Fortágh, and C. Zimmermann. Observing quantum gases in real time: Single-atom detection on a chip. *Phys. Rev. A*, 80(1):011604, Jul 2009.

[83] J. Orloff. *Handbook of Charged Particle Optics*. CRC Press LLC, 1997.

[84] F. Scheck. *Theoretische Physik 2, Nichtrelativistische Quantentheorie*. Springer, 2000.

[85] A. Koglbauer. Laserunterstützte Elektronenstoßionisation von Rubidium. Diplomarbeit, Johannes Gutenberg-Universität Mainz, 2009.

[86] H. A. Bethe and R. W. Jackiw. *Intermediate Quantum Mechanics*. W.A. Benjamin, Inc., second edition, 1968.

[87] K. Omidvar and A. H. Khateeb. Inelastic collision of fast charged particles with arbitrary levelled hydrogen-like atoms. *Journal of Physics B: Atomic and Molecular Physics*, 6(2):341–353, 1973.

[88] M. Inokuti. Inelastic Collisions of Fast Charged Particles with Atoms and Molecules⁻The Bethe Theory Revisited. *Rev. Mod. Phys.*, 43(3):297–347, Jul 1971.

[89] M. A. Coplan, J. H. Moore, and J. P. Doering. $(e,2e)$ spectroscopy. *Rev. Mod. Phys.*, 66(3):985, Jul 1994.

[90] P. L. Bartlett and A. T. Stelbovics. Calculation of electron-impact total-ionization cross sections. *Phys. Rev. A*, 66(1):012707, Jul 2002.

[91] P. L. Bartlett and A. T. Stelbovics. Electron-impact ionization cross sections for elements Z=1 to Z=54. *Atomic Data and Nuclear Data Tables*, 86(2):235 – 265, 2004.

[92] R. S. Schappe, P. Feng, L. W. Anderson, C. C. Lin, and T. Walker. Electron Collision Cross-Sections Measured with the Use of a Magneto-Optical Trap. *EPL (Europhysics Letters)*, 29(6):439–444, 1995.

[93] R. S. Schappe, T. Walker, L. W. Anderson, and Chun C. Lin. Absolute Electron-Impact Ionization Cross Section Measurements Using a Magneto-Optical Trap. *Phys. Rev. Lett.*, 76(23):4328–4331, Jun 1996.

[94] T. Walker. private communication.

[95] D. Reitz. Ortsaufgelöster Nachweis ultraklater Atome in optischen Gittern. Diplomarbeit, Johannes Gutenberg-Universität Mainz, 2007.

[96] T. Gericke, P. Würtz, D. Reitz, T. Langen, and H. Ott. High-resolution scanning electron microscopy of an ultracold quantum gas. *Nat Phys*, 4(12):949, 2008.

[97] K. Dieckmann, R. J. C. Spreeuw, M. Weidemüller, and J. T. M. Walraven. Two-dimensional magneto-optical trap as a source of slow atoms. *Phys. Rev. A*, 58(5):3891–3895, Nov 1998.

[98] J. Schoser, A. Batär, R. Löw, V. Schweikhard, A. Grabowski, Yu. B. Ovchinnikov, and T. Pfau. Intense source of cold Rb atoms from a pure two-dimensional magneto-optical trap. *Phys. Rev. A*, 66(2):023410, Aug 2002.

[99] R. S. Conroy, Y. Xiao, M. Vengalattore, W. Rooijakkers, and M. Prentiss. Compact, robust source of cold atoms for efficient loading of a magnetic guide. *Optics Communications*, 226(1-6):259 – 266, 2003.

[100] J. M. Moore, C. C. Davis, and M. A. Coplan. *Building scientific apparatus; 4th ed.* Cambridge Univ. Press, Cambridge, 2009.

[101] C. Utfeld. Aufbau einer Hochleistungsquelle für ultrakalte Atome. Diplomarbeit, Johannes Gutenberg-Universität Mainz, 2006.

[102] T. Petelski. *Atom Interferometers for Precision Gravity Measurements*. PhD thesis, European PhD School, XVII Cycle, 2005.

[103] E. L. Raab, M. Prentiss, A. Cable, S. Chu, and D. E. Pritchard. Trapping of Neutral Sodium Atoms with Radiation Pressure. *Phys. Rev. Lett.*, 59(23):2631–2634, Dec 1987.

[104] L. Ricci, M. Weidemüller, T. Esslinger, A. Hemmerich, C. Zimmermann, V. Vuletic, W. König, and T. W. Hänsch. A compact grating-stabilized diode laser system for atomic physics. *Optics Communications*, 117(5-6):541 – 549, 1995.

[105] T. W. Hänsch, M. D. Levenson, and A. L. Schawlow. Complete Hyperfine Structure of a Molecular Iodine Line. *Phys. Rev. Lett.*, 26(16):946–949, Apr 1971.

[106] G. C. Bjorklund, M. D. Levenson, W. Lenth, and C. Ortiz. Frequency modulation (FM) spectroscopy. *Applied Physics B: Lasers and Optics*, 32(3):145–152, 11 1983/11/01/.

[107] E. I. Gordon. A Review of Acoustooptical Deflection and Modulation Devices. *Appl. Opt.*, 5(10):1629–1639, 1966.

[108] A. Zach. Entwicklung und Aufbau eines frequenzstabilen, schmalbandigen Trapez-Diodenlaser-Verstärker-Systems mit hoher Ausgangsleistung. Diplomarbeit, Fachhochschule Ulm, 1998.

[109] A digital frequency counter counts the frequency of the beat signal, which is then transfered into a voltage.

[110] M. D. Barrett, J. A. Sauer, and M. S. Chapman. All-Optical Formation of an Atomic Bose-Einstein Condensate. *Phys. Rev. Lett.*, 87(1):010404, Jun 2001.

[111] S. R. Granade, M. E. Gehm, K. M. O'Hara, and J. E. Thomas. All-Optical Production of a Degenerate Fermi Gas. *Phys. Rev. Lett.*, 88(12):120405, Mar 2002.

[112] T. Weber, J. Herbig, M. Mark, H. C. Nägerl, and R. Grimm. Bose-Einstein Condensation of Cesium. *Science*, 299(5604):232–235, 2003.

[113] G. Cennini, G. Ritt, C. Geckeler, and M. Weitz. All-Optical Realization of an Atom Laser. *Phys. Rev. Lett.*, 91(24):240408, Dec 2003.

[114] Y. Takasu, K. Maki, K. Komori, T. Takano, K. Honda, M. Kumakura, T. Yabuzaki, and Y. Takahashi. Spin-Singlet Bose-Einstein Condensation of Two-Electron Atoms. *Phys. Rev. Lett.*, 91(4):040404, Jul 2003.

[115] T. Kinoshita, T. Wenger, and D. S. Weiss. All-optical Bose-Einstein condensation using a compressible crossed dipole trap. *Phys. Rev. A*, 71(1):011602, Jan 2005.

[116] M. S. Chang, Q. Qin, W. Zhang, L. You, and M. S. Chapman. Coherent spinor dynamics in a spin-1 Bose condensate. *Nat. Phys.*, 1:111–116, 2005.

[117] R. Grimm, M. Weidemüller, and Y. B. Ovchinnikov. Optical dipole traps for neutral atoms. *Advances in Atomic, Molecular, and Optical Physics*, 42:95–170, 2000.

[118] T. Gericke, P. Würtz, D. Reitz, C. Utfeld, and H. Ott. All-optical formation of a Bose–Einstein condensate for applications in scanning electron microscopy. *Applied Physics B: Lasers and Optics*, 89(4):447–451, 12 2007/12/01/.

[119] B. Fröhlich, T. Lahaye, B. Kaltenhauser, H. Kubler, S. Muller, T. Koch, M. Fattori, and T. Pfau. Two-frequency acousto-optic modulator driver to improve the beam pointing stability during intensity ramps. *Review of Scientific Instruments*, 78(4):043101, 2007.

[120] N. Hommerstad. Eine CO_2-Dipolfalle für ultrakalte Quantengase. Diplomarbeit, Johannes Gutenberg-Universität Mainz, 2007.

[121] P. Würtz. Detection of Ultracold Atoms Using Electron-Impact-Ionization. Diplomarbeit, Johannes Gutenberg-Universität Mainz, 2007.

[122] G. Cennini. *Field-Insensitive Bose-Einstein Condensates and an All-Optical Atom Laser*. PhD thesis, Eberhard-Karls-Universität zu Tübingen, 204.

[123] H. F. Hess. Evaporative cooling of magnetically trapped and compressed spin-polarized hydrogen. *Phys. Rev. B*, 34(5):3476, 1986.

[124] N. Masuhara, J. M. Doyle, J. C. Sandberg, D. Kleppner, T. J. Greytak, H. F. Hess, and G. P. Kochanski. Evaporative Cooling of Spin-Polarized Atomic Hydrogen. *Phys. Rev. Lett.*, 61(8):935, 1988.

[125] C. S. Adams, H. J. Lee, N. Davidson, M. Kasevich, and S. Chu. Evaporative Cooling in a Crossed Dipole Trap. *Phys. Rev. Lett.*, 74(18):3577, 1995.

[126] H. Ott, J. Fortagh, and C. Zimmermann. Dynamics of a Bose-Einstein condensate in an anharmonic trap. *Journal of Physics B: Atomic, Molecular and Optical Physics*, 36(13):2817–2822, 2003.

[127] J. F. Dobson. Harmonic-Potential Theorem: Implications for Approximate Many-Body Theories. *Phys. Rev. Lett.*, 73(16):2244–2247, Oct 1994.

[128] W. Kohn. Cyclotron Resonance and de Haas-van Alphen Oscillations of an Interacting Electron Gas. *Phys. Rev.*, 123(4):1242–1244, Aug 1961.

[129] P. W. Hawkes and E. Kasper. In *Principles of Electron Optics*. Academic Press, San Diego, 1996.

[130] B. E. A. Saleh and M. C. Teich. *Fundamentals of Photonics*. John Wiley and Sons, Inc., 1991.

[131] K. Blaum. private communication.

[132] P. Würtz, T. Gericke, T. Langen, A. Koglbauer, and H. Ott. Probing Bose-Einstein Condensates by Electron Impact Ionization. *J. Phys.: Conf.Ser.*, 141:012020, 2008.

[133] S. E. Koonin and D. C. Meredith. *Computational Physics*. Addison-Wesley, 1990.

[134] L. Lehtovaara, J. Toivanen, and J. Eloranta. Solution of time-independent Schrdinger equation by the imaginary time propagation method. *Journal of Computational Physics*, 221(1):148 – 157, 2007.

[135] B. A. Berg and R. C. Harris. From data to probability densities without histograms. *Computer Physics Communications*, 179(6):443–448, 2008.

[136] R.P. Feynman. Simulating physics with computers. *Int .J. of Theo. Phys.*, 21:467–488, 1982.

[137] R.P. Feynman. Quantum mechanical computers. *Found. Phys.*, 16:503–531, 1986.

[138] I. Bloch. Quantum coherence and entanglement with ultracold atoms in optical lattices. *Nature*, 453:1016, 2008.

[139] I. Bloch. Ultracold quantum gases in optical lattices. *Nat Phys*, 1(1):23, 2005.

[140] M. Greiner. *Ultracold quantum gases in three-dimensional optical lattice potentials*. Dissertation, Ludwig-Maximilians-Universitt, Mnchen, 2003.

[141] N.W. Ashcroft and N.D. Mermin. *Solid state physics*. Saunders College Publishing, 1976.

[142] J. Slater. A soluble problem in energy bands. *Phys. Rev.*, 87, 1952.

[143] A. Hoffmann. Bosonen im optischen Gitter. Diplomarbeit, Freie-Universität Berlin, 2007.

[144] T. Langen. Addressing of ultracold atoms in optical lattices. Diplomarbeit, Johannes Gutenberg-Universität Mainz, 2008.

[145] S. R. Clark and D. Jaksch. Dynamics of the superfluid to Mott-insulator transition in one dimension. *Phys. Rev. A*, 70(4):043612, Oct 2004.

[146] L. Reimer. *Scanning Electron Microscopy*. Springer, 1985.

[147] P. Würtz, T. Gericke, A. Vogler, F. Etzold, and H. Ott. Image formation in scanning electron microscopy of ultracold atoms. *Applied Physics B: Lasers and Optics*, 98(4):641–645, 03 2010.

[148] K. D. Nelson, X. Li, and D. S. Weiss. Imaging single atoms in a three-dimensional array. *Nat Phys*, 3(8):556, 2007.

[149] P. Würtz, T. Langen, T. Gericke, A. Koglbauer, and H. Ott. Experimental Demonstration of Single-Site Addressability in a Two-Dimensional Optical Lattice. *Phys. Rev. Lett.*, 103(8):080404, Aug 2009.

[150] M. D. Lukin, M. Fleischhauer, R. Cote, L. M. Duan, D. Jaksch, J. I. Cirac, and P. Zoller. Dipole Blockade and Quantum Information Processing in Mesoscopic Atomic Ensembles. *Phys. Rev. Lett.*, 87(3):037901, Jun 2001.

[151] F. S. Cataliotti, S. Burger, C. Fort, P. Maddaloni, F. Minardi, A. Trombettoni, A. Smerzi, and M. Inguscio. Josephson junction arrays with Bose-Einstein condensates. *Science*, 293(5531):843–846, 2001.

[152] Th. Anker, M. Albiez, R. Gati, S. Hunsmann, B. Eiermann, A. Trombettoni, and M. K. Oberthaler. Nonlinear Self-Trapping of Matter Waves in Periodic Potentials. *Phys. Rev. Lett.*, 94(2):020403, Jan 2005.

[153] M. Albiez, R. Gati, J. Fölling, S. Hunsmann, M. Cristiani, and M. K. Oberthaler. Direct Observation of Tunneling and Nonlinear Self-Trapping in a Single Bosonic Josephson Junction. *Phys. Rev. Lett.*, 95(1):010402, Jun 2005.

[154] K. Winkler, G. Thalhammer, F. Lang, R. Grimm, J. Hecker Denschlag, A. J. Daley, A. Kantian, H.P. Büchler, and P. Zoller. Repulsively bound atom pairs in an optical lattice. *Nature*, 441:853, 2006.

[155] T. F. Gallagher. *Rydberg Atoms*. Cambridge University Press, 1994.

[156] R. Heidemann, U. Raitzsch, V. Bendkowsky, B. Butscher, R. Löw, L. Santos, and T. Pfau. Evidence for Coherent Collective Rydberg Excitation in the Strong Blockade Regime. *Phys. Rev. Lett.*, 99(16):163601, Oct 2007.

[157] I. Bloch, J. Dalibard, and W. Zwerger. Many-body physics with ultracold gases. *Rev. Mod. Phys.*, 80(3):885–964, Jul 2008.

[158] J. Esteve, J.-B. Trebbia, T. Schumm, A. Aspect, C. I. Westbrook, and I. Bouchoule. Observations of Density Fluctuations in an Elongated Bose Gas: Ideal Gas and Quasicondensate Regimes. *Phys. Rev. Lett.*, 96(13):130403, Apr 2006.

[159] T. Jeltes, J. M. McNamara, W. Hogervorst, W. Vassen, V. Krachmalnicoff, M. Schellekens, A. Perrin, H. Chang, D. Boiron, A. Aspect, and C. I. Westbrook. Comparison of the Hanbury Brown-Twiss effect for bosons and fermions. *Nature*, 445:402, 2007.

[160] S. Fölling, F. Gerbier, A. Widera, O. Mandel, T. Gericke, and I. Bloch. Spatial quantum noise interferometry in expanding ultracold atom clouds. *Nature*, 434(7032):481, 2005.

[161] T. Rom, Th. Best, D. van Oosten, U. Schneider, S. Fölling, B. Paredes, and I. Bloch. Free fermion antibunching in a degenerate atomic Fermi gas released from an optical lattice. *Nature*, 444(7120):733, 2006.

[162] M. Greiner, C. A. Regal, J. T. Stewart, and D. S. Jin. Probing Pair-Correlated Fermionic Atoms through Correlations in Atom Shot Noise. *Phys. Rev. Lett.*, 94(11):110401, Mar 2005.

[163] M. Girardeau. Relationship between Systems of Impenetrable Bosons and Fermions in One Dimension. *J. Math. Phys*, 1:516, 1960.

[164] A. G. Sykes, D. M. Gangardt, M. J. Davis, K. Viering, M. G. Raizen, and K. V. Kheruntsyan. Spatial Nonlocal Pair Correlations in a Repulsive 1D Bose Gas. *Phys. Rev. Lett.*, 100(16):160406, Apr 2008.

[165] D. A. Steck. Rubidium 87 D Line Data. http://steck.us/alkalidata/, 2003.

[166] W. Zwerger. Mott-Hubbard transition of cold gases in an optical lattice. *Journal of Optics B: Quantum Semiclass. Opt*, 5, 2002.

[167] D. Jaksch. *Bose-Einstein condensation and applications*. PhD thesis, Universität Innsbruck, 1999.